Looking at shadows of entanglement wedges

Yuya Kusuki[1], Yuki Suzuki[2], Tadashi Takayanagi[1,3,*], and Koji Umemoto[1]

[1]*Center for Gravitational Physics, Yukawa Institute for Theoretical Physics, Kyoto University, Kitashirakawa Oiwakecho, Sakyo-ku, Kyoto 606-8502, Japan*
[2]*Faculty of Science, Kyoto University, Kitashirakawa Oiwakecho, Sakyo-ku, Kyoto 606-8502, Japan*
[3]*Kavli Institute for the Physics and Mathematics of the Universe (WPI), University of Tokyo, Kashiwa, Chiba 277-8582, Japan*
*E-mail: takayana@yukawa.kyoto-u.ac.jp

Dedicated to the memory of Tohru Eguchi

We present a new method of deriving shapes of entanglement wedges directly from conformal field theory (CFT) calculations. We point out that a reduced density matrix in holographic CFTs possesses a sharp wedge structure such that inside the wedge we can distinguish two local excitations, while outside we cannot. We can determine this wedge, which we call a CFT wedge, by computing a distinguishability measure. We find that CFT wedges defined by the fidelity or Bures distance as a distinguishability measure coincide perfectly with shadows of entanglement wedges in anti-de Sitter (AdS)/CFT. We confirm this agreement between CFT wedges and entanglement wedges for two-dimensional holographic CFTs where the subsystem is chosen to be an interval or double intervals, as well as higher-dimensional CFTs with a round ball subsystem. On the other hand, if we consider a free scalar CFT, we find that there are no sharp CFT wedges. This shows that sharp entanglement wedges emerge only for holographic CFTs owing to the large-N factorization. We also generalize our analysis to a time-dependent example and to a holographic boundary conformal field theory (AdS/BCFT). Finally, we study other distinguishability measures to define CFT wedges. We observe that some of the measures lead to CFT wedges which slightly deviate from the entanglement wedges in AdS/CFT, and we give a heuristic explanation for this. This paper is an extended version of our earlier letter (arXiv:1908.09939 [hep-th]) and includes various new observations and examples.

Subject Index   B21, B22, B24

Contents

		PAGE

1.   Introduction

The anti-de Sitter / conformal field theory (AdS/CFT) correspondence has provided a key framework for exploring quantum gravity aspects of string theory [1]. The principle of AdS/CFT relates quantum gravity in an AdS spacetime equivalently to a CFT which lives on the boundary of AdS. The basic rule of the correspondence is given by the bulk–boundary correspondence [2,3], which says the gravity partition function is equal to the CFT partition function.

To better understand the AdS/CFT correspondence, it is useful to decompose it into subregions. Namely, we would like to understand which subregion in AdS is dual to a given region A in a CFT. The answer to this question has been argued to be the entanglement wedge M_A [4–6], the region surrounded by the subsystem A and the extremal surface Γ_A whose area gives the holographic entanglement entropy [7–12]. Here we consider a static spacetime and assume a restriction on the canonical time slice. In more general time-dependent spacetimes, the genuine entanglement wedge is given by the domain of dependence of M_A.

In this correspondence, called entanglement wedge reconstruction, the bulk reduced density matrix on the entanglement wedge $\rho_{M_A}^{\text{bulk}}$ is equivalent to the CFT reduced density matrix ρ_A. So far, this subregion–subregion duality has been explained by combining several known facts: the gravity dual of a bulk local field operator (called the Hamilton–Kabat–Lifschytz–Lowe (HKLL) map [13–15] and its generalization [16]), the formula of quantum corrections to holographic entanglement entropy [17,18], and the conjectured connection between AdS/CFT and quantum error-correcting codes [19–21]. However, since this explanation relies highly on the dual AdS geometry and its dynamics from the beginning, it is not clear how the entanglement wedge geometry naturally emerges from a CFT itself.

Recently, a new approach to entanglement wedges was reported briefly in Ref. [22], where purely CFT analysis reveals the structure of the entanglement wedge for the first time. In the present paper, which is a full paper accompanying the letter in Ref. [22], we provide not only detailed explanations but also more evidence for this construction, with various new examples. This includes a precise derivation of the entanglement wedge from the Bures metric when the subsystem A consists of double intervals. Moreover, we give purely CFT derivations of the entanglement wedges in a time-dependent setup and in AdS / boundary CFT (BCFT) [23–25]. Though most of our examples are two-dimensional (2d) CFTs, in a later part of this paper we will analyze higher-dimensional CFTs and derive the entanglement wedges from CFTs.

In our analysis, it is important to remember that only a special class of CFTs, called holographic CFTs, can have classical gravity duals which are well approximated by general relativity. A holographic CFT is characterized by a large central charge c (or a large rank of the gauge group N) and very strong interactions. The latter property leads to a large spectrum gap [26–28]. Thus, we expect that the entanglement wedge geometry is available only when we employ holographic CFTs. Indeed, our new framework will explain how entanglement wedges emerge from holographic CFTs.

Consider a locally excited state in a 2d CFT, created by inserting a primary operator $O_\alpha(w, \bar{w})$ on the vacuum. The index α distinguishes different primaries. As the first example, we focus on a 2d CFT on a Euclidean complex plane R^2. We write the coordinates of this space by $(w, \bar{w})$, or equally (x, τ) such that $w = x + i\tau$. We choose a subsystem A on the x-axis and define the reduced density matrix on A, tracing out its complement B:

$$\rho_A(w, \bar{w}) = \mathcal{N}_\alpha \cdot \mathrm{Tr}_B\big[O_\alpha(w, \bar{w})|0\rangle\langle 0|O_\alpha^\dagger(\bar{w}, w)\big], \tag{1.1}$$

where $\mathcal{N}_\alpha$ is a normalization factor to secure $\mathrm{Tr}\,\rho_A = 1$. This state was first introduced in Refs. [29,30] to study its entanglement entropy. We refer also to Ref. [31] for calculations of the entanglement entropy of primary states.

We choose the (chiral and anti-chiral) conformal dimension h_α of the primary operator O_α in the range

$$1 \ll h_\alpha \ll c. \tag{1.2}$$
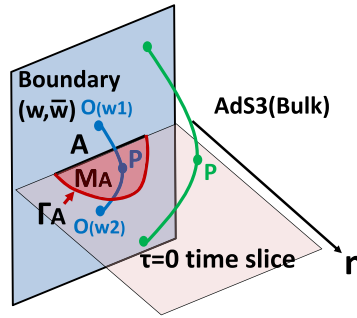
Fig. 1. Sketch of an entanglement wedge M_A for an interval A in AdS$_3$/CFT$_2$, also showing holographic computations of two-point functions dual to geodesics. The blue (or green) geodesic does (or does not) intersect with M_A at P.

This assumption allows us to neglect its backreaction in the gravity dual and to approximate the two-point function $\langle O(w_1, \bar{w}_1) O^{\dagger}(w_2, \bar{w}_2) \rangle$ by the geodesic length in the gravity dual between the two points $(w_1, \bar{w}_1)$ and $(w_2, \bar{w}_2)$ on the boundary $\eta \to 0$ of the Poincaré AdS$_3$

$$ds^2 = \eta^{-2}(d\eta^2 + dw d\bar{w}) = \eta^{-2}(d\eta^2 + dx^2 + d\tau^2), \tag{1.3}$$

where we set the AdS radius to one. Thus, by projecting on the bulk time slice $\tau = 0$, the state $\rho_A(w, \bar{w})$ is dual to a bulk excitation at a bulk point P, which is defined by the intersection between the time slice $\tau = 0$ and the geodesic. This procedure is sketched in Fig. 1.

In this way, we can probe the bulk point by using the locally excited reduced density matrix in Eq. (1.1). If the entanglement wedge reconstruction is correct, then we should be able to distinguish $\rho_A(w, \bar{w})$ and $\rho_A(w', \bar{w}')$ when $w \neq w'$ if either of their bulk points P and P' is in the entanglement wedge. If both of them are outside, we should not be able to distinguish $\rho_A(w, \bar{w})$ and $\rho_A(w', \bar{w}')$. Remarkably, this argument of distinguishability is based on purely CFT calculations and we can define a CFT counterpart of the entanglement wedge from this analysis, which we call the CFT wedge. We can regard CFT wedges as shadows of entanglement wedges when we interpret the geodesics in Euclidean spaces as light rays. In other words, the entanglement wedge reconstruction argues that the CFT wedge coincides with the true entanglement wedge. One may think that our definition of CFT wedges may depend on the choice of the local operator O_α. However, assuming the probe limit in Eq. (1.2), our results for CFT wedges are universal and do not depend on the choice of the local operator. We only define the notion of CFT wedges in this probe limit. The main part of this paper is to confirm these expectations in various examples of AdS/CFT.

The paper is organized as follows. In Sect. 2 we give a brief review of the distance (or distinguishability) measure of quantum states, and introduce the concept of CFT wedges. In Sect. 3 we analyze the geometry of the CFT wedge from the measure $I(\rho, \rho')$ in the single-interval case of 2d CFTs, and confirm that this reproduces the entanglement wedges. In Sect. 4 we study the Bures information metric in the single-interval case of 2d CFTs, and confirm that this reproduces the entanglement wedges. In Sect. 5 we analyze how the time-dependent excited states correctly probe the entanglement wedges in a simple example. In Sect. 6 we turn to the double-interval example in 2d CFTs and confirm that the Bures metric reproduces the entanglement wedges, while the measure $I(\rho, \rho')$ leads to a small deviation. In Sect. 7 we analyze the CFT wedges for global quantum quenches and the thermofield double state, where the correct entanglement wedge is reproduced under a reasonable assumption. In Sect. 8 we extend our calculations of CFT wedges in higher-dimensional holographic

CFTs and confirm that the Bures metric reproduces the correct entanglement wedges. In Sect. 9 we discuss other distinguishability measures, and observe that CFT wedges for most of them fall into the two classes of the Bures metric and $I(\rho, \rho')$. In Sect. 10 we discuss how we can reproduce the entanglement wedge if we employ the HKLL operators instead of local operators. In Sect. 11 we summarize our conclusions and discuss future problems. Appendix A gives the detailed calculations of $I(\rho, \rho')$ in the single interval. In Appendix B we present a detailed analysis of the Bures metric in $c = 1$ CFT. In Appendix C we discuss the Bures metric in a general time-dependent case. In Appendix D we list the properties of various distinguishability measures.

2. Distance measure of quantum states and CFT wedges

The main analysis in this paper is to study the distinguishability of reduced density matrices of the form of Eq. (1.1). Therefore, in this section we summarize relevant measures of distances between two density matrices ρ and ρ'. See Ref. [32] for a textbook. After these preparations we will introduce the notion of CFT wedges, which are finally identified with shadows of entanglement wedges in AdS/CFT.

2.1. Fidelity and related quantities

First, we introduce quantities which provide analogues of the inner product of two density matrices. One of the best quantities is the fidelity $F(\rho, \rho')$ defined by

$$F(\rho, \rho') = \mathrm{Tr}\left[\sqrt{\sqrt{\rho}\rho'\sqrt{\rho}}\,\right]. \tag{2.1}$$

The fidelity is symmetric under an exchange of ρ and ρ', and takes values in the range

$$0 \le F(\rho, \rho') = F(\rho', \rho) \le 1. \tag{2.2}$$

Moreover, it satisfies

$$F(\rho, \rho') = 1 \text{ if and only if } \rho = \rho', \tag{2.3}$$

$$F(\rho, \rho') = 0 \text{ if and only if } \rho\rho' = 0. \tag{2.4}$$

Therefore, we can employ the fidelity to distinguish two quantum states.

There are many other measures which satisfy the basic properties in Eqs. (2.2), (2.3), and (2.4)—they are listed in Appendix D. One of them is the affinity $A(\rho, \rho')$ [33]:

$$A(\rho, \rho') = \mathrm{Tr}\left[\sqrt{\rho}\sqrt{\rho'}\,\right]. \tag{2.5}$$

This quantity has upper and lower bounds in terms of the fidelity:

$$F^2(\rho, \rho') \le A(\rho, \rho') \le F(\rho, \rho'). \tag{2.6}$$

For the actual computations, taking a square root of a given density matrix is not always tractable. This motivates us to consider the quantity $I(\rho, \rho')$:

$$I(\rho, \rho') \equiv \frac{\mathrm{tr}\,\rho\rho'}{\sqrt{\left(\mathrm{tr}\,\rho^2\right)\left(\mathrm{tr}\,\rho'^2\right)}}. \tag{2.7}$$

This quantity is called geometric mean fidelity; it was introduced in Ref. [34] (see also Refs. [35,36]) and satisfies the basic properties in Eqs. (2.2), (2.3), and (2.4). it was employed to study non-equilibrium dynamics of quantum systems in Ref. [37]. We might be able to think that this quantity $I(\rho, \rho')$ is analogous to the second Rényi entropy, while the fidelity is analogous to von Neumann entropy. Indeed, the total power of ρ and ρ' is two in the former, and one in the latter.

It is also useful to evaluate these quantities when the states are pure, expressed as $\rho = |\phi\rangle\langle\phi|$ and $\rho' = |\phi'\rangle\langle\phi'|$. From the definitions, we obtain

$$F(\rho, \rho') = |\langle\phi|\phi'\rangle|, \tag{2.8}$$

$$A(\rho, \rho') = |\langle\phi|\phi'\rangle|^2, \tag{2.9}$$

$$I(\rho, \rho') = |\langle\phi|\phi'\rangle|^2. \tag{2.10}$$

2.2. Distance measures

Now we move on to distance measures between two quantum states ρ and ρ'. First of all, the Bures distance is defined from the fidelity as

$$D_{\mathrm{B}}(\rho, \rho')^2 = 2(1 - F(\rho, \rho')). \tag{2.11}$$

It is obvious that this quantity is symmetric and takes values in the range

$$0 \le D_{\mathrm{B}}(\rho, \rho') = D_{\mathrm{B}}(\rho', \rho) \le 2. \tag{2.12}$$

In addition, it satisfies

$$D_{\mathrm{B}}(\rho, \rho') = 0 \text{ if and only if } \rho = \rho'. \tag{2.13}$$

There are several other important distance measures: the trace distance $D_{\mathrm{tr}}(\rho, \rho')$ [38], relative entropy distance $D_{\mathrm{R}}(\rho, \rho')$, Hellinger distance $D_{\mathrm{H}}(\rho, \rho')$, and geometric mean fidelity distance $D_I(\rho, \rho')$, given respectively by

$$D_{\mathrm{tr}}(\rho, \rho') = \frac{1}{2}|\rho - \rho'|_1 = \frac{1}{2}\mathrm{Tr}\left[\sqrt{(\rho - \rho')^2}\right], \tag{2.14}$$

$$D_{\mathrm{R}}(\rho, \rho')^2 = \mathrm{Tr}\left[\rho(\log\rho - \log\rho')\right], \tag{2.15}$$

$$D_{\mathrm{H}}(\rho, \rho')^2 = 2(1 - A(\rho, \rho')), \tag{2.16}$$

$$D_I(\rho, \rho')^2 = 2(1 - I(\rho, \rho')). \tag{2.17}$$

Three of them, namely D_{tr}, D_{H}, and D_I, satisfy the basic properties in Eqs. (2.12) and (2.13). On the other hand, the relative entropy distance $D_{\mathrm{R}}(\rho, \rho')$ is not symmetric and takes the values $0 \le D_{\mathrm{R}}(\rho, \rho') < \infty$, though Eq. (2.13) holds. Refer to Refs. [39,40] for computations in integrable 2d CFTs, and to Ref. [41] for an application to locally excited states (see also Ref. [42]).

It is useful to note the following relations between these distances:

$$D_{\mathrm{R}}(\rho, \rho') \ge 2D_{\mathrm{tr}}(\rho, \rho')^2, \tag{2.18}$$

$$1 - F(\rho, \rho') \le D_{\mathrm{tr}}(\rho, \rho') \le \sqrt{1 - F(\rho, \rho')^2}. \tag{2.19}$$

2.3.   Information metrics and the quantum Cramér–Rao theorem

Furthermore, we can introduce the so-called information metric when the density matrix is parameterized by continuous variables λ^i, denoted by $\rho(\lambda)$. For the Bures distance, this metric is defined as

$$D_{\mathrm{B}}(\rho(\lambda + d\lambda), \rho(\lambda)) = G_{\mathrm{B}ij}d\lambda^i d\lambda^j + \cdots, \tag{2.20}$$

where the $d\lambda_i$ are infinitesimally small and $\cdots$ denotes the higher powers of $d\lambda^i$. This metric $G_{\mathrm{B}ij}$ is called the Bures metric. In the same way, we can define another metric from the relative entropy distance D_{R}, called the quantum Fisher metric G_{R}. It is also possible to define the metrics G_{H} and G_I for the distance measures D_{H} and D_I, respectively.

The quantum version of the Cramér–Rao theorem [43] (see also the textbook Ref. [32]) tells us that when we try to estimate the value of λ_i from physical measurements, the errors of the estimated value are bounded by the inverse of the Bures metric G_{B}:

$$\langle \delta\lambda^i \delta\lambda^j \rangle \geq (G_{\mathrm{B}}^{-1})^{ij}. \tag{2.21}$$

In particular, when $G_{\mathrm{B}ij} = 0$, the uncertainty becomes divergent and we cannot estimate the value of λ_i at all. This is simply because the density matrix does not depend on λ_i and we cannot distinguish density matrices for various values of λ_i.

More precisely, the quantum Cramér–Rao theorem is stated as follows. A physical measurement is described by the positive operator-valued measure M_ω (≥ 0) such that $\sum_\omega M_\omega = I$, where ω corresponds to each value of the measurement. $\mathrm{Tr}[\rho M_\omega]$ denotes the probability that the measured value is given by ω. We would like to estimate the value of λ^i from the measured value ω following an arbitrarily chosen function $\lambda^i \rightarrow \hat{\lambda}^i(\omega)$. We introduce an error in this process as

$$\langle \delta\lambda^i \delta\lambda^j \rangle \equiv \sum_\omega (\lambda_i - \hat{\lambda}^i(\omega))(\lambda_j - \hat{\lambda}^j(\omega))\mathrm{Tr}[\rho_\lambda M_\omega]. \tag{2.22}$$

To be exact, we actually consider n copies of the system $\rho_\lambda^{\otimes n}$ and take the asymptotic limit

$$\langle \delta\lambda^i \delta\lambda^j \rangle_n \equiv \sum_\omega (\lambda_i - \hat{\lambda}^i(\omega))(\lambda_j - \hat{\lambda}^j(\omega))\mathrm{Tr}[\rho_\lambda^{\otimes n} M_\omega^n]. \tag{2.23}$$

The quantum Cramér–Rao theorem [43] argues that the lower bound is given by the inverse of the Bures metric:

$$\lim_{n\to\infty} n\langle \delta\lambda^i \delta\lambda^j \rangle_n \geq (G_{\mathrm{B}}^{-1})^{ij}. \tag{2.24}$$

2.4.   Simple information metric example: Pure states in CFTs

For pure states $\rho = |\phi\rangle\langle\phi|$ and $\rho' = |\phi'\rangle\langle\phi'|$, the distance measures look like

$$D_{\mathrm{B}}(\rho, \rho')^2 = 2(1 - |\langle\phi|\phi'\rangle|), \tag{2.25}$$

$$D_{\mathrm{H}}(\rho, \rho')^2 = 2(1 - |\langle\phi|\phi'\rangle|^2). \tag{2.26}$$

We omit the relative entropy distance because D_{R} becomes divergent when $|\phi\rangle \neq |\phi'\rangle$.

Consider locally excited states $|\phi(w, \bar{w})\rangle = O_\alpha(w, \bar{w})|0\rangle$ in a 2d CFT. We simply find

$$|\langle\phi(w)|\phi'(w')\rangle| = \frac{|w - \bar{w}|^{2h}|w' - \bar{w}'|^{2h}}{|w - \bar{w}'|^{4h}}. \tag{2.27}$$

This leads to the Bures metric

$$D_{\text{B}}^2 \simeq \frac{h_\alpha}{\tau^2}(d\tau^2 + dx^2),\tag{2.28}$$

and the Hellinger metric

$$D_{\text{H}}^2 \simeq \frac{2h_\alpha}{\tau^2}(d\tau^2 + dx^2).\tag{2.29}$$

Interestingly, the information metric is proportional to the two-dimensional hyperbolic space H_2. This looks like a time slice of the gravity dual, i.e. the Poincaré AdS$_3$ of Eq. (1.3). This coincidence is very natural because the distinguishability between two excitations should increase when the corresponding bulk points are geometrically separated. This was already noted essentially in Ref. [44]. However, this result is universal for any 2d CFT as the computation only involves two-point functions. This implies that the study of the information metric of the reduced density matrix ρ_A has more opportunities to explore deep mechanisms of AdS/CFT, which is the main motivation of this paper.

2.5.   CFT wedges in holographic CFTs

Distinguishability measures for the reduced density matrices of Eq. (1.1) crucially depend on the nature of CFTs such as multi-point correlation functions, as opposed to those for pure states. The special properties of holographic CFTs allow us to introduce a CFT counterpart of the entanglement wedge, as we will explain in this paper for various examples. We call these geometrical structures in holographic CFTs CFT wedges, which we introduce below.

Consider an information metric $G_\#$ (here, $\# = \text{B}, I, \ldots$ specifies the type of distance measure) for a reduced density matrix ρ_A of a locally excited state given by Eq. (1.1), regarding the operator insertion point $X = (w, \bar{w})$ as the parameter λ in Eq. (2.20). The information metric has the components $G_{\#ij}$ with $i, j = w, \bar{w}$, and depends on the location $(w, \bar{w})$. Since the restriction to 2d CFTs is not necessary in this subsection, we have in mind holographic CFTs in any dimensions below.

In this setup, we introduce the geometrical structure in a CFT, which we call the CFT wedge $C_A^{(\#)}$ for the subsystem A, as follows:

$$\begin{aligned} &\text{if } X \in C_A^{(\#)}, \text{ then } G_{\#ij}(X) > 0; \\ &\text{if } X \notin C_A^{(\#)}, \text{ then } G_{\#ij}(X) \simeq 0. \end{aligned}\tag{2.30}$$

In the case of the Bures metric, we can write this equivalently in terms of fidelity as follows:

$$\begin{aligned} &\text{if } X = X' \in C_A^{(\text{B})}, \text{ then } F(\rho(X), \rho(X')) \simeq 1; \\ &\text{if } X \notin C_A^{(\text{B})} \text{ and } X' \notin C_A^{(\text{B})}, \text{ then } F(\rho(X), \rho(X')) \simeq 1; \\ &\text{otherwise}, F(\rho(X), \rho(X')) \simeq 0. \end{aligned}\tag{2.31}$$

Also, for the distance measure $I(\rho, \rho')$ we can express the CFT wedge $C_A^{(I)}$ by

$$\begin{aligned} &\text{if } X = X' \in C_A^{(I)}, \text{ then } I(\rho(X), \rho(X')) \simeq 1; \\ &\text{if } X \notin C_A^{(I)} \text{ and } X' \notin C_A^{(I)}, \text{ then } I(\rho(X), \rho(X')) \simeq 1; \\ &\text{otherwise}, I(\rho(X), \rho(X')) \simeq 0. \end{aligned}\tag{2.32}$$

Note that the sharp geometrical structures in Eqs. (2.30), (2.31), and (2.32) only appear in holographic CFTs, where we take the limit $h_\alpha \gg 1$ as in Eq. (1.2). The non-vanishing information metric in Eq. (2.30) scales as $O(h_\alpha)$. For generic CFTs, such as free field CFTs, we only find smeared behaviors, which prohibit us defining a CFT wedge, though qualitatively the behaviors of distance measures are often similar. In other words, the sharp CFT wedges emerge only when we consider holographic CFTs.

We would also like to stress that the CFT wedges can depend on the choice of distance measures. Indeed, as we will see later, for generic setups, $C_A^{(B)}$ and $C_A^{(I)}$ can differ. In the end, we argue that the correct choice which probes the low-energy states in AdS/CFT (i.e. the code subspace) will be the Bures metric. We will comment more on this point in the final part of this paper.

3. Entanglement wedge from $I(\rho, \rho')$ in the single-interval case

We start with the simplest example, namely the CFT wedges $C_A^{(I)}$ of Eq. (2.32) for the measure $I(\rho, \rho')$ in Eq. (2.7) when A is a single interval in a 2d CFT. Consider a 2d CFT on the flat space $\mathbb{R}^2$, whose Euclidean time and space coordinate are denoted by τ and x. We employ a complex coordinate $(w, \bar{w})$, or equally a Cartesian coordinate (τ, x) such that $w = x + i\tau$. If the CFT has a gravity dual, it is dual to gravity in the Poincaré AdS$_3$ metric of Eq. (1.3). However, below we will analyze both holographic and non-holographic CFTs to compare their results.

3.1. Reduced density matrix for single-interval and CFT wedges

We choose the subsystem A to be an interval $0 \le x \le L$ at $\tau = 0$. The extremal surface Γ_A in the bulk AdS is given by the semicircle $(x - L/2)^2 + \eta^2 = L^2/4$. Therefore, the entanglement wedge M_A is given by

$$(x - L/2)^2 + \eta^2 \le L^2/4. \tag{3.1}$$

Note that this is also identical to the causal wedge [45].

From the viewpoint of CFTs, we consider an excited state by inserting a local operator O_α at $(w, \bar{w})$ and define the reduced density matrix in Eq. (1.1). We regard the location (τ, x) of the insertion point as the parameters of ρ_A. Having in mind the AdS/CFT duality, the geodesic which connects (τ, x) and $(-\tau, x)$ intersects the time slice $\tau = 0$ at the point P given by $\eta = \tau$. Therefore, if the entanglement reconstruction is correct, the CFT wedge, based on a proper distance measure, should coincide with $|w - L/2| \le L/2$, or, equally,

$$C_A: \quad \left(x - \frac{L}{2}\right)^2 + \tau^2 \le \frac{L^2}{4}. \tag{3.2}$$

Accordingly, the information metric should vanish if the intersection P is outside the CFT wedge, i.e.

$$\overline{C_A}: \quad \left(x - \frac{L}{2}\right)^2 + \tau^2 > \frac{L^2}{4}, \tag{3.3}$$

while it is non-vanishing inside the wedge, Eq. (3.2).

In this section we focus on calculating the CFT wedge $C^{(I)}$ for the measure $I(\rho, \rho')$ of Eq. (2.7).
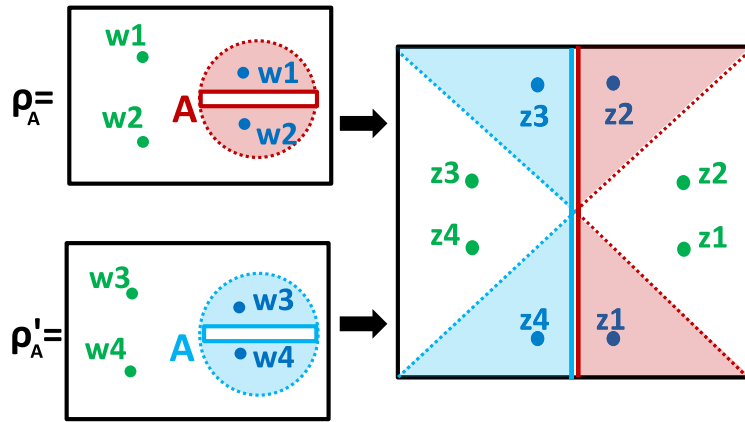
Fig. 2. The conformal mapping for the calculation of $\text{Tr}[\rho\rho']$. The green (or blue) points describe the local excitations in the CFT which are dual to bulk local excitations outside (or inside) the CFT wedge.

3.2. Calculation of $I(\rho, \rho')$

Let us calculate $I(\rho, \rho')$ of Eq. (2.7) for the two density matrices

$$\rho = \rho_A(w, \bar{w}), \qquad \rho' = \rho_A(w', \bar{w}'). \tag{3.4}$$

To calculate $\text{Tr}[\rho\rho']$, consider the conformal transformation[1]

$$z^2 = \frac{w}{w - L}, \tag{3.5}$$

which maps two flat-space path integrals for $\rho(w, \bar{w})$ and $\rho'(w', \bar{w}')$ into a single plane. The coordinate of the latter (single plane) is written as $(z, \bar{z})$. The insertion points of the local operators O_α and $O_\alpha^\dagger$ are given by

$$w_1 = x + i\tau (= w), \qquad w_2 = x - i\tau (= \bar{w}) \tag{3.6}$$

for $\rho(w, \bar{w})$, and

$$w_3' = x' + i\tau' (= w'), \qquad w_4' = x' - i\tau' (= \bar{w}') \tag{3.7}$$

for $\rho(w', \bar{w}')$. Refer to the upper two pictures in Fig. 2. The transformation in Eq. (3.5) maps these four points into z_1, z_2, z_3', and z_4' given by

$$z_1 = \sqrt{\frac{-x - i\tau}{L - x - i\tau}}, \qquad z_2 = \sqrt{\frac{-x + i\tau}{L - x + i\tau}},$$

$$z_3' = -\sqrt{\frac{-x' - i\tau'}{L - x' - i\tau'}}, \qquad z_4' = -\sqrt{\frac{-x' + i\tau'}{L - x' + i\tau'}}. \tag{3.8}$$

It is important to note that the boundaries of the CFT wedge $|w - L/2| = L/2$ of the original two flat planes are mapped into the diagonal lines $z = \pm i\bar{z}$, as depicted in Fig. 2. As we will see soon, this leads to the CFT wedge structure in the distinguishability.

----

[1] The calculations are similar to Refs. [29,30,46].

The trace $\text{Tr}[\rho\rho']$ is now expressed as a correlation function on the z-plane:

$$\text{Tr}[\rho\rho'] = \left|\frac{dz_1}{dw_1}\right|^{2h_\alpha}\left|\frac{dz_2}{dw_2}\right|^{2h_\alpha}\left|\frac{dz_3'}{dw_3'}\right|^{2h_\alpha}\left|\frac{dz_4'}{dw_4'}\right|^{2h_\alpha} \cdot H(z_1, z_2, z_3', z_4') \cdot \frac{Z^{(2)}}{(Z^{(1)})^2},$$

$$H(z_1, z_2, z_3', z_4') \equiv \frac{\langle O_\alpha^\dagger(z_1, \bar{z}_1)O_\alpha(z_2, \bar{z}_2)O_\alpha^\dagger(z_3', \bar{z}_3')O_\alpha(z_4', \bar{z}_4')\rangle}{\langle O_\alpha^\dagger(w_1, \bar{w}_1)O_\alpha(w_2, \bar{w}_2)\rangle\langle O_\alpha^\dagger(w_3', \bar{w}_3')O_\alpha(w_4', \bar{w}_4')\rangle}, \tag{3.9}$$

where $\langle \cdots \rangle$ denotes the normalized correlation function such that $\langle 1 \rangle = 1$, and we also write the vacuum partition function on an n-sheeted complex plane by $Z^{(n)}$.

Thus, we obtain

$$I(\rho, \rho') = \left|\frac{dz_1/dw_1}{dz_1'/dw_1'}\right|^{2h_\alpha}\left|\frac{dz_2/dw_2}{dz_2'/dw_2'}\right|^{2h_\alpha}\left|\frac{dz_3'/dw_3'}{dz_3/dw_3}\right|^{2h_\alpha}\left|\frac{dz_4'/dw_4'}{dz_4/dw_4}\right|^{2h_\alpha}$$

$$\times \frac{F(z_1, z_2, z_3', z_4')}{\sqrt{F(z_1, z_2, z_3, z_4)F(z_1', z_2', z_3', z_4')}}, \tag{3.10}$$

where F is the (normalized) four-point function

$$F(z_1, z_2, z_3', z_4') = \langle O_\alpha^\dagger(z_1, \bar{z}_1)O_\alpha(z_2, \bar{z}_2)O_\alpha^\dagger(z_3', \bar{z}_3')O_\alpha(z_4', \bar{z}_4')\rangle. \tag{3.11}$$

Because we have the relations

$$z_1 = -z_3 = z, \qquad z_2 = -z_4 = \bar{z},$$
$$z_1' = -z_3' = z', \qquad z_2' = -z_4' = \bar{z}', \tag{3.12}$$

we can simplify Eq. (3.10) as follows:

$$I(\rho, \rho') = \frac{F(z, \bar{z}, -z', -\bar{z}')}{\sqrt{F(z, \bar{z}, -z, -\bar{z})F(z', \bar{z}', -z', -\bar{z}')}}. \tag{3.13}$$

We now study this quantity for both a holographic CFT and a free scalar CFT.

3.3.   Holographic CFTs

First, let us evaluate Eq. (3.13) in holographic CFTs. We assume the range in Eq. (1.2) of conformal dimension h_α. In this case, the large-N (or large-c) factorization property justifies the generalized free field approximation [47]. That is, in the large-c limit, the leading contribution to the correlation function in Eq. (3.11) is given by a simple Wick contraction based on the two-point function

$$\langle O_\alpha^\dagger(z, \bar{z})O_\alpha(z', \bar{z}')\rangle = |z - z'|^{-4h_\alpha}. \tag{3.14}$$

The generalized free field prescription leads to a simple expression of the four-point function:

$$F(z_1, z_2, z_3', z_4') \simeq |z_1 - z_2|^{-4h} \cdot |z_3' - z_4'|^{-4h} + |z_1 - z_4'|^{-4h}|z_2 - z_3'|^{-4h}$$

$$\simeq |z - \bar{z}|^{-4h} \cdot |z' - \bar{z}'|^{-4h} + |z + \bar{z}'|^{-8h}, \tag{3.15}$$

where in the final line we remember that $z_1 = z$ and $z' = z_3$. In the right-hand side of Eq. (3.15), the first term comes from the Wick contraction $\langle O^\dagger(1)O(2)\rangle\langle O^\dagger(3)O(4)\rangle$, which we call the trivial Wick contraction. The second term arises from the other Wick contraction, $\langle O^\dagger(1)O(4)\rangle\langle O^\dagger(3)O(2)\rangle$, which we call the non-trivial Wick contraction.

First, consider the case where the local operator is inserted outside the CFT wedge, Eq. (3.3). This is mapped into the uncolored region in Fig. 2 given by the wedge region $|\text{Im}[z]| < |\text{Re}[z]|$. When both w and w' are outside the wedge, the lengths $|z_1 - z_2| = |z - \bar{z}|$ and $|z'_1 - z'_2| = |z' - \bar{z}'|$ are shorter than $|z_1 - z'_4| = |z_2 - z'_3| = |z + \bar{z}'|$. Therefore, the four-point function in Eq. (3.11) is approximated by the first term, which comes from the trivial Wick contraction. Therefore, we finally obtain

$$\text{if } w \text{ and } w' \text{ are outside, then } I(\rho, \rho') \simeq 1. \tag{3.16}$$

This tells us that we cannot distinguish between ρ and ρ' when the local excitations are outside the CFT wedge.

Next, we turn to the case where both w and w' are inside the CFT wedge, Eq. (3.2). In this case, the lengths $|z_1 - z_2| = |z - \bar{z}|$ and $|z'_1 - z'_2| = |z' - \bar{z}'|$ are larger than $|z_1 - z'_4| = |z_2 - z'_3| = |z + \bar{z}'|$. Therefore, the four-point function in Eq. (3.11) is approximated by the second term, which comes from the non-trivial Wick contraction. Therefore, we finally obtain

$$I(\rho, \rho') \simeq |z + \bar{z}'|^{-8h} \cdot |z + \bar{z}|^{4h} \cdot |z' + \bar{z}'|^{4h}. \tag{3.17}$$

Since we always have $|z + \bar{z}||z' + \bar{z}'| \leq |z + z'|^2$ and take the limit $h_\alpha \gg 1$, this quantity $I(\rho, \rho')$ is vanishing except when $z = z'$:

$$\text{if } w \text{ and } w' \text{ are inside and } w = w', \text{ then } I(\rho, \rho') \simeq 1; \tag{3.18}$$

$$\text{if } w \text{ and } w' \text{ are inside and } w \neq w', \text{ then } I(\rho, \rho') \simeq 0. \tag{3.19}$$

Finally, when either of w or w' is inside the CFT wedge, we find that $I(\rho, \rho')$ is vanishing:

$$\text{if } w \text{ is inside and } w' \text{ is outside (or vice versa), then } I(\rho, \rho') \simeq 0. \tag{3.20}$$

These behaviors in Eqs. (3.16), (3.18), (3.19), and (3.20) confirm our expectations in Eq. (2.32), and this shows that the CFT wedge $C_A^{(I)}$ agrees with the entanglement wedge in AdS/CFT in the present example. Refer to Appendix A for more detailed calculations of $I(\rho, \rho')$ in this example.

We also plot the profiles of $I(\rho, \rho')$ in the left columns of Figs. 3 and 4. The left graph in Fig. 3 shows $I(\rho, \rho')$ as a function of w when w' is fixed inside the CFT wedge. We observe a clear peak at $w = w'$, which will be highly localized in the limit $h_\alpha \gg 1$. In the left graphs of Fig. 4 we fixed w' outside the CFT wedge. We can observe a clear entanglement wedge structure, where we have $I \simeq 0$ inside and $I \simeq 1$ outside.

3.4. *Free scalar $c = 1$ CFT*

To understand how the properties of holographic CFTs are relevant to the emergence of entanglement wedges in the gravity duals, consider the free massless scalar CFT ($c = 1$ CFT) in two dimensions. We choose the operator O_α to be

$$O_\alpha(w, \bar{w}) = e^{ip(\phi(w) + \phi(\bar{w}))}, \tag{3.21}$$

where $\phi(w)$ and $\phi(\bar{w})$ are chiral and anti-chiral massless scalar fields. Note that the conformal dimension of the above operator is $h_\alpha = \bar{h}_\alpha = \frac{p^2}{2}$. In this case we obtain

$$F(z, \bar{z}, -z', -\bar{z}') = \frac{|z + z'|^{8h}}{|z - \bar{z}|^{4h}|z' - \bar{z}'|^{4h}|z + \bar{z}'|^{8h}}. \tag{3.22}$$

Holographic CFT (w'=1+0.1i)   Free Scalar (w'=1+0.1i)
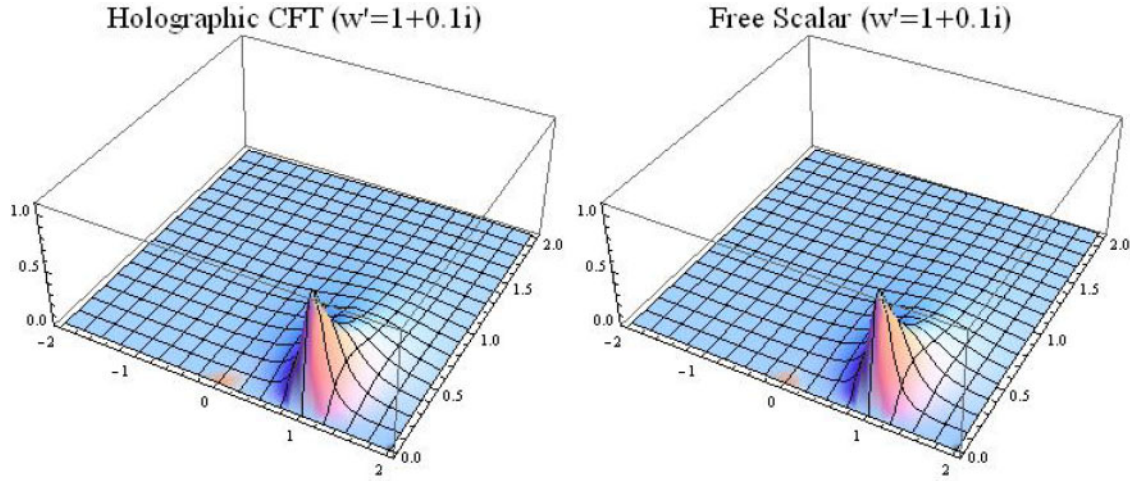
Fig. 3. The value of $I(\rho, \rho')$ as a function of Re$[w]$ (horizontal axis) and Im$[w]$ (depth axis) when w' is fixed inside the CFT wedge. In particular, we chose $h_\alpha = 1/2$, $w' = 1 + 0.1i$, and $A = [0, 2]$ (i.e. $L = 2$). The left and right graphs describe the results for the holographic CFT and the $c = 1$ free scalar CFT, respectively.

We can easily estimate Eq. (3.13) analytically, and obtain

$$I(\rho, \rho') = \left(\frac{|z + z'|^2 |z + \bar{z}||z' + \bar{z}'|}{4|z||z'||z + \bar{z}'|^2} \right)^{4h}, \qquad (3.23)$$

for any values of w and w'. Note that in these excited states, we always have $\text{Tr}[\rho^2] = \text{Tr}[\rho'^2] = 1$ as they do not generate entanglement between the left and right moving modes [29,30,46].

Thus, in this free scalar CFT there is no sharp CFT wedge structure, as expected for non-holographic CFTs. The numerical plots are in the right columns of Figs. 3 and 4. Even though we can observe a peak when w is inside the CFT wedge (see Fig. 3), which is similar to the holographic case, we do not find any sharp CFT wedge when w is outside the wedge (see Fig. 4). In this way we can conclude that there is no emergence of the entanglement wedge in $c = 1$ CFT, as expected.

3.5.   Two different operators

So far we have assumed that both ρ_A and ρ_A' are created by the same local operator O_α, as in Eq. (1.1). It is also instructive to consider the case where ρ_A and ρ_A' are created by two orthogonal operators O_α and O_β respectively (each chiral conformal dimension h_α and h_β) such that the two-point function $\langle O_\alpha O_\beta \rangle$ vanishes. We would like to calculate $I(\rho_A, \rho_A')$ in this case. Again, we can use the expression in Eq. (3.10) as

$$I(\rho_A, \rho_A') = \frac{\langle O_\alpha^\dagger(z_1) O_\alpha(z_2) O_\beta^\dagger(z_3') O_\beta(z_4') \rangle}{\sqrt{\langle O_\alpha^\dagger(z_1) O_\alpha(z_2) O_\alpha^\dagger(z_3) O_\alpha(z_4) \rangle . \langle O_\beta^\dagger(z_1') O_\beta(z_2') O_\beta^\dagger(z_3') O_\beta(z_4') \rangle}}, \qquad (3.24)$$

where we can write $z_1 = z$, $z_2 = \bar{z}$, $z_3 = -z$, $z_4 = -\bar{z}$, etc.

Now we evaluate this in holographic CFTs, by applying the large-c factorization (generalized free field prescription). First of all, we can always estimate

$$\langle O_\alpha^\dagger(z_1) O_\alpha(z_2) O_\beta^\dagger(z_3') O_\beta(z_4') \rangle \simeq |z - \bar{z}|^{-4h_\alpha} \cdot |z' - \bar{z}'|^{-4h_\beta}. \qquad (3.25)$$
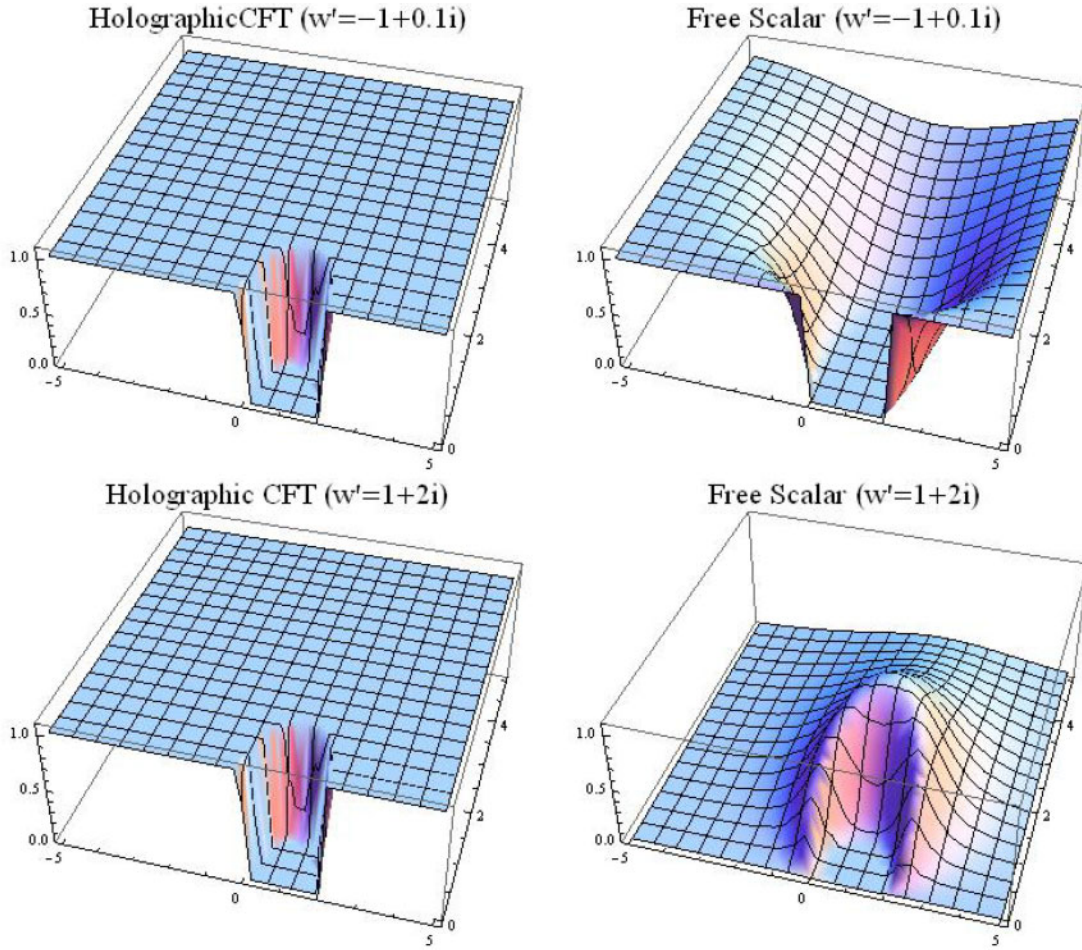
Fig. 4. The value of $I(\rho, \rho')$ as a function of $\text{Re}[w]$ (horizontal axis) and $\text{Im}[w]$ (depth axis) when w' is fixed outside the CFT wedge. In particular, we chose $h_\alpha = 10$ and $A = [0, 2]$ (i.e. $L = 2$). The upper two graphs are for $w' = -1 + 0.1i$, and the lower ones are for $w' = 1 + 2i$, both of which are outside the wedge. The left and right graphs describe the results for the holographic CFT and the $c = 1$ free scalar CFT, respectively. We find that the wedge structure is sharp only in the holographic CFT. For the free scalar CFT, we can detect an excitation even outside the wedge.

Depending on whether $z \simeq z'$ is inside or outside the CFT wedge, Eqs. (3.2) or (3.3), we find

$$\text{inside EW:} \quad \langle O_\alpha^\dagger(z_1) O_\alpha(z_2) O_\alpha^\dagger(z_3) O_\alpha(z_4) \rangle \simeq |z - \bar{z}|^{-8h_\alpha};$$

$$\text{outside EW:} \quad \langle O_\alpha^\dagger(z_1) O_\alpha(z_2) O_\alpha^\dagger(z_3) O_\alpha(z_4) \rangle \simeq |z + \bar{z}|^{-8h_\alpha}. \tag{3.26}$$

Thus, we can evaluate Eq. (3.24) as follows:

$$\text{inside EW:} \quad I(\rho_A, \rho_A') \simeq \left| \frac{z + \bar{z}}{z - \bar{z}} \right|^{4h_\alpha} \cdot \left| \frac{z' + \bar{z}'}{z' - \bar{z}'} \right|^{4h_\beta} \simeq 0;$$

$$\text{outside EW:} \quad I(\rho_A, \rho_A') \simeq 1. \tag{3.27}$$

This nicely fits with the entanglement wedge structure in AdS/CFT: we can distinguish two different operators inside the wedge, while we cannot outside. In particular, since this analysis can be applied to the case when O_β is the identity operator, ρ_A cannot be distinguished from the vacuum one (no insertions of operators), if the insertion of O_α is outside the wedge.
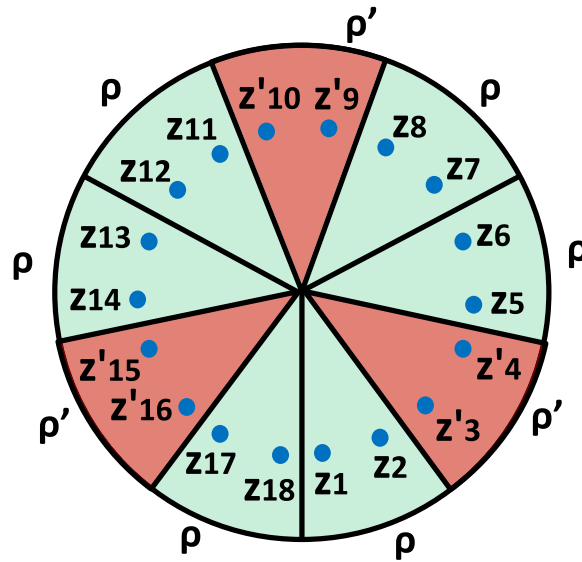
Fig. 5. The complex plane which describes the path integral that calculates the trace $A_{n,m} = \mathrm{Tr}[(\rho^m \rho' \rho^m)^n]$, i.e. Eq. (4.1), after performing the conformal transformation in Eq. (4.3). Here we choose $m = 1$ and $n = 3$ for convenience.

4. The Bures metric in the single-interval case

So far we have studied the measure $I(\rho, \rho')$. Instead, here we calculate the Bures distance $D_{\mathrm{B}}(\rho, \rho')$ defined by Eq. (2.11) and the Bures metric G_{B} defined by Eq. (2.20) in the same setup. This problem is essentially the computation of the following trace:

$$A_{n,m}(\rho, \rho') = \mathrm{Tr}[(\rho^m \rho' \rho^m)^n]. \tag{4.1}$$

By analytically continuing n and m and setting $n = 1/2$ and $m = 1/2$, we obtain the fidelity:

$$A_{1/2,1/2}(\rho, \rho') = \mathrm{Tr}\left[\sqrt{\sqrt{\rho}\rho'\sqrt{\rho}}\right] = F(\rho, \rho'). \tag{4.2}$$

We will employ this replica-like method below to calculate the fidelity.

For this, we apply the conformal transformation

$$z^k = \frac{w}{w - L}, \tag{4.3}$$

where

$$k = (2m + 1)n, \tag{4.4}$$

so that the path integrals for $2mn$ ρs and n ρ's are mapped into that on a single plane, with the correct order of ρs and ρ's specified by Eq. (4.1). See Fig. 5 for a sketch of the geometry after the conformal transformation. This map is similar to those employed for the calculations of relative entropy [48–52].

Then, $A_{n,m}$ is written as the $2k$-point function divided by the normalization of $\mathrm{Tr}[\rho]$ and $\mathrm{Tr}[\rho']$, i.e. two-point functions:

$$A_{n,m} = \frac{\langle O_\alpha^\dagger(w_1) O_\alpha(w_2) \cdots O_\alpha^\dagger(w_{2k-1}) O_\alpha(w_{2k}) \rangle}{\prod_{i=1}^k \langle O_\alpha^\dagger(w_{2i-1}) O_\alpha(w_{2i}) \rangle} \cdot \frac{Z^{(k)}}{(Z^{(1)})^k}. \tag{4.5}$$

Here, $Z^{(k)}$ is the vacuum partition function with k-replicated space. The $2k$-point function in the w-plane is mapped into that in the z-plane by

$$\langle O_\alpha^\dagger(w_1)O_\alpha(w_2)\cdots O_\alpha^\dagger(w_{2k-1})O_\alpha(w_{2k})\rangle$$

$$= \prod_{i=1}^{2k}\left|\frac{dz_i}{dw_i}\right|^{2h}\cdot\langle O_\alpha^\dagger(z_1)O_\alpha(z_2)\cdots O_\alpha^\dagger(z_{2k-1})O_\alpha(z_{2k})\rangle. \quad (4.6)$$

Since we have

$$\frac{dz}{dw} = -\frac{z^{1-k}(z^k-1)^2}{kL} \quad (4.7)$$

and

$$\langle O_\alpha^\dagger(w)O_\alpha(w')\rangle = \left|\frac{(z^k-1)(z'^k-1)}{L(z'^k-z^k)}\right|^{4h_\alpha}, \quad (4.8)$$

the ratio in Eq. (4.5) can be rewritten as

$$A_{n,m} = \prod_{i=1}^{2k}\left|\frac{(z_i)^{1-k}}{k}\right|^{2h_\alpha}\times$$

$$\prod_{j=1}^{k}|(z_{2j-1})^k-(z_{2j})^k|^{4h_\alpha}\cdot\langle O_\alpha^\dagger(z_1)O_\alpha(z_2)\cdots O_\alpha^\dagger(z_{2k-1})O(z_{2k})\rangle\cdot\frac{Z^{(k)}}{(Z^{(1)})^k}. \quad (4.9)$$

Note that we have

$$z_1 = \left(\frac{-x-i\tau}{L-x-i\tau}\right)^{1/k}, \qquad z_2(=\bar{z}_1) = \left(\frac{-x+i\tau}{L-x+i\tau}\right)^{1/k},$$

$$z_{2s+1} = e^{\frac{2\pi i}{k}s}z_1, \qquad z_{2s+2} = e^{\frac{2\pi i}{k}s}z_2 \qquad (s=1,2,\ldots,k-1). \quad (4.10)$$

As we will see in explicit evaluations, the analytical continuation $m=1/2$ is rather straightforward. This allows us to define the convenient ratio

$$A_n(\rho,\rho') = \frac{\text{Tr}[(\sqrt{\rho}\rho'\sqrt{\rho})^n]}{\sqrt{\text{Tr}[\rho^{2n}]\text{Tr}[\rho'^{2n}]}}. \quad (4.11)$$

We immediately find that $A_1(\rho,\rho')=I(\rho,\rho')$ and $A_{1/2}(\rho,\rho')=F(\rho,\rho')$.

4.1. The Bures metric in holographic CFT for Poincaré AdS₃

Let us focus on a holographic 2d CFT. The leading contribution is again given by the generalized free field prescription. When w and w' are outside the CFT wedge, Eq. (3.3), we can approximate the $2k$-point function as

$$\langle O_\alpha^\dagger(z_1)O_\alpha(z_2)\cdots O_\alpha^\dagger(z_{2k-1})O_\alpha(z_{2k})\rangle \simeq \prod_{j=1}^{k}\langle O_\alpha^\dagger(z_{2j-1})O_\alpha(z_{2j})\rangle$$

$$\simeq \prod_{j=1}^{k}|z_{2j-1}-z_{2j}|^{-4h_\alpha}. \quad (4.12)$$

In this case we get the trivial Bures distance

$$D_{\mathrm{B}}(\rho, \rho')^2 = 2(1 - A_{1/2, 1/2}) \simeq 0, \tag{4.13}$$

where we note that $k \to 1$ in this limit. Thus, the Bures metrics $G_{\mathrm{B}ij}$ all vanish in the outside wedge case.

On the other hand, when w and w' are inside the CFT wedge, Eq. (3.2), we can approximate

$$\langle O^\dagger(z_1) O(z_2) \cdots O^\dagger(z_{2k-1}) O(z_{2k}) \rangle \simeq \prod_{j=1}^{k} \langle O^\dagger(z_{2j-2}) O(z_{2j-1}) \rangle$$

$$\simeq \prod_{j=1}^{k} |z_{2j-2} - z_{2j-1}|^{-4h_\alpha}$$

$$\simeq |\bar{z} - e^{\frac{2\pi i}{k}} z'|^{-8h_\alpha n} |\bar{z} - e^{\frac{2\pi i}{k}} z|^{-4h_\alpha(2m-1)n}, \tag{4.14}$$

where we regard $z_0 = z_{2k}$. Thus, we have

$$A_{n,m} \simeq \prod_{i=1}^{2k} \left| \frac{(z_i)^{1-k}}{k} \right|^{2h_\alpha} \times$$

$$|z^k - \bar{z}^k|^{8h_\alpha mn} |z'^k - \bar{z}'^k|^{4h_\alpha n} |\bar{z} - e^{\frac{2\pi i}{k}} z'|^{-8h_\alpha n} |\bar{z} - e^{\frac{2\pi i}{k}} z|^{-4h_\alpha(2m-1)n} \cdot \frac{Z^{(k)}}{(Z^{(1)})^k}. \tag{4.15}$$

In the limit $m = n \to 1/2$ $(k \to 1)$, we find

$$A_{1/2, 1/2} = |z - \bar{z}|^{2h_\alpha} |z' - \bar{z}'|^{2h} |z' - \bar{z}|^{-4h_\alpha} = |w - \bar{w}|^{2h_\alpha} |w' - \bar{w}'|^{2h_\alpha} |w' - \bar{w}|^{-4h_\alpha}, \tag{4.16}$$

where z and w are related by $z = \frac{w}{w-L}$ in the $k \to 1$ limit. By assuming that $dz = z' - z$ is infinitesimally small, we obtain the Bures metric

$$D_{\mathrm{B}}(\rho, \rho')^2 \simeq \frac{h_\alpha}{\tau^2}(dx^2 + d\tau^2). \tag{4.17}$$

Interestingly, this Bures metric coincides with that for the pure state in Eq. (2.28). Therefore, it is proportional to the metric on a time slice of AdS$_3$. Remember that the original Euclidean time coordinate τ can be regarded as the radial coordinate η via the intersection between the geodesic and the time slice, as in Fig. 1. This agreement between the information metric with the bulk metric is natural if we think that the distinguishability in the quantum estimation theory is related to the bulk locality resolution. At the same time, the agreement between the Bures metric for ρ_A with local excitation inside the CFT wedge and that for the pure state tells us us that we can perfectly reconstruct the information in the entanglement wedge from ρ_A. This supports the entanglement wedge reconstruction.

4.2. The Bures metric in holographic CFT for global AdS$_3$

Next, we turn to a holographic CFT dual to the Euclidean global AdS$_3$,

$$ds^2 = R^2(\cosh^2 \rho \, d\tau^2 + d\rho^2 + \sinh^2 \rho \, dx^2). \tag{4.18}$$

This is a 2d holographic CFT with the space coordinate compactified on a circle, $x \sim x + 2\pi$. We choose the subsystem A to be the interval $0 \le x \le l$ at $\tau = 0$.

By performing the conformal transformation $w = e^\xi$ with $\xi = \tau + ix$, we find

$$
A_{1/2,1/2} = \frac{|w - 1/\bar{w}|^{2h_\alpha}|w' - 1/\bar{w}'|^{2h_\alpha}}{|w - 1/\bar{w}'|^{2h_\alpha}|w' - 1/\bar{w}|^{2h_\alpha}} = \left[\frac{2\cosh\tau\cosh\tau'}{\cosh(\tau + \tau') - \cos(x - x')}\right]^{2h_\alpha}. \tag{4.19}
$$

This leads to the following Bures metric inside the CFT wedge:

$$
D_{\mathrm{B}}^2 = \frac{h_\alpha}{\sinh^2\tau}(d\tau^2 + dx^2). \tag{4.20}
$$

Since the geodesic in global AdS$_3$ which connects the two points (τ_0, x_0) and $(-\tau_0, x_0)$ at the boundary $\rho \to \infty$ looks like

$$
e^{2\tau} = \frac{\sinh\rho + \left\{\frac{\cosh^2\rho}{\cosh^2\rho_*} - 1\right\}^{1/2}}{\sinh\rho - \left\{\frac{\cosh^2\rho}{\cosh^2\rho_*} - 1\right\}^{1/2}}, \tag{4.21}
$$

where ρ_* is the intersection point of the time slice $\tau = 0$ and this geodesic in the bulk AdS, by taking the boundary limit $\rho \to \infty$ we find the relation

$$
\sinh\tau_0 = \frac{1}{\sinh\rho_*}. \tag{4.22}
$$

By relating the boundary point (τ, x) to the bulk point (ρ, x) on the time slice $\tau = 0$ using this relation we can rewrite the metric in Eq. (4.20) as

$$
D_{\mathrm{B}}^2 = h_\alpha(d\rho^2 + \sinh^2\rho\, dx^2), \tag{4.23}
$$

which agrees with the time slice metric of the global AdS$_3$, Eq. (4.18).

4.3. The Bures metric in holographic CFT for BTZ

Consider a holographic CFT dual to the Euclidean Bañados–Teitelboim–Zanelli (BTZ) (with a non-compact horizon),

$$
ds^2 = R^2\left(\left(\frac{2\pi}{\beta}\right)^2\sinh^2\rho\, d\tau^2 + d\rho^2 + \left(\frac{2\pi}{\beta}\right)^2\cosh^2\rho\, dx^2\right). \tag{4.24}
$$

This is given by a 2d holographic CFT, with the space coordinate compactified on a circle, $\tau \sim \tau + \beta$.

By performing the conformal transformation $w = e^{\frac{2\pi}{\beta}\xi}$ with $\xi = x + i\tau$, we find the following result in the case of the non-trivial Wick contraction:

$$
A_{1/2,1/2} = |w - \bar{w}|^{2h_\alpha}|w' - \bar{w}'|^{2h_\alpha}|w' - \bar{w}|^{-4h_\alpha} = \left[\frac{2\sin\left(\frac{2\pi}{\beta}\tau\right)\sin\left(\frac{2\pi}{\beta}\tau'\right)}{\cos\left(\frac{2\pi(\tau+\tau')}{\beta}\right) - \cosh\left(\frac{2\pi(x-x')}{\beta}\right)}\right]^{2h_\alpha} \tag{4.25}
$$

Note that we limit the range of τ to $-\beta/2 \le \tau \le \beta/2$.

This leads to the following Bures metric inside the wedge:

$$
D_{\mathrm{B}}^2 = h_\alpha\frac{\left(\frac{2\pi}{\beta}\right)^2}{\sin^2\left(\frac{2\pi}{\beta}\tau\right)}(d\tau^2 + dx^2). \tag{4.26}
$$

The geodesic in BTZ which connects the two points (τ_0, x_0) and $(-\tau_0, x_0)$ at the boundary $\rho = \infty$ looks like

$$e^{i\frac{4\pi}{\beta}\tau} = \frac{\cosh\rho + i\left\{\frac{\sinh^2\rho}{\sinh^2\rho_*} - 1\right\}^{1/2}}{\cosh\rho - i\left\{\frac{\sinh^2\rho}{\sinh^2\rho_*} - 1\right\}^{1/2}}, \tag{4.27}$$

where ρ_* is the intersection point of the time slice $\tau = 0$ and this geodesic in the bulk. Note that Eq. (4.19) in the global AdS and Eq. (4.27) in BTZ are related by the familiar coordinate transformation

$$(\rho, \tau, x) \rightarrow (\rho + i\pi/2, i\tau, ix). \tag{4.28}$$

By taking the boundary limit $\rho = \infty$, we find the relation

$$\sin\left(\frac{2\pi}{\beta}\tau_0\right) = \frac{1}{\cosh\rho_*}. \tag{4.29}$$

By relating the boundary point (τ, x) to the bulk point (ρ, x) on the time slice $\tau = 0$ using this relation, we can rewrite the metric in Eq. (4.26) as

$$D_{\mathrm{B}}^2 = h_\alpha\left(d\rho^2 + \left(\frac{2\pi}{\beta}\right)^2\cosh^2\rho\, dx^2\right), \tag{4.30}$$

which agrees with the time slice metric of the BTZ, Eq. (4.24).

Moreover, we can also confirm that the CFT wedge in this case agrees with the entanglement wedge in BTZ as follows. The condition for the non-trivial Wick contraction is $|z - \bar{z}| > |z + \bar{z}|$, where

$$z^2 = \frac{e^{\frac{2\pi}{\beta}(x+i\tau)} - 1}{e^{\frac{2\pi}{\beta}(x+i\tau)} - e^{\frac{2\pi}{\beta}l}}. \tag{4.31}$$

This leads to the condition

$$\left[e^{\frac{2\pi}{\beta}l}\sin\left(\frac{2\pi\tau}{\beta}\right)\right]^2 + \left(e^{\frac{2\pi}{\beta}l}\cos\left(\frac{2\pi\tau}{\beta}\right) - 1\right)\left(e^{\frac{2\pi}{\beta}l}\cos\left(\frac{2\pi\tau}{\beta}\right) - e^{\frac{2\pi}{\beta}l}\right) \leq 0. \tag{4.32}$$

On the other hand, the geodesic which connects $x = 0$ and $x = l$ (on the slice $\tau = 0$) in the BTZ geometry is

$$\frac{\cosh\left[\frac{2\pi}{\beta}\left(x - \frac{l}{2}\right)\right]}{\sinh\left[\frac{2\pi}{\beta}\left(x - \frac{l}{2}\right)\right]} = \frac{\cosh\rho_*\sinh\rho}{\sqrt{\cosh^2\rho - \cosh^2\rho_*}}, \tag{4.33}$$

where

$$\cosh\rho_* = \frac{\cosh\left(\frac{\pi l}{\beta}\right)}{\sinh\left(\frac{\pi l}{\beta}\right)}. \tag{4.34}$$

This coincides with the border of Eq. (4.32) via the relation between τ and ρ given by Eq. (4.29).

4.4. The Bures distance for different operators

Next, we consider the Bures distance $D_{\mathrm{B}}(\rho_A, \rho_A')$, where ρ_A and ρ_A' are defined by locally excited operators $O_\alpha(w, \bar{w})$ and $O_\beta(w', \bar{w}')$ that are orthogonal to each other. Let us work out the behavior of the Bures distance by computing A_n introduced in Eq. (4.11) and taking the limit $n = 1/2$. Using the expression in Eq. (4.9), we eventually find:

> if w and w' are both outside the CFT wedge, then $A_n \simeq 1$;

> if w and w' are both inside the CFT wedge,

$$\text{then } A_n = \left| \frac{z - e^{\frac{\pi i}{n}} \bar{z}}{z - \bar{z}} \right|^{4h_\alpha n} \cdot \left| \frac{z' - e^{\frac{\pi i}{n}} \bar{z}'}{z' - \bar{z}'} \right|^{4h_\beta n} \simeq 0;$$

> if w is inside and w' outside the CFT wedge,

$$\text{then } A_n = \left| \frac{z - e^{\frac{\pi i}{n}} \bar{z}}{z - \bar{z}} \right|^{4h_\alpha n} \simeq 0. \tag{4.35}$$

Here, we used the assumption that $h_\alpha, h_\beta \gg 1$ and noted that the inside CFT wedge region is given by $|z - e^{\frac{\pi i}{n}} \bar{z}| < |z - \bar{z}|$. By taking the $n = 1/2$ limit, the fidelity behaves as follows:

> if w and w' are both outside the CFT wedge, then $F(\rho, \rho') \simeq 1$;

> otherwise, $F(\rho, \rho') \simeq 0$. \hfill (4.36)

The above behaviors precisely agree with what we expect from the entanglement wedge reconstruction.

4.5. The Bures distance in free scalar $c = 1$ CFT

It is useful to compare the previous Bures metric in holographic CFTs with that in free scalar CFT. Consider a $c = 1$ free scalar CFT and choose the primary operator O_α to be as in Eq. (3.21) with $p = 1/2$ to simplify the calculations. As we explain in Appendix B, in this case we can analytically evaluate $A_{n,m}$, and eventually we find the fidelity

$$A_{1/2,1/2} = \frac{(\sqrt{z} + \sqrt{z'})(\sqrt{\bar{z}} + \sqrt{\bar{z}'})}{(\sqrt{z} + \sqrt{\bar{z}'})(\sqrt{\bar{z}} + \sqrt{z'})} \cdot \frac{(\sqrt{z} + \sqrt{\bar{z}})(\sqrt{z'} + \sqrt{\bar{z}'})}{4\sqrt{|z||z'|}}, \tag{4.37}$$

where $z = w/(w - L)$. Several profiles of the fidelity are plotted in Fig. 6.

The Bures metric for the free scalar can be found as

$$D_{\mathrm{B}}^2 = -\frac{L^2 (dw)^2}{16 w^2 (L - w)^2} - \frac{L^2 (d\bar{w})^2}{16 \bar{w}^2 (L - \bar{w})^2} + \frac{L^2}{\left(\sqrt{\frac{w}{w-L}} + \sqrt{\frac{\bar{w}}{\bar{w}-L}} \right)^2} \cdot \frac{(dw)(d\bar{w})}{2|w||w - L|^3}. \tag{4.38}$$

This metric is plotted in Fig. 7. Note that we cannot find any sharp structure of a CFT wedge, as opposed to the holographic CFT. However, in the limit $\tau \to 0$, we find the metric $D_{\mathrm{B}}^2 \simeq \frac{h}{\tau^2}(d\tau^2 + dx^2)$ for $0 \le x \le L$.

5. Time dependence

In this section we analyze how we can understand time evolutions of the CFT wedges and how they agree with the AdS/CFT prediction.
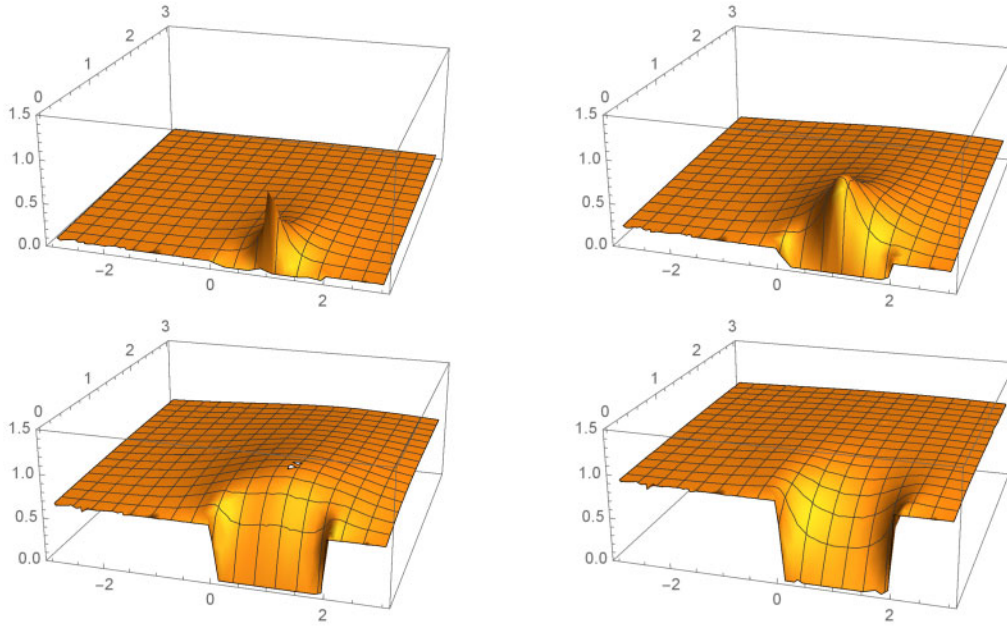
Fig. 6. Profiles of the fidelity $A_{n=1/2,m=1/2} = \text{Tr}\left[\sqrt{\sqrt{\rho}\rho'\sqrt{\rho}}\right]$ in $c = 1$ free scalar CFT for the operator $O = e^{i\phi}$, which has the dimension $h = 1/2$ when we change the value of w. The upper left, upper right, lower left, and lower right graphs describe $A_{n=1/2,m=1/2}$ for $w = 1 + 0.05i$, $w = 1 + 0.2i$, $w = 1 + 0.8i$, and $w = 1 + 2i$, respectively. $A_{n=1/2,m=1/2}$ is plotted as a function of (p, q) for $\rho'(w' = p + iq)$, with $L = 2$.
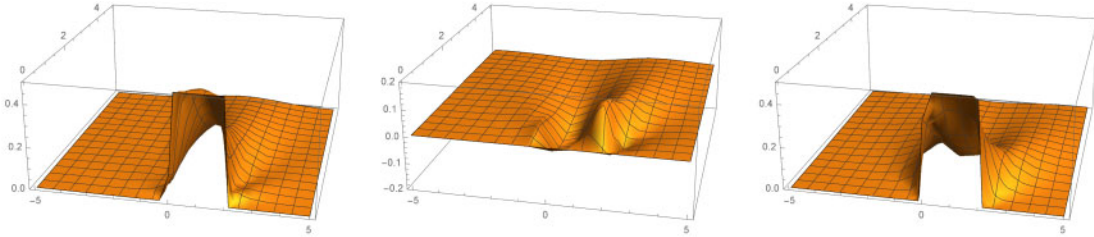
Fig. 7. Profiles of the Bures metric for $c = 1$ free scalar CFT as a function of $w = x + i\tau$: $\tau^2 G_{\tau\tau}$ (left), $\tau^2 G_{\tau x}$ (middle), and $\tau^2 G_{xx}$ (right) as functions of x and τ, with $L = 2$. At the boundary $\tau \to 0$, we find $\tau^2 G_{\tau\tau,xx} \to \frac{1}{2}$ and $\tau^2 G_{\tau x} \to 0$.

Consider insertions of two operators O_α and $O_\alpha^\dagger$ at $w_1 = x + i\tau_1$ and $w_2 = x - i\tau_2$. If we choose

$$\tau_1 = \tau_0 + it, \qquad \tau_2 = \tau_0 - it, \tag{5.1}$$

then we can describe the Lorentzian time evolution of the state $e^{-\tau_0 H} O_\alpha(x)|0\rangle$.

The gravity dual of the two-point function $\langle O_\alpha^\dagger(w_1, \bar{w}_1) O_\alpha(w_2, \bar{w}_2)\rangle$ is given by the geodesic in the Poincaré AdS$_3$ which connects the two boundary points, given by

$$\left(\tau - \frac{\tau_1 - \tau_2}{2}\right)^2 + \eta^2 = \frac{(\tau_1 + \tau_2)^2}{4}. \tag{5.2}$$

This intersects with the time slice $\tau = 0$ at the point $\eta = \sqrt{\tau_1 \tau_2}$. Therefore, the condition of inside the CFT wedge,

$$\left(x - \frac{L}{2}\right)^2 + \eta^2 \leq \frac{L^2}{4}, \tag{5.3}$$

is rewritten in terms of the CFT as

$$x^2 - Lx + \tau_1\tau_2 \leq 0. \tag{5.4}$$

We now derive this condition from the information metric analysis. The crucial condition of the CFT wedge is

$$|z_2 - z_3| \leq |z_1 - z_2|, \tag{5.5}$$

where

$$z_1 = \sqrt{\frac{-x - i\tau_1}{L - x - i\tau_1}} = -i\sqrt{\frac{x + i\tau_1}{L - x - i\tau_1}},$$

$$z_2 = \sqrt{\frac{-x + i\tau_2}{L - x + i\tau_2}} = i\sqrt{\frac{x - i\tau_2}{L - x + i\tau_2}},$$

$$z_3 = -z_1. \tag{5.6}$$

This condition is rewritten as

$$\mathrm{Re}\left[\sqrt{(x + i\tau_1)(x + i\tau_2)(L - x + i\tau_1)(L - x + i\tau_2)}\right] \geq 0. \tag{5.7}$$

This is equivalent to

$$\mathrm{Im}[(x + i\tau_1)(x + i\tau_2)(L - x + i\tau_1)(L - x + i\tau_2)] \geq 0, \tag{5.8}$$

or equally

$$-(\tau_1 + \tau_2)L(x^2 - Lx + \tau_1\tau_2) \geq 0, \tag{5.9}$$

which finally reproduces the condition in Eq. (5.4) derived from the entanglement wedge structure in AdS/CFT.

After the analytical continuation to the real time evolution of Eq. (5.1), the CFT wedge is given by

$$\left(x - \frac{L}{2}\right)^2 + \tau_0^2 + t^2 \leq \frac{L^2}{4}. \tag{5.10}$$

This agrees with the entanglement wedge in AdS/CFT. Refer to Fig. 8 for a sketch.

The fidelity $A_{1/2,1/2} = F(\rho, \rho')$ is computed as

$$A_{1/2,1/2} = \left[\frac{|w_2 - w_1||w_2' - w_1'|}{|w_2' - w_1||w_2 - w_1'|}\right]^{2h_\alpha}$$

$$= \left[\frac{|\tau_1 + \tau_2|^2|\tau_1' + \tau_2'|^2}{\left((x' - x)^2 + (\tau_1 + \tau_2')^2\right)\left((x' - x)^2 + (\tau_1' + \tau_2)^2\right)}\right]^{h_\alpha}. \tag{5.11}$$

This leads to the Bures metric in Euclidean space:

$$D_{\mathrm{B}}^2 = 2(1 - A_{1/2,1/2}) \simeq \frac{4h}{(\tau_1 + \tau_2)^2}(dx^2 + d\tau_1 d\tau_2). \tag{5.12}$$

We can actually see that this length coincides with the square of the minimal length between the geodesic which connects w_1 and w_2 and the one which connects w_1' and w_2'.
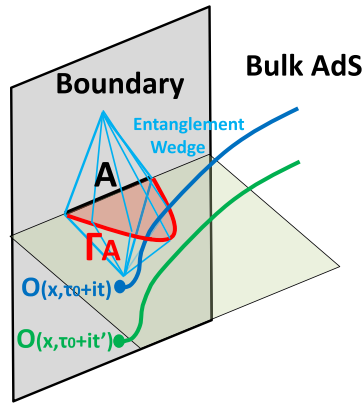
Fig. 8. The time evolution of a local excitation in CFT and entanglement wedge in the gravity dual.

If we substitute Eq. (5.1), then we have the Bures metric under the real time evolution:

$$D_{\mathrm{B}}^2 = \frac{h}{\tau_0^2}(dx^2 + dt^2).\qquad(5.13)$$

Notice that even though we consider the Lorentzian time t, the metric is positive definite as follows from the definition of the Bures metric. Refer to Appendix C for an analysis of the Bures metric in the more general time-dependent case.

6.   Double-interval case

Consider the reduced density matrix ρ_A in a 2d CFT when A consists of two disconnected intervals A_1 and A_2, which are parameterized as

$$A_1 = [0, s], \qquad A_2 = [l + s, l + 2s].\qquad(6.1)$$

Owing to the conformal invariance, this parameterization is enough to cover all possible configurations of the double intervals. Then, as in the single-interval case, we insert a local operator O_α at a point $w = x + i\tau$. This defines a reduced density matrix ρ_A, Eq. (1.1), for the locally excited state.

6.1.   Conformal map
We employ the following conformal transformation (analogous to the one in Refs. [53–55]) which maps a complex plane (the w-plane) with two slits along A_1 and A_2 into a cylinder (coordinate z):

$$z = f(w) = -J(\kappa^2)\left(\frac{1}{2K(\kappa^2)}\int_0^{\tilde{w}}\frac{dx}{\sqrt{(1 - x^2)(1 - \kappa^2 x^2)}} - \frac{1}{2}\right),\qquad(6.2)$$

where we have introduced

$$\tilde{w} = \frac{2}{l}\left(w - s - \frac{l}{2}\right),$$

$$J(\kappa^2) = 2\pi\frac{K(\kappa^2)}{K(1 - \kappa^2)},$$

$$K(\kappa^2) = \int_0^1\frac{dx}{\sqrt{(1 - x^2)(1 - \kappa^2 x^2)}},$$
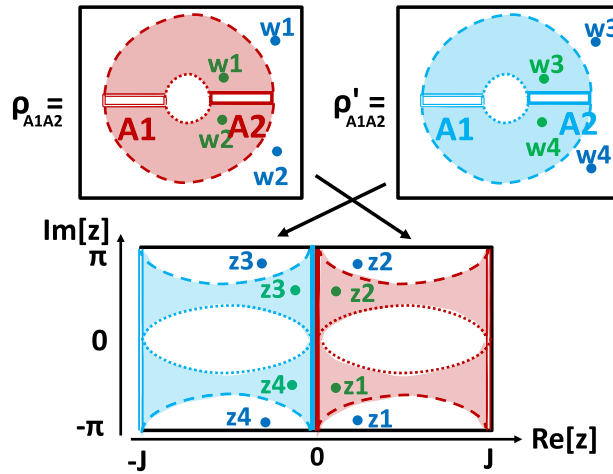
Fig. 9. The conformal mapping for the calculation of $\text{Tr}[\rho_A \rho'_A]$ in the double-interval case. Here we chose phase (i), where the entanglement is connected, as shown by the colored region. The lower picture describes the geometry after the mapping and represents a torus by identifying $\text{Im}[z] \sim \text{Im}[z] + 2\pi$ and $\text{Re}[z] \sim \text{Re}[z] + 2J$. The green (or blue) points describe the local excitations in the CFT which are dual to bulk excitations inside (or outside) the entanglement wedge M_A.

$$\kappa = \frac{l}{l + 2s}. \tag{6.3}$$

Note that we have

$$\frac{dz}{dw} = -\frac{2\pi}{lK(1 - \kappa^2)\sqrt{(1 - \tilde{w}^2)(1 - \kappa^2 \tilde{w}^2)}}. \tag{6.4}$$

Also notice that we are considering the analytical continuation of the integral given by the Jacobi elliptic function:

$$\int_0^{\tilde{w}} \frac{dx}{\sqrt{(1 - x^2)(1 - \kappa^2 x^2)}} = \text{sn}^{-1}(\tilde{w}, \kappa^2). \tag{6.5}$$

It is useful to note the relation

$$\text{sn}^{-1}(\tilde{w}, 0) = \arcsin(\tilde{w}). \tag{6.6}$$

Consider the calculation of $\text{Tr}[\rho \rho']$, where $\rho = \rho_A(w, \bar{w})$ and $\rho' = \rho_A(w', \bar{w}')$. Each of ρ and ρ' is described by the path integral on the complex plane with two slits. We can compute $\text{Tr}[\rho \rho']$ as the partition function on the space obtained by gluing the two complex planes along the slits. This is conformally mapped into a torus. This torus is constructed by gluing two cylinders: one of them describes ρ and is obtained by performing the transformation $z = f(w)$ in Eq. (6.2). The other corresponds to ρ' and is obtained from another transformation, $z = -f(w)$. These conformal maps take the original two-sheeted geometry into a torus, as depicted in Fig. 9. The horizontal and vertical length of the torus are given by $2J$ and 2π, respectively.

Finally, we find that $I(\rho, \rho')$ is given by the same formula as in the single-interval case, Eq. (3.13), where F is the torus four-point function. In the next subsection we study the CFT wedge geometry by focusing on holographic CFTs.

6.2.   CFT wedges from $I(\rho, \rho')$ in holographic CFTs

In holographic CFTs, we need to distinguish two phases depending on the moduli of the torus [26]:

(i) Connected phase: $J < \pi$, or equally $\kappa < 3 - 2\sqrt{2}$;
(ii) Disconnected phase: $J > \pi$, or equally $\kappa > 3 - 2\sqrt{2}$.

In phase (i), the entanglement wedge gets connected because $s^2 > (2s + l)l$, i.e. $S_{A_1} + S_{A_2} > S_{A_1 A_2}$. In this case, the AdS$_3$/CFT$_2$ duality tells us that the entanglement wedge M_A in the Poincaré AdS, Eq. (1.3), looks like

$$M_A^{\text{Con}} : \quad \frac{l^2}{4} \leq \left(x - s - \frac{l}{2}\right)^2 + \eta^2 \leq \left(\frac{l}{2} + s\right)^2 \tag{6.7}$$

on the time slice $\tau = 0$. In terms of the location of the local operator O_α insertion, the corresponding CFT wedge is expected to be

$$C_A^{\text{Con}} : \quad \frac{l^2}{4} \leq \left(x - s - \frac{l}{2}\right)^2 + \tau^2 \leq \left(\frac{l}{2} + s\right)^2 . \tag{6.8}$$

On the other hand, in phase (ii) the entanglement wedge gets disconnected as $s^2 < (2s + l)l$, i.e. $S_{A_1} + S_{A_2} < S_{A_1 A_2}$. In this case, the entanglement wedge M_A in the Poincaré AdS, Eq. (1.3), is found to be $M_A^{\text{Dis}} = M_A^{\text{Dis}(1)} \cup M_A^{\text{Dis}(2)}$, where

$$
\begin{aligned}
M_A^{\text{Dis}(1)} : \quad & \left(x - \frac{s}{2}\right)^2 + \eta^2 \leq \frac{s^2}{4}, \\
M_A^{\text{Dis}(2)} : \quad & \left(x - \frac{3s}{2} - l\right)^2 + \eta^2 \leq \frac{s^2}{4}.
\end{aligned}
\tag{6.9}
$$

The corresponding CFT wedge reads

$$
\begin{aligned}
C_A^{\text{Dis}(1)} : \quad & \left(x - \frac{s}{2}\right)^2 + \tau^2 \leq \frac{s^2}{4}, \\
C_A^{\text{Dis}(2)} : \quad & \left(x - \frac{3s}{2} - l\right)^2 + \tau^2 \leq \frac{s^2}{4}.
\end{aligned}
\tag{6.10}
$$

Now let us work out the CFT wedge from the calculation of $I(\rho, \rho')$ in holographic CFTs. The two-point functions on the torus in phases (i) and (ii) behave like

$$\langle O_\alpha^\dagger(z, \bar{z}) O_\alpha(z', \bar{z}')\rangle_{(i)} \simeq \left| \sin\left(\frac{\pi(z + 2\pi i n_1 - z')}{2J}\right)\right|^{-4h_\alpha} ,$$

$$\langle O_\alpha^\dagger(z, \bar{z}) O_\alpha(z', \bar{z}')\rangle_{(ii)} \simeq \left| \sinh\left(\frac{(z + 2J n_2 - z')}{2}\right)\right|^{-4h_\alpha} , \tag{6.11}$$

where we assumed that $\left|\sin\left(\frac{\pi(z + 2\pi i n - z')}{2J}\right)\right|$ takes the smallest value among all integer n at $n = n_1$ for phase (i) and $\left|\sinh\left(\frac{(z + 2J n_2 - z')}{2}\right)\right|$ takes the smallest value among all integer n at $n = n_2$ for phase (ii).

This expression for the two-point functions in Eq. (6.11) follows from the standard fact in AdS$_3$/CFT$_2$ that the gravity dual of the torus is given by a solid torus. We can construct the dual solid torus by filling the inside of the torus such that the circle Re[z] (or Im[z]) shrinks to zero size

in the bulk when we consider phase (i) (or (ii)). This is due to the well-known Hawking–Page phase transition [56], and matches perfectly with the large-c CFT analysis [26].

We can rewrite the value of $I(\rho, \rho')$ in holographic CFTs using the generalized free field approximation:

$$I(\rho, \rho') \simeq \frac{F(z_1, z_2, z'_3, z'_4)}{\sqrt{F(z_1, z_2, z_3, z_4)F(z'_1, z'_2, z'_3, z'_4)}}, \tag{6.12}$$

where

$$F(z_1, z_2, z'_3, z'_4) = \min\bigg[\langle O^\dagger_\alpha(z_1, \bar{z}_1)O_\alpha(z_2, \bar{z}_2)\rangle \langle O^\dagger_\alpha(z'_3, \bar{z}'_4)O_\alpha(z'_4, \bar{z}'_4)\rangle,$$

$$\langle O^\dagger_\alpha(z_1, \bar{z}_1)O_\alpha(z'_4, \bar{z}'_4)\rangle \langle O^\dagger_\alpha(z_2, \bar{z}_2)O_\alpha(z'_3, \bar{z}'_3)\rangle\bigg]. \tag{6.13}$$

The locations z_1, z_2 and z'_3, z'_4 of the operator insertions are depicted in Fig. 9, explicitly obtained via the map in Eq. (6.2) from the original insertion locations w_1, w_2 and w'_3, w'_4 in the double-sheeted geometry which describes the path integral of $\text{Tr}[\rho\rho']$.

When the true minimum is the first term in Eq. (6.13), i.e. the trivial contraction, we simply find $I(\rho, \rho') = 1$ and we cannot detect the local operator insertions. On the other hand, if the other one is favored as the minimum (i.e. the non-trivial contraction), then $I(\rho, \rho')$ becomes a non-trivial function of the locations of operator insertions.

The condition that the non-trivial contraction is favored is given by

$$\min\bigg[\bigg|\sin\bigg(\frac{\pi}{2J}(z_2 - z_1)\bigg)\bigg|, \bigg|\sin\bigg(\frac{\pi}{2J}(z_2 - z_1 - 2\pi i)\bigg)\bigg|\bigg] \geq \bigg|\sin\bigg(\frac{\pi}{2J}(z_3 - z_2)\bigg)\bigg| \tag{6.14}$$

in the connected case (i), and by

$$\bigg|\sinh\bigg(\frac{1}{2}(z_2 - z_1)\bigg)\bigg| \geq \min\bigg[\bigg|\sin\bigg(\frac{1}{2}(z_2 - z_3)\bigg)\bigg|, \bigg|\sin\bigg(\frac{1}{2}(z_2 - z_3 - 2J)\bigg)\bigg|\bigg] \tag{6.15}$$

in the disconnected case (ii).

We plot the parameter region of (x, τ), where the non-trivial contraction is favored, in Fig. 10 for the connected phase (i) and Fig. 11 for the disconnected phase (ii).

In both cases, the region is very close to the true entanglement wedge, Eq. (6.8). The deviation is interestingly very small (within a few percent), and is sketched in Fig. 12. The wedge derived from $I(\rho, \rho')$ in the holographic CFT can be larger or smaller than the true entanglement wedge in AdS/CFT, depending on the situation. Notice that these deviations are leading order in our computational scheme, i.e. $1/c$ expansions, and thus we cannot regard them as quantum corrections in gravity. Rather, it is an essential feature of the Rényi-like measure $I(\rho, \rho')$. We will comment on possible interpretations of this phenomenon in later subsections.

6.3. *Plots of $I(\rho, \rho')$ in holographic CFTs*

We also explicitly plot the values of $I(\rho, \rho')$ as a function of w' (the location of operator insertion of ρ'_A) when we fix w (the location of operator insertion of ρ_A) for both the connected (upper two pictures) and the disconnected (lower two pictures) cases in Fig. 13. In both plots, the left graphs show the plots when we fix w to be inside the wedge. In this case we find a sharp peak of $I(\rho, \rho')$, which reaches the maximum $I(\rho, \rho') = 1$ only when $w' = w$. In the right graphs, w is outside the wedge. We see that $I(\rho, \rho') = 1$ when w' is also outside the wedge, while we have $I(\rho, \rho') = 0$
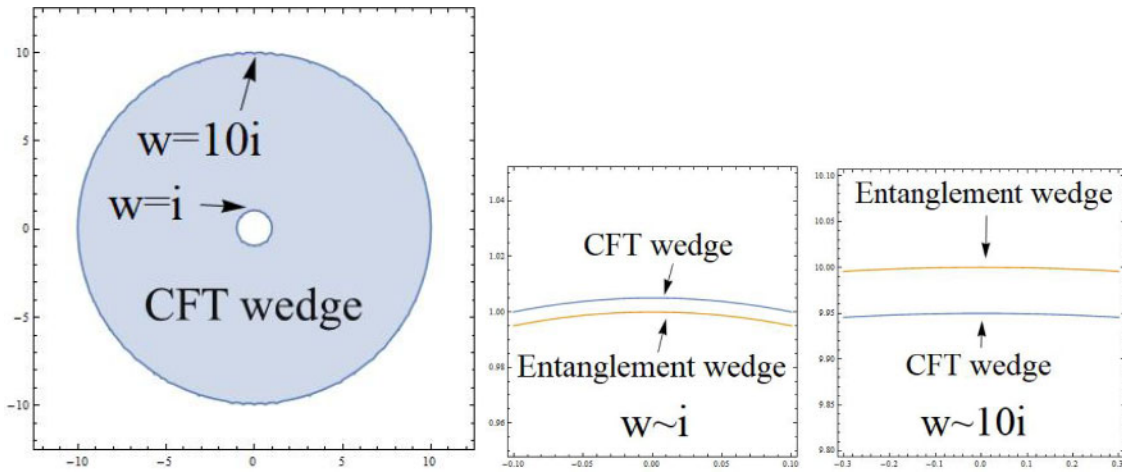
Fig. 10. The location of the local operator on the $\tilde{w}$-plane where the non-trivial contraction is favored (left), and its deviation from the entanglement wedge (middle and right). We set $\kappa = 0.1$, where the entanglement wedge is connected, i.e. phase (i). The blue curves are the borders between the non-trivial and trivial contraction. The orange line in the right picture describes the entanglement wedge.
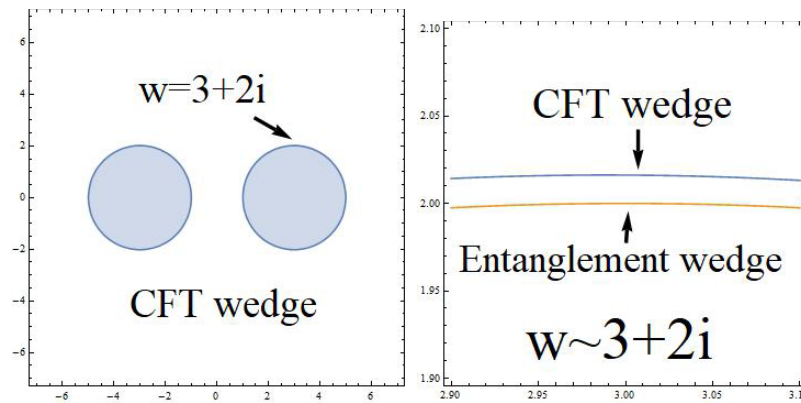
Fig. 11. The location of the local operator on the $\tilde{w}$-plane where the non-trivial contraction is favored (left), and its deviation from the entanglement wedge (right). We set $\kappa = 0.2$, where the entanglement wedge is disconnected, i.e. phase (ii). The blue curves are the borders between the non-trivial and trivial contraction. The orange line in the right picture describes the entanglement wedge.
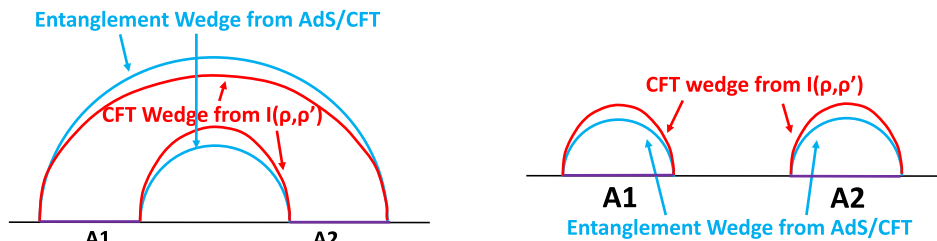
Fig. 12. The small deviation between the CFT wedge (red) based on $I(\rho, \rho')$ and the correct entanglement wedge in AdS/CFT. The left and right pictures correspond to the connected and disconnected phases.
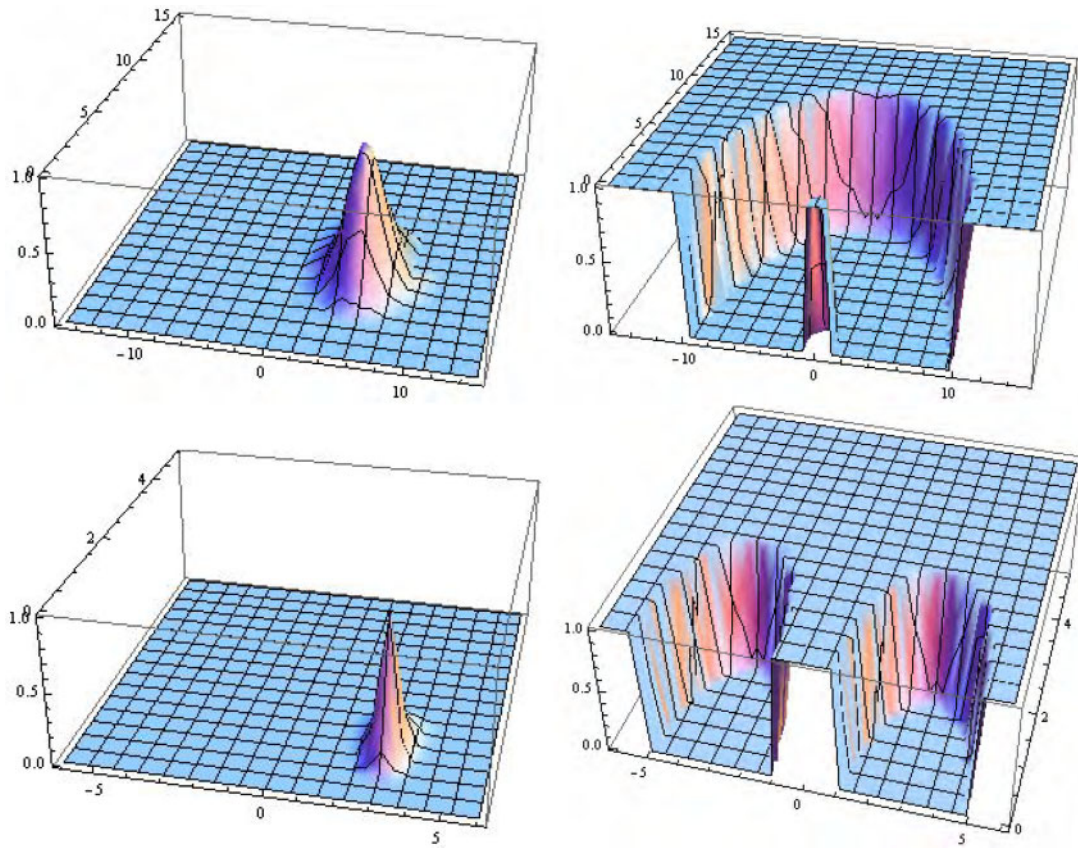
**Fig. 13.** The values of $I(\rho, \rho')$ as a function of Re[w'] (horizontal) and Im[w'] (depth) for fixed values of w when the subsystem A consists of double intervals. In the upper two pictures $\kappa = 0.1$ (connected phase), and in the lower ones $\kappa = 0.2$ (disconnected phase). In the upper left and right pictures, $w = 5 + 5i$ (inside the wedge) and $w = 5 + 20i$ (outside the wedge), respectively. In the lower left and right pictures, $w = 3 + i$ (inside the wedge) and $w = i$ (outside the wedge), respectively.

when w' is inside the wedge. All of these agree with the expectation from AdS/CFT, neglecting the small deviation previously discussed.

6.4.   CFT wedge from $I(\rho, \rho')$ for the complement

It is instructive to also consider the behavior of CFT wedges for the reduced density matrix ρ_B, where B is the complement of the subsystem A. We again focus on CFT wedges based on $I(\rho, \rho')$. The calculation of Tr[$\rho_B \rho'_B$] is very similar to the previous one of Tr[$\rho_A \rho'_A$], as depicted in Fig. 14. The only, but very important, difference is that the locations of z_2 and z_4 are flipped. Therefore, the conditions of non-trivial Wick contraction are simply opposite to each other: when we need to take the non-trivial one for Tr[$\rho_A \rho'_A$], we need to take the trivial one for Tr[$\rho_B \rho'_B$], and vice versa. Therefore, the CFT wedge for ρ_B is just the complement of that for ρ_A.

This relation helps us to understand the behavior in Fig. 12. First of all, when the CFT wedge for $A = A_1 \cup A_2$ is disconnected, it is clear that the CFT wedge C_A should be larger than or equal to that for the union of the CFT wedges C_{A_1} and C_{A_2}, as the information included in ρ_A is greater than that in the union of ρ_{A_1} and ρ_{A_2}. This explains the right picture of Fig. 12. Also, this requirement is trivially satisfied in the left picture.
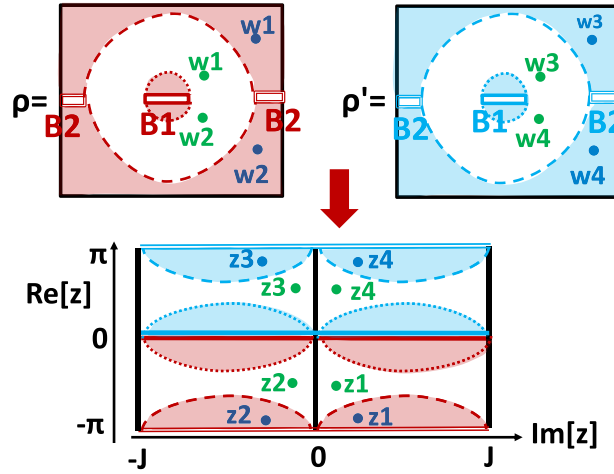
Fig. 14. The conformal transformation for the calculation of $\text{Tr}[\rho_B \rho'_B]$ in the double-interval case assuming phase (i), where the entanglement wedge B is disconnected, as depicted by the colored region. The lower picture describes the geometry after the transformation, given by a torus by identifying $\text{Im}[z] \sim \text{Im}[z] + 2\pi$ and $\text{Re}[z] \sim \text{Re}[z] + 2J$. The green (or blue) points correspond to the local excitation in the CFT which is dual to the bulk excitation outside (or inside) the entanglement wedge M_B.

To better understand the left picture in Fig. 12, let us consider the complement of A, i.e. $B = B_1 \cup B_2$. Since the wedge of B is disconnected when that for A is connected, we can apply the same rule, i.e. C_B should be larger than or equal to the union of C_{B_1} and C_{B_2}. As we just showed, we also know that C_B is the complement of C_A. These two facts lead to the behavior of the left picture in Fig. 12.

6.5.   The Bures distance in holographic CFTs

In the double-interval case we found that the CFT wedge defined by the distinguishablity measure $I(\rho, \rho')$ does not precisely agree with the expected entanglement wedge from AdS/CFT, though the deviations are very small. This motivates us to study CFT wedges for the Bures distance $D_B(\rho, \rho')$, Eq. (2.11), or equally the fidelity $F(\rho, \rho')$, Eq. (2.1), which is expected to be the ideal distinguishablity measure. As we will see below, the CFT wedge for D_B precisely agrees with the correct entanglement wedge.

The fidelity can be computed from the analytical continuation $A_{1/2,1/2}$ of $A_{n,m}$, Eq. (4.1), via a replica-like method. Even though it is very difficult to evaluate $A_{n,m}$ for general integers n and m, we can heuristically obtain analytical results in the limit $n \to 1/2$ and $m \to 1/2$ as follows. First, notice the useful property shown in Refs. [27,28] that the vacuum replica partition function of a holographic CFT with $k \sim 1$ can be approximated by[2]

$$Z_{\Sigma_k([0,s]\cup[l+s,l+2s])} \xrightarrow[c\to\infty]{} \begin{cases} Z_{\Sigma_k([0,l+2s])}Z_{\Sigma_k([s,l+s])}, & \text{(i) connected phase: } s^2 > (2s+l)l, \\ Z_{\Sigma_k([0,s])}Z_{\Sigma_k([l+s,l+2s])}, & \text{(ii) disconnected phase: } s^2 < (2s+l)l, \end{cases}$$

$$(6.16)$$

where $\Sigma_k([a,b])$ means the k-sheeted manifold with a cut along the interval $[a,b]$, and $Z_{\Sigma_k([a,b])}$ is the vacuum partition function on that manifold.

---

[2] If k is enough large, then we need to take the contributions from the descendants into account. We can consider this by making use of Virasoro conformal blocks.
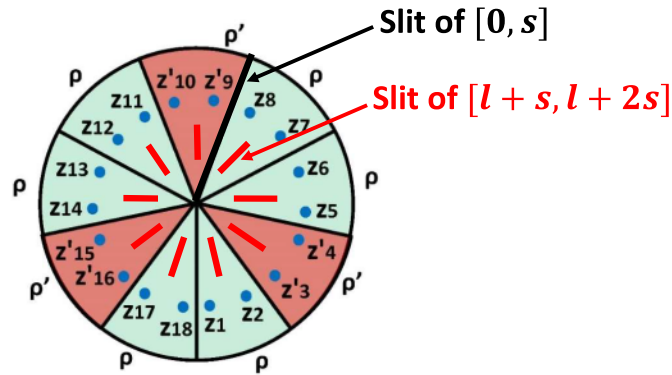
Fig. 15. The complex plane which describes the path integral that calculates the trace $A_{n,m} = \mathrm{Tr}[(\rho^m \rho' \rho^m)^n]$, i.e. Eq. (4.1), where we performed the conformal transformation of Eq. (4.3) with $L = s$. Here, we choose $m = 1$ and $n = 3$ for convenience. Now that we consider the double-interval case, we have cuts associated with the slit $[l + s, l + 2s]$ (the red solid lines).

Indeed, the limit of fidelity $n \to 1/2$ and $m \to 1/2$ corresponds to $k \to 1$, as is clear from the relation in Eq. (4.4). Therefore, we can factorize the computation of the fidelity $F(\rho, \rho')$ into two correlation functions, each of which includes a single interval. In this sense the calculations are reduced to the fidelity in the single-interval case, which we already worked out, e.g. in Eqs. (4.13) and (4.16). A CFT wedge in the single-interval case is bounded by a semicircle, which agrees with the correct entanglement wedge.

We can illustrate this factorization from another viewpoint. If one wants to probe the disconnected entanglement wedge $[0, s]$, one may consider the conformal transformation in Eq. (4.3) with $L = s$. This leads to the geometry shown in Fig. 15, which has "cuts" associated with the slit $[l + s, l + 2s]$ (the red solid lines in the figure). Although these cuts give non-trivial contributions to the $2k$-point function in general, these contributions can be neglected in the limits $n = m \to 1/2$. Therefore, we can evaluate this $2k$-point function in the same way as the single-interval case, which means that the result just reduces to Eq. (4.16).

In this way, owing to the factorization in Eq. (6.16), we can conclude that the CFT wedges $C^{(\mathrm{B})}$ calculated from the Bures distance (or equally fidelity) coincide with the expectations from the entanglement wedges: Eq. (6.8) in the connected case and Eq. (6.10) in the disconnected case. It is also clear that the Bures metric in the double-interval case also agrees with the AdS metric as in the single-interval case, when the locations of operator insertions are inside the wedge.

6.6. Interpretation of the two different CFT wedges $C_A^{(I)}$ and $C_A^{(\mathrm{B})}$

So far, we have seen the calculations of two distinguishability measures $I(\rho, \rho')$ and $F(\rho, \rho')$ in the double-interval case. Entanglement wedges in AdS/CFT are precisely reproduced from the latter, i.e. the fidelity, while the former predicts CFT wedges which are slightly distorted from the actual entanglement wedges. Here, we discuss why CFT wedges depend on the choice of these distinguishability measures.

First, remember that $I(\rho, \rho')$ is essentially the calculation of $\mathrm{Tr}[\rho \rho']$, and the fidelity $F(\rho, \rho')$ is equal to $\mathrm{Tr}\left[\sqrt{\sqrt{\rho} \rho' \sqrt{\rho}}\right]$. In this sense the total power of the density matrices (for this we identify ρ and ρ') is two for the former and one for the latter.

A measurement of a physical quantity is described by $\langle O_i \rangle = \text{Tr}[\rho O_i]$. In the classical gravity limit of AdS/CFT, we restrict the operators O_i to low-energy ones. Therefore, we expect that the entanglement wedge should be determined by the distinguishability of low-energy states (or so-called code subspaces [19,20]).

In this sense, the quantity $\text{Tr}[\rho\rho']$ goes beyond the low-energy approximation as $O_i = \rho'$ is a highly excited operator. A reduced density matrix can be expressed as $\rho_A = e^{-H_A}$ in terms of the modular Hamiltonian H_A. For a CFT vacuum, for example, H_A is given by an integral of the energy stress tensor. Therefore, $\rho_A = e^{-H_A}$ includes an infinite number of energy stress tensors, which are clearly outside of the low-energy states.

On the other hand, when we calculate the Bures metric the fidelity $F(\rho, \rho')$ distinguishes low-energy states when ρ is very close to ρ'. We argue that the above different property of distinguishing states causes the difference of CFT wedges between $I(\rho, \rho')$ and $F(\rho, \rho')$. This also explains why the latter agrees with the expectation from the actual entanglement wedge in AdS/CFT. We will explore differences of CFT wedges for various other distance measures Sect. 9.

7.   Entanglement wedges from AdS/BCFT

Here, we consider a quantum state $|\Psi\rangle$ in a CFT on a 2d space with boundaries, called BCFT, given by

$$|\Psi_{\text{bdy}}\rangle = e^{-\frac{\beta}{4}H}|B\rangle. \tag{7.1}$$

Its gravity dual is given by the AdS/BCFT construction [23–25] via the holography.

This is the initial state of the global quantum quench [57] using the boundary state $|B\rangle$ (i.e. the Cardy state [58]). We choose the subsystem A to be the interval $[0, L]$ as before. The reduced density matrix $\rho_A = \text{Tr}_B[|\Psi_{\text{bdy}}\rangle\langle\Psi_{\text{bdy}}|]$ is computed as the path integral on a strip $-\frac{\beta}{4} \leq \tau \leq \frac{\beta}{4}$. We describe this space by the coordinate $w = x + i\tau$; see the upper pictures in Fig. 16.
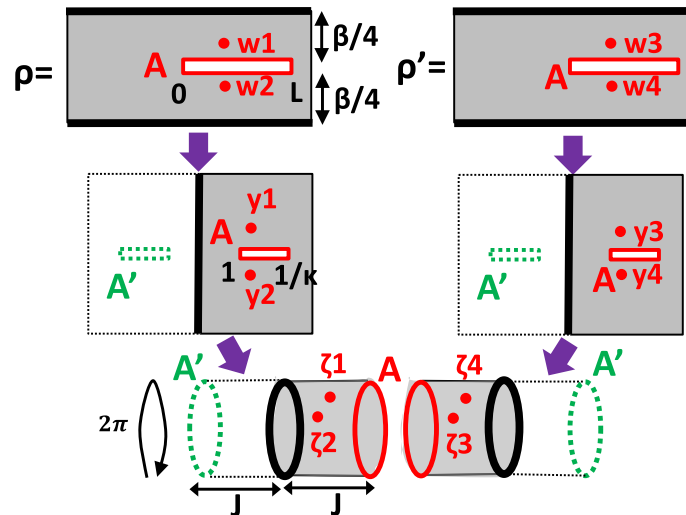
Fig. 16.   The conformal transformation for the calculation of $\text{Tr}[\rho_A \rho'_A]$ in the BCFT setup. The upper pictures describe the setup in the original w coordinate. The red slit describes the subsystem A. The thick black lines describe the boundaries. They are mapped into the y coordinate as shown in the middle pictures. Finally, they are mapped into cylinders as shown in the lower pictures. To calculate the trace $\text{Tr}[\rho_A \rho'_A]$, we identify the two red circles, which describe the subsystem A, and the final geometry becomes a cylinder.

Next, we transform by the conformal map

$$y = e^{\frac{2\pi}{\beta} w},\tag{7.2}$$

so that the w-plane is mapped into a half-plane, as in the middle pictures in Fig. 16. In this coordinate, the subsystem A is the interval $[1, e^{\frac{2\pi L}{\beta}}]$.

Finally, we introduce a new cylindrical coordinate ζ via the elliptic map

$$\zeta = \frac{\pi}{K(1 - \kappa^2)} \int_0^y \frac{d\tilde{y}}{\sqrt{(1 - \tilde{y}^2)(1 - \kappa^2 \tilde{y}^2)}} = \frac{\pi}{K(1 - \kappa^2)} \cdot \mathrm{sn}^{-1}(y, \kappa^2),\tag{7.3}$$

where we have defined

$$\kappa = e^{-\frac{2\pi L}{\beta}} \quad (< 1).\tag{7.4}$$

See the lower pictures in Fig. 16.

7.1.   *Phase transitions of entanglement wedges in AdS/BCFT*

We expect that the state in Eq. (7.1) is dual to half of the eternal BTZ geometry [59]. In the Euclidean setup, it is identical to the geometry given by the metric in Eq. (4.24). In the AdS/BCFT (see Refs. [23–25] for details), the gravity dual of a BCFT state is found by adding a boundary surface into an AdS space, which extends to the bulk.

There are two phases in the holographic calculation of the entanglement entropy S_A which follows from the prescription of AdS/BCFT: (a) the connected geodesic Γ_{con} is favored, and (b) the disconnected geodesics Γ_{dis} which end on the horizon are favored. Accordingly, the geometry of the entanglement wedge changes between (a) and (b). Since the length of the connected and disconnected geodesic is computed from the explicit form of the geodesic, Eq. (4.33), as

$$|\Gamma_{\mathrm{con}}| = 2 \int_{\rho_*}^{\rho_\infty} d\rho \frac{\cosh \rho}{\sqrt{\cosh^2 \rho - \cosh^2 \rho_*}} = \left[\mathrm{arctanh} \left(\frac{\sinh \rho}{\sqrt{\cosh^2 \rho - \cosh^2 \rho_*}} \right) \right]_{\rho_*}^{\rho_\infty}$$

$$= \rho_\infty - \log \sinh \rho_*,\tag{7.5}$$

$$|\Gamma_{dis}| = 2 \int_0^{\rho_\infty} d\rho = \rho_\infty,\tag{7.6}$$

where the constant ρ_* is related to L via

$$\cosh \rho_* \tanh \left(\frac{\pi L}{\beta} \right) = 1,\tag{7.7}$$

phases (a) and (b) correspond to the regions

$$\text{phase (a) } \Gamma_{\mathrm{con}}: \quad \sinh \rho_* > 1 \quad \leftrightarrow \quad \sinh \left(\frac{\pi L}{\beta} \right) < 1 \quad \leftrightarrow \quad \kappa = e^{-\frac{2\pi L}{\beta}} > 3 - 2\sqrt{2};$$

$$\text{phase (b) } \Gamma_{\mathrm{dis}}: \quad \sinh \rho_* < 1 \quad \leftrightarrow \quad \sinh \left(\frac{\pi L}{\beta} \right) > 1 \quad \leftrightarrow \quad \kappa = e^{-\frac{2\pi L}{\beta}} < 3 - 2\sqrt{2}.\tag{7.8}$$

This is the same condition we encounter in the case of a double interval. This is not a coincidence, and indeed we find that the ratio of the horizontal length and vertical length of the cylinder of the ζ coordinate in Fig. 16 is given by $\frac{\pi}{J} = \frac{K(1-\kappa^2)}{2K(\kappa^2)}$, which is the same ratio as appears in Fig. 9. Indeed,
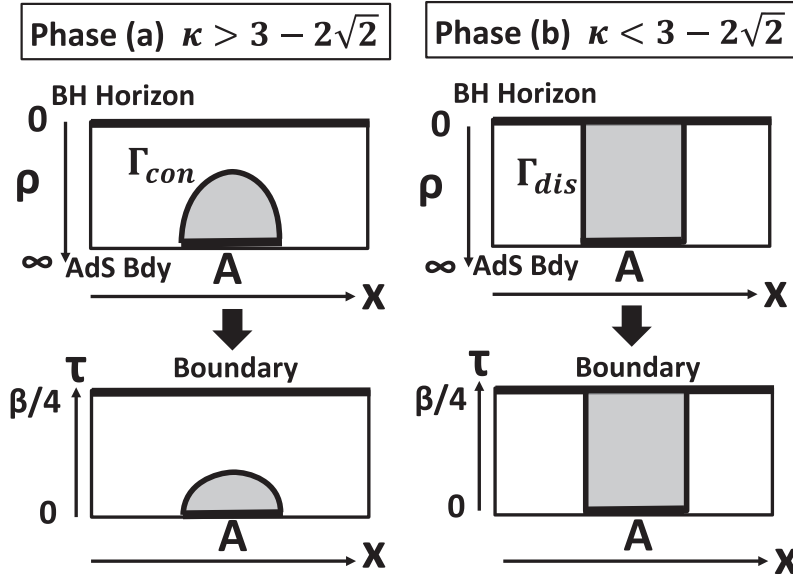
Fig. 17. The entanglement wedges in AdS/BCFT in phases (a) and (b). The upper pictures describe the geometry of the entanglement wedge (gray region) in the time slice of the BTZ black hole. The lower pictures show the wedge geometry in the CFT dual, Eq. (4.32), in the w-plane by the geodesic projection.

it is a cylinder with circumference 2π and length $J = 2\pi \frac{K(\kappa^2)}{K(1-\kappa^2)}$. Via the doubling trick this can be extended as a torus, with the periodicities given by 2π and $2J$.

In this way, the reduced density matrix analysis provides the phase transition of the entanglement wedge at the correct value of subsystem size. The expected entanglement wedge geometry from AdS/BCFT is shown in Fig. 17.

7.2. Wick contractions and distinguishability

Now we come back to the evaluation of $I(\rho_A, \rho'_A)$. This is given by the four-point functions as

$$I(\rho_A, \rho'_A) = \frac{F(\zeta_1, \zeta_2, \zeta'_3, \zeta'_4)}{\sqrt{F(\zeta_1, \zeta_2, \zeta_3, \zeta_4) F(\zeta'_1, \zeta'_2, \zeta'_3, \zeta'_4)}}, \tag{7.9}$$

where F denotes the four-point function on the cylinder in the ζ coordinate,

$$F(\zeta_1, \zeta_2, \zeta_3, \zeta_4) = \langle O_\alpha^\dagger(\zeta_1) O_\alpha(\zeta_2) O_\alpha^\dagger(\zeta_3) O_\alpha(\zeta_4) \rangle. \tag{7.10}$$

Note that this four-point function is defined on the cylinder.

In the generalized free field prescription, we can evaluate this four-point function via Wick contractions. There are three possible Wick contractions: (i) trivial contraction, (ii) non-trivial contraction, and (iii) boundary contraction, as depicted in Fig. 18. The third one is new, and is the contraction between each point of ζ_i ($i = 1, 2, 3, 4$) and its mirror point ζ'_i due to the presence of the boundary.

In phase (a) we have $J > \pi$, and thus the state is dual to the BTZ black hole on an interval $-J \leq \text{Re}\, \zeta \leq J$, where $\text{Im}\, \zeta$ is the Euclidean time. Therefore, the two-point function behaves as

$$\langle O_\alpha(\zeta) O_\alpha(\zeta') \rangle = \sinh\left(\frac{\zeta_1 - \zeta_2}{2}\right)^{-4h_\alpha} \equiv G_a(\zeta - \zeta'). \tag{7.11}$$
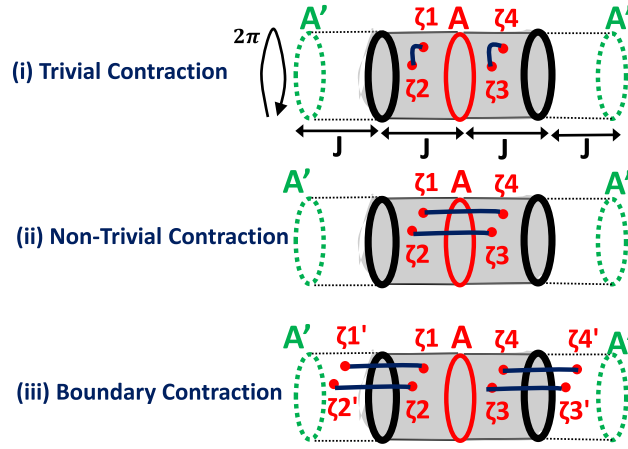
Fig. 18. The three possibilities for Wick contractions in holographic BCFTs.

In phase (b), since $J < \pi$ the state is dual to a global AdS$_3$ on an interval $-J \leq \mathrm{Re}\,\zeta \leq J$, where $\mathrm{Im}\,\zeta$ is the Euclidean time. Therefore, the two-point function behaves as

$$\langle O_\alpha(\zeta) O_\alpha(\zeta') \rangle = \sin\left(\frac{\pi(\zeta_1 - \zeta_2)}{2J}\right)^{-4h_\alpha} \equiv G_b(\zeta - \zeta'), \tag{7.12}$$

where $J = 2\pi K(\kappa^2)/K(1 - \kappa^2)$.

It is obvious that we obtain $I(\rho_A, \rho'_A) = 1$ (i.e. ρ_A and ρ'_A are indistinguishable) when contraction (i) or (iii) is favored. We can distinguish ρ_A and ρ'_A, i.e. $I(\rho_A, \rho'_A) < 1$, when the non-trivial contraction (ii) is favored. The condition that the non-trivial contraction (ii) is favored is:

(ii) is more favored than (i): $G(\zeta_1 - \zeta_4) \gg G(\zeta_1 - \zeta_2)$;

(ii) is more favored than (iii): $G(\zeta_1 - \zeta_4) \gg G(\zeta_1 - \zeta'_1)$, \qquad (7.13)

when h_α is very large.

In phase (a) they are equivalent to the condition

$$\text{(ii) is more favored than (i):} \quad \left| \sinh\left[\frac{\zeta_1 - \zeta_4}{2}\right] \right| < \left| \sinh\left[\frac{\zeta_1 - \zeta_2}{2}\right] \right|; \tag{7.14}$$

$$\text{(ii) is more favored than (iii):} \quad \left| \sinh\left[\frac{\zeta_1 - \zeta_4}{2}\right] \right| < \left| \sinh\left[\frac{\zeta_1 - \zeta'_1}{2}\right] \right|. \tag{7.15}$$

We numerically plot this region in the left panel of Fig. 19. If we ignore the boundary contributions, this CFT wedge is very close to the actual entanglement wedge from AdS/CFT as depicted in the right panel of Fig. 19. This small deviation is because we are actually employing the measure $I(\rho, \rho')$ which has the unwanted property that it is also sensitive to high-energy states. In other words, if we utilize the Bures metric instead, we can reproduce the expected CFT wedges which agree with the entanglement wedges. This situation is the same as that discussed in Sect. 6.6 for the example of double intervals.

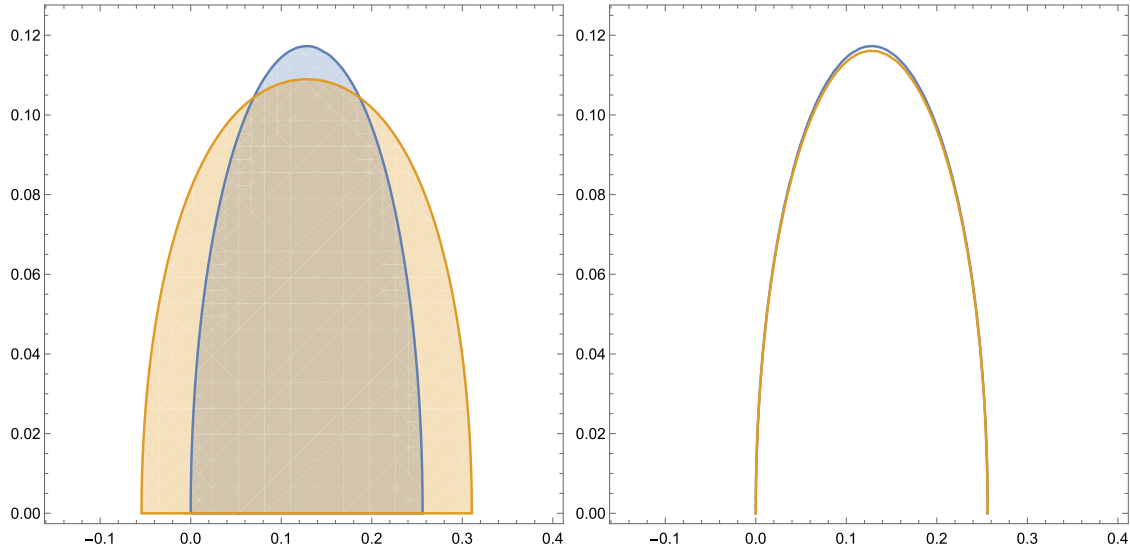In phase (b), they are equivalent to the conditions

$$\text{(ii) is more favored than (i):} \quad \left| \sin\left[\frac{\zeta_1 - \zeta_4}{2}\right] \right| < \left| \sin\left[\frac{\zeta_1 - \zeta_2}{2}\right] \right|, \tag{7.16}$$

Fig. 19. Γ_{con}, the region where the non-trivial Wick contraction (ii) is favored, is shown for phase (a) with $\kappa = 1/5$ and $\beta = 1$. In the left picture, the blue region corresponds to Eq. (7.14) and the orange region corresponds to Eq. (7.15). The distinguishable region is the overlap between them. In the right picture the blue curve is the border of Eq. (7.14), while the orange curve is the expected entanglement wedge profile, Eq. (4.32), from the AdS/CFT. We observe a very small deviation between them.

$$\left|\sin\left[\frac{\zeta_1 - \zeta_4}{2}\right]\right| < \left|\sin\left[\frac{2\pi - \zeta_1 + \zeta_2}{2}\right]\right|; \qquad (7.17)$$

(ii) is more favored than (iii): $\quad \left|\sin\left[\frac{\zeta_1 - \zeta_4}{2}\right]\right| < \left|\sin\left[\frac{\zeta_1 - \zeta_1'}{2}\right]\right|. \qquad (7.18)$

This region is plotted numerically in Fig. 20. The resulting CFT wedge is largely different from that expected from the entanglement wedge. However, if we are allowed to ignore the boundary contribution (i.e. the constraint to the green region), this CFT wedge is the same as the actual entanglement wedge from AdS/CFT. In other words, we can reproduce the correct geometry of the entanglement wedge only when the one-point function $\langle O_\alpha \rangle_{\text{bdy}}$ vanishes. This is because in this case the boundary contraction (iii) is not allowed. If the boundary one-point function does not vanish, then we get the smaller wedge from the holographic CFT rather than the correct entanglement wedge; see Fig. 21.

Even though when $\langle O_\alpha \rangle_{\text{bdy}} \neq 0$ the CFT wedge does not agree with the entanglement wedge in AdS/CFT, this discrepancy is present even when A is the total system (i.e. the pure state). In other words, we cannot probe points near the black hole horizon by two-point functions dual to the geodesic which connects two boundary points. This is simply because the two-point function gets factorized into one-point functions when the points are close to the boundaries of BCFT. Therefore, this means that we cannot employ our original idea that we probe the bulk geometry by two-point functions when $\langle O_\alpha \rangle_{\text{bdy}}$ does not vanish. In this sense, we should not think the above discrepancy shows that the CFT predicts an entanglement wedge which differs from the AdS/CFT prediction. Rather, we need to find a better CFT quantity which can probe the bulk geometry.[3]

---

[3] If we turn to a setup of a pure state black hole created by a heavy operator O_H [60], we may avoid the mentioned problem because the two-point function $\langle O_H O_\alpha \rangle$ is vanishing.
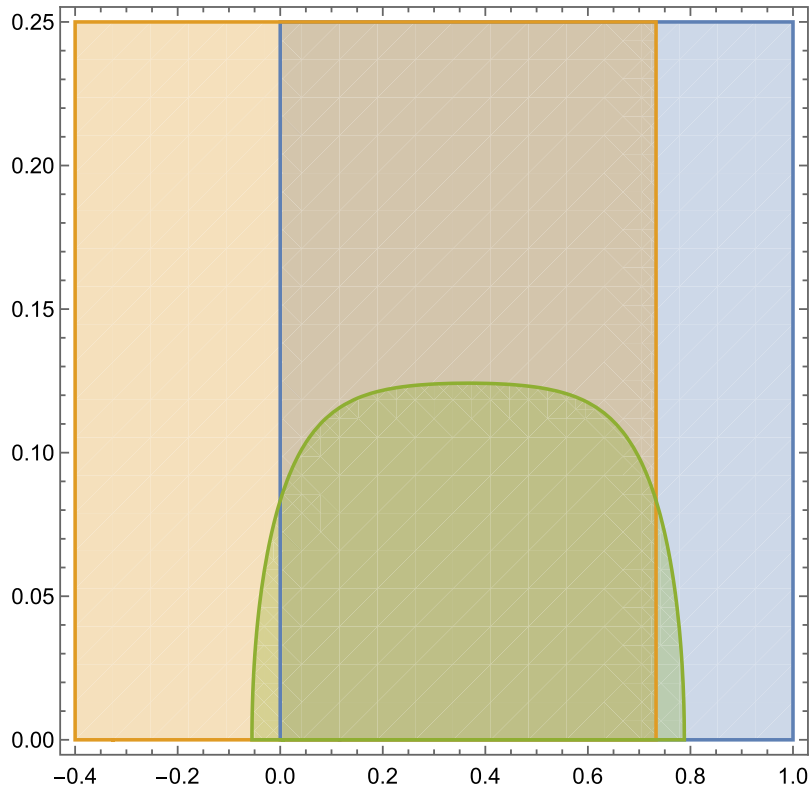
Fig. 20. Γ_{dis}, the region where the non-trivial Wick contraction (ii) is favored, is shown for phase (b) with $\kappa = 1/10$ and $\beta = 1$. In the left picture, the blue, orange, and green regions correspond to Eqs. (7.16), (7.17), and (7.18), respectively. The distinguishable region is the overlap between these three regions.
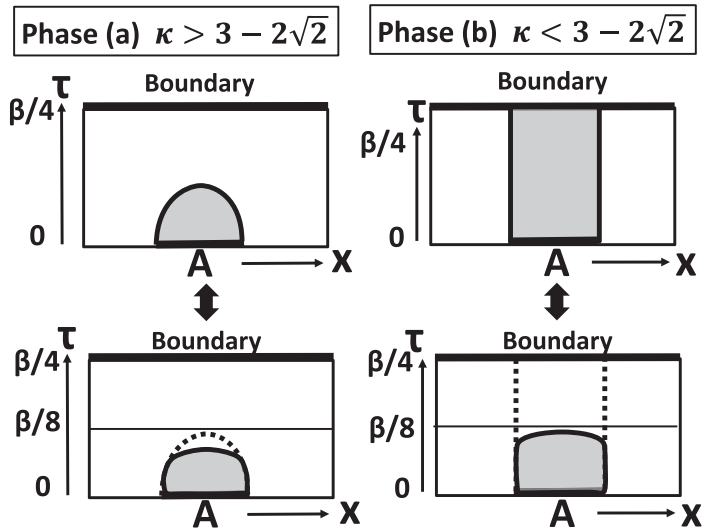
Fig. 21. The CFT wedges in phase (a) (left) and phase (b) (right). The upper wedges are obtained from Eqs. (7.14), (7.16), and (7.17). For the lower wedges we impose Eqs. (7.15) and (7.18) in addition. In phase (b), i.e. the right two pictures, the upper and lower panels correspond to $\langle O_\alpha \rangle_{\text{bdy}} = 0$ and $\langle O_\alpha \rangle_{\text{bdy}} \neq 0$, respectively.

The entanglement wedge in AdS/BCFT which ends on the boundary surface as in the upper right picture of Fig. 17 plays a crucial role in a recent explanation of the black hole information paradox [61–66], where a region of the entanglement wedge near the boundary surface is called the islands. When $\langle O_\alpha \rangle_{\text{bdy}} = 0$, our arguments above support the entanglement reconstruction relevant to this interesting problem.

7.3. Thermofield double state

The thermofield double (TFD) state also provides a closely related but different setup of AdS/CFT. It is given by the pure state in the direct product of two identical CFT Hilbert spaces, $\mathcal{H}_1 \otimes \mathcal{H}_2$:

$$|\text{TFD}\rangle = \frac{1}{Z_{\text{TH}}} \sum_n e^{-\beta E_n/2} |n\rangle_1 |n\rangle_2, \tag{7.19}$$

where $|n\rangle$ is the energy eigenstate with energy E_n, and $Z_{\text{TH}} = \sum_n e^{-\beta E_n}$ is the thermal partition function. When we trace out either one of the Hilbert spaces, the reduced density matrix coincides with the canonical distribution. As discovered in Ref. [67], this pure state $|\text{TFD}\rangle$ is dual to the eternal AdS black hole. In AdS$_3$/CFT$_2$, the dual geometry is given by the eternal BTZ solution, which is obtained by continuing the Lorentzian geometry inside the horizon and which has two asymptotically AdS boundaries. The two boundaries correspond to the first and second CFTs. In the well-known path integral formulation, the state in Eq. (7.19) is described by a strip with width $\beta/2$ in the Euclidean time direction, while the space direction is an infinite line. The boundary conditions on the two boundaries of the strip are arguments of two CFTs, which in total represent the wave functional of the TFD state.

Let us choose subsystem A in the first CFT at $\tau = 0$ and subsystem A' in the second CFT at $\tau = -\beta/2$. For simplicity, we choose A and A' to be symmetric with respect to the middle line $\tau = -\beta/4$. In this setup, if we artificially take a Z_2 quotient $\tau \to \pi/2 - \tau$, then we get back to the previous example of the global quantum quench, Eq. (7.1). Thus, the mathematical structures are very similar.

Consider the CFT wedge for the union of these two subsystems AA' in the TFD state. The entanglement wedge from CFT is simply given by doubling that for the global quench (see Fig. 17) across the horizon, utilizing the Z_2 symmetry.

The calculation of the measure $I(\rho, \rho')$ in CFT can be done by doubling the cylinder into a torus, as depicted in Fig. 16, where the dotted green circle represents the subsystem A'. Therefore, we find that the phase transition structure, i.e. the connected phase (a) and the disconnected phase (b), is identical. Moreover, the CFT wedge is determined by the condition that the non-trivial Wick contraction is favored over the trivial one. Notice that boundary contractions are not allowed as we do not have any boundaries in our CFT, as opposed to the previous example. Because of this, we find that the CFT wedge in the connected phase agrees with the entanglement wedge up to a very small deviation, which can be confirmed in the right picture of Fig. 19. In the disconnected phase, the CFT wedge perfectly agrees with the entanglement wedge, as confirmed from Fig. 21. This small deviation for the connected case is again due to the measure $I(\rho, \rho')$, and should be absent in the CFT wedges for the Bures metric, as in Sect. 6.6 for the example of double intervals.

8. Higher-dimensional case

Here we derive the entanglement wedge in higher-dimensional AdS/CFT. Consider a $(d + 1)$-dimensional holographic CFT on $\mathbb{R}^{d+1}$ dual to AdS$_{d+2}$. We write the coordinates of $\mathbb{R}^{d+1}$
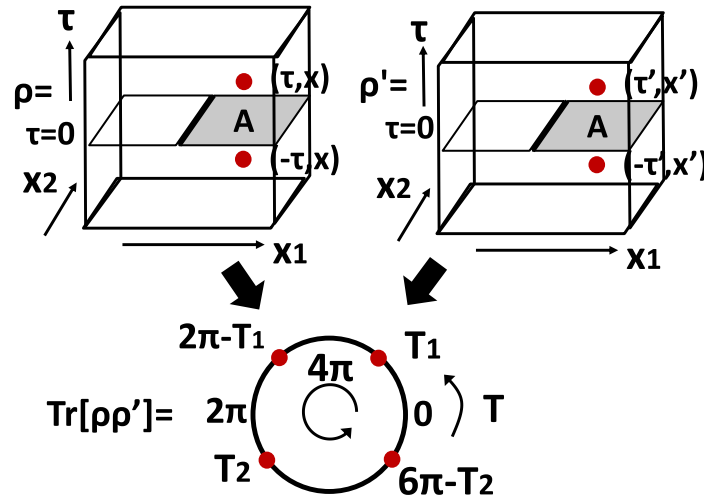
Fig. 22. The computation of $\text{Tr}[\rho\rho']$ in a three-dimensional CFT.

as $(\tau, x_1, \ldots, x_d)$. Consider the reduced density matrix of the locally excited state $\rho_A = \text{Tr}_B\left[O_\alpha(\tau, x)|0\rangle\langle 0|[O_\alpha(\tau, x)]^\dagger\right]$ as before. We first analyze the case where the subsystem A is a half-plane, and later extend the results to the case where A is a round sphere.

8.1.   Half-plane subsystem

Let us start with the simple example where the subsystem A is given by the half-plane $x_1 > 0$ at $\tau = 0$. A path integral calculation of the quantity $I(\rho, \rho')$ in Eq. (2.7) can be obtained as a natural generalization of our previous analysis in two dimensions, and is depicted in the upper pictures of Fig. 22. To proceed, it is useful to introduce a polar coordinate $(T, \zeta, x_2, \ldots, x_d)$ as follows:

$$x_1 = \zeta \cos T, \qquad \tau = \zeta \sin T, \tag{8.1}$$

where $(x_2, \ldots, x_d)$ are the same as before. The metric looks like

$$ds^2 = d\tau^2 + \sum_{i=1}^{d}(dx_i)^2 = dT^2 + T^2 d\eta^2 + \sum_{i=2}^{d}(dx_i)^2. \tag{8.2}$$

By using this polar coordinate, we can express the trace $\text{Tr}[\rho\rho']$ as a path integral on the space illustrated in the lower picture of Fig. 22. Since the two spaces $\mathbf{R}^d$ are glued to each other along A, the periodicity of T is now 4π.

The gravity dual is given by the topological black hole (refer to Ref. [68]):

$$\begin{aligned}
ds^2 &= \frac{dz^2 + d\tau^2 + \sum_{i=1}^{d}(dx_i)^2}{z^2} \\
&= \frac{dr^2}{f(r)} + f(r)dT^2 + r^2\left(\frac{d\eta^2 + \sum_{i=2}^{d}(dx_i)^2}{\zeta^2}\right),
\end{aligned} \tag{8.3}$$

where $f(r) \equiv r^2 - 1 - \frac{\mu}{r^{d-2}}$. The smoothness of the geometry determines the periodicity β_T of T as

$$\beta_T = \frac{4\pi r_+}{(d+1)r_+^2 - (d-1)}, \tag{8.4}$$

where r_+ is the outer horizon $f(r_+) = 0$.

We take the periodicity to be $\beta_T = 2\pi n$. This leads to

$$r_+ = \frac{1}{n(d+1)} + \sqrt{1 - \frac{2}{d+1} + \frac{1}{n^2(d+1)^2}}. \tag{8.5}$$

We can evaluate two-point functions in the holographic CFT from this geometry by applying the standard formula in AdS/CFT:

$$\langle O_1(a)O_2(b)\rangle \sim e^{-\Delta_O L_{ab}}, \tag{8.6}$$

where L_{ab} is the geodesic distance between the two points a and b in the gravity dual. Note that even though the two-point functions on $\mathbf{R}^d$ are universal in higher-dimensional CFTs, that is not true for two-point functions on a curved manifold. Therefore we need the evaluation of two-point functions using the gravity dual.

We consider geodesics described by the form $T = T(r)$, where ζ and $x_2, \ldots, x_d$ take fixed values. The geodesic equation in the metric of Eq. (8.3) looks like

$$\frac{dT}{dr} = \frac{1}{f(r)\left(\frac{f(r)}{f(r_*)} - 1\right)^{1/2}}, \tag{8.7}$$

where r_* is the minimum value of r on the geodesic (or equally the turning point). By integrating the solution to this equation as

$$L_{12} = \int_{r_*}^{r_\infty} \left[f(r)\left(\frac{dT}{dr}\right)^2 + \frac{1}{f(r)} \right]^{1/2}, \tag{8.8}$$

we can find the geodesic length L between two boundary points $(T, r) = (T_a, r_\infty)$ and $(T, r) = (T_b, r_\infty)$; r_∞ is the cutoff at the AdS boundary and is written as $r_\infty = \zeta/\epsilon$ in terms of the CFT cutoff ϵ. The geodesic length L_{ab} is a function of the time difference $T_b - T_a$, and they are parameterized by r_* as

$$T_b - T_a = 2 \int_{r_*}^{r_\infty} \frac{dr}{f(r)\left(\frac{f(r)}{f(r_*)} - 1\right)^{1/2}}, \tag{8.9}$$

$$L_{ab} = 2 \int_{r_*}^{r_\infty} \frac{1}{\sqrt{f(r) - f(r_*)}}. \tag{8.10}$$

Now let us consider the evaluation of $I(\rho, \rho')$. As in the two-dimensional CFT case we apply the large-N factorization, namely generalized free field calculation. Then, the non-trivial Wick contraction is favored when $L_{ab} > L_{bc}$, where the points p_1, p_2, and p_3 are the AdS boundary points $a = (T_1, r_\infty), b = (2\pi - T_1, r_\infty)$, and $c = (T_2, r_\infty)$. Since L_{ab} is a monotonically increasing function of $T_b - T_a$, we find that the non-trivial Wick contraction is favored when $L_{ab} > L_{bc}$ holds, i.e.

$$(2\pi - T_1) - T_1 > T_2 - (2\pi - T_1). \tag{8.11}$$

When we calculate the information metric we assume that p_1 and p_3 are almost the same position in each R^d. This means that $T_2 \simeq 2\pi + T_1$ (look at the bottom picture of Fig. 22). In this way, the condition of non-trivial Wick contraction, Eq. (8.11), leads to

$$0 \leq T_1 < \frac{\pi}{2}. \tag{8.12}$$

In the original coordinates of $(\tau, x_1, \ldots, x_d)$, this is equivalent to

$$x_1 > 0. \tag{8.13}$$

This reproduces the correct entanglement wedge of the half-plane A.

In the Bures distance limit, the replica number n is finally taken to be $n = 1$. Therefore, we do not need to worry about the curved space complications and the two-point function takes the standard universal form:

$$\langle O^\dagger(\tau, x) O(\tau', x') \rangle = \left| (\tau - \tau')^2 + \sum_{i=1}^{d} (x_i - x_i')^2 \right|^{-2\Delta_O}. \tag{8.14}$$

In the same way as the two-dimensional CFT case, we find, in the limit $n = m = 1/2$,

$$A_{1/2, 1/2} = \frac{\langle O^\dagger(-\tau, x) O(\tau', x') \rangle}{\sqrt{\langle O^\dagger(\tau, x) O(-\tau, x) \rangle \cdot \langle O^\dagger(\tau', x') O(-\tau', x') \rangle}}, \tag{8.15}$$

where the two-point functions are given by Eq. (8.14).

Thus, the final Bures information metric is computed as

$$ds^2 = \frac{\Delta_O}{2} \cdot \frac{d\tau^2 + \sum_{i=1}^{d} (dx_i)^2}{\tau^2}. \tag{8.16}$$

This does indeed agree with the time slice metric of a $(d + 2)$-dimensional Poincaré AdS.

8.2. Spherical subsystem

Next, we turn to spherical subsystems. Consider a holographic CFT on R^{d+1}. In polar coordinates, the metric takes

$$ds^2 = d\tau^2 + dr^2 + r^2 d\Omega_{d-1}^2.$$

We take the subregion A to be inside the spherical region defined by $\{\tau = 0, r \leq R\}$. To apply the replica method, we use the map [68]

$$r = R \frac{\sinh(u)}{\cosh(u) + \cos\left(\frac{\tau_H}{R}\right)}, \qquad \tau = R \frac{\sin\left(\frac{\tau_H}{R}\right)}{\cosh(u) + \cos\left(\frac{\tau_H}{R}\right)}.$$

After this coordinate transformation, the metric looks like

$$ds^2 = \frac{1}{\left(\cosh(u) + \cos\left(\frac{\tau_H}{R}\right)\right)^2} \left(d\tau_H^2 + R^2 \left(du^2 + \sinh^2(u) \, d\Omega_{d-1}^2\right)\right),$$

which is conformally equivalent to $S^1 \times H^d$. The S^1 direction represents the Euclidean time coordinate and its period is $\beta = 2\pi R$, and in this map the original surfaces $\tau = 0^-$ and $\tau = 0^+$ will transform to $\tau_H = 0^+$ and $\tau_H = R\beta^-$, respectively.

The gravity dual of the above space is a topological black hole with the metric (see Ref. [68])

$$ds^2 = f(\rho) \, d\tau_{\rm H}^2 + \frac{d\rho^2}{f(\rho)} + \rho^2 \left(du^2 + \sinh^2 u \, d\Omega_{d-1}^2\right), f(\rho) = \frac{\rho^2}{R^2} - 1 - \frac{M}{R^2 \rho^{d-1}}.$$

Around the event horizon we can approximate $f(\rho) \simeq \epsilon f'(\rho^+)$, where ρ^+ is the larger solution of $f(\rho) = 0$. After substituting this form if we require that this spacetime is the regular solution to the Einstein equation, i.e. we do not admit any conical singularity, the inverse temperature is fixed as $\beta_T = \frac{4\pi \rho_+ R^2}{(d+1)\rho_+^2 - (d-1)R^2}$.

Now, let us consider calculating $I(\rho, \rho')$; ρ is a state in which operators $O(\tau, r)$ and $O^\dagger(-\tau, r)$ are inserted, and ρ' is a state in which operators $O(\tau', r')$ and $O^\dagger(-\tau', r')$ are similarly inserted. If we apply the replica method to evaluate the correlation function, we have to consider geodesics in the topological black hole which connect two boundary points, and to choose the mass parameter M in Eq. (8.17) such that the periodicity of $\tau_{\rm H}$ is $4\pi R$. However, as in the previous calculation, the geodesic length is monotonic with the difference of boundary time coordinates, and hence we only have to specify the difference of τ instead of calculating the length of the geodesic directly.

As in the previous argument, we find that non-trivial contraction is favored when

$$0 \leq \tau_{\rm H} \leq \frac{\pi R}{2}. \tag{8.17}$$

This condition is equivalent to

$$0 \leq r \leq \sqrt{R^2 - \tau^2}, \tag{8.18}$$

which indeed perfectly reproduces the expected entanglement wedge in AdS$_{d+2}$.

Correlation functions on $S^1 \times H^d$ are related to those on R^{d+1} by

$$\left\langle \mathcal{O}(\tau_{\rm H}, u) \, \mathcal{O}^\dagger(\tau'_{\rm H}, u') \right\rangle = \left| \frac{\partial(\tau, r)}{\partial(\tau_{\rm H}, u)} \right|^{\Delta_\mathcal{O}} \left| \frac{\partial(\tau', r')}{\partial(\tau_{\rm H}, u')} \right|^{\Delta_\mathcal{O}}$$

$$\times \left(\Omega(\tau_{\rm H}, u) \, \Omega(\tau'_{\rm H}, u')\right)^{\Delta_\mathcal{O}} \left\langle \mathcal{O}(\tau, r) \, \mathcal{O}^\dagger(\tau', r') \right\rangle,$$

where $\Omega = \frac{1}{\cosh(u) + \cos(\frac{\tau_{\rm H}}{R})}$ is a conformal factor.

In the above form we just care about Jacobian and conformal transformations of the correlation functions, whose explicit forms are given by

$$\left\langle \mathcal{O}(\tau, r) \, \mathcal{O}^\dagger(\tau', r') \right\rangle = \left| (\tau - \tau')^2 + (r - r')^2 \right|^{-\Delta_\mathcal{O}},$$

$$\left| \frac{\partial(\tau, r)}{\partial(\tau_{\rm H}, u)} \right| = \left| R \frac{\sinh^2 u - \sin^2 \frac{\tau_{\rm H}}{R}}{\left(\cosh(u) + \cos\left(\frac{\tau_{\rm H}}{R}\right)\right)^2} \right|.$$

Then, the Bures distance becomes

$$A_{\frac{1}{2}, \frac{1}{2}} = \frac{\left\langle \mathcal{O}(-\tau_{\rm H}, u) \, \mathcal{O}^\dagger(\tau'_{\rm H}, u') \right\rangle}{\sqrt{\left\langle \mathcal{O}(-\tau_{\rm H}, u) \, \mathcal{O}^\dagger(\tau_{\rm H}, u) \right\rangle \left\langle \mathcal{O}(-\tau'_{\rm H}, u') \, \mathcal{O}^\dagger(\tau'_{\rm H}, u') \right\rangle}}$$

$$= \frac{\left| (\tau_- - \tau')^2 + (r - r')^2 \right|^{-\Delta_{\mathcal{O}}}}{\left(\left| (\tau_- - \tau)^2 + (r_- - r)^2 \right|^{-\Delta_{\mathcal{O}}} \left| (\tau'_- - \tau')^2 + (r'_- - r')^2 \right|^{-\Delta_{\mathcal{O}}} \right)^{1/2}},$$

where

$$\tau_- = R \frac{\sin\left(\frac{-\tau_H}{R}\right)}{\cosh(u) + \cos\left(\frac{-\tau_H}{R}\right)}, \qquad r_- = R \frac{\sinh(u)}{\cosh(u) + \cos\left(\frac{-\tau_H}{R}\right)}. \tag{8.19}$$

Above, we neglected the spherical part for simplicity; however, we can treat it in a similar way and thus can derive the full Bures metric:

$$ds^2 = \frac{1}{2} \frac{\Delta_{\mathcal{O}}}{\sin^2 \frac{\tau_H}{R}} \left(\frac{1}{R^2} d\tau_H^2 + du^2 + \sinh^2 u \, d\Omega_{d-1}^2 \right). \tag{8.20}$$

By considering a geodesic which connects τ_H at the AdS boundary $\rho = \infty$ and the middle point $\tau_H = 0$ and $\rho = \rho_*$, the relation between τ_H and ρ_* is found as

$$\sin\left(\frac{\tau}{R}\right) = \frac{R}{\rho_*}. \tag{8.21}$$

This maps the Bures metric of Eq. (8.20) into the time slice metric of AdS:

$$ds^2 = \frac{d\rho^2}{\rho^2/R^2 - 1} + \rho^2 (du^2 + \sinh^2 u \, d\Omega_{d-1}^2), \tag{8.22}$$

up to a constant factor.

9. Other distinguishability measures

In this section we analyze behaviors of some more distinguishability measures other than $I(\rho, \rho')$ and $F(\rho, \rho')$ in our CFT setup, and we summarize which distinguishability measures can reproduce correct entanglement wedges, discussing possible reasons.

9.1. Affinity (Hellinger distance)

The affinity $A(\rho, \rho')$ is defined by Eq. (2.5), and the Hellinger distance $D_H(\rho, \rho')$ is introduced as in Eq. (2.16), accordingly. The affinity for our density matrix in Eq. (1.1) in 2d CFTs with a single-interval A can also be evaluated by the analytic continuation of the replica correlation function as

$$A(\rho, \rho') \equiv \lim_{m,n \to \frac{1}{2}} \text{tr} \rho^m \rho'^n = \lim_{m,n \to \frac{1}{2}} \frac{Z_{m,n}}{\mathcal{N}_{m,n}}, \tag{9.1}$$

where the correlation function is the same as in Eq. (4.5) with $k = m + n$, and

$$w_j = \begin{cases} w, & \text{if } j = 1, \dots, m, \\ w', & \text{otherwise.} \end{cases} \tag{9.2}$$

The normalization is given by

$$\mathcal{N}_{m,n} = |w - \bar{w}|^{-4mh} |w' - \bar{w}'|^{-4nh}. \tag{9.3}$$

The partition function can be evaluated in a similar manner to the fidelity. For example, the partition function for the single-interval case is

$$Z_{1/2,1/2} = \begin{cases} |w - \bar{w}|^{-2h} \, |w' - \bar{w}'|^{-2h}, & \text{outside the CFT wedge,} \\ |w - \bar{w}|^{2h} \, |w' - \bar{w}'|^{2h} \, |w - \bar{w}'|^{-8h}, & \text{inside the CFT wedge,} \end{cases} \tag{9.4}$$

where the CFT wedge for the affinity is the same as that for the fidelity. In this example we find that

$$A(\rho, \rho') = F^2(\rho, \rho'). \tag{9.5}$$

Actually, the same relation also holds for the double-interval case. CFT wedges of affinity in both single- and double-interval cases coincide with those of the fidelity, and therefore agree with the actual entanglement wedge in AdS.

9.2. Trace distance

From the property in Eq. (2.19), we have

$$F(\rho, \rho') \to 1 \iff D_{\text{tr}}(\rho, \rho') \to 0. \tag{9.6}$$

Therefore, the trace distance has the same transition point as the fidelity, which perfectly matches the entanglement wedge. It would be interesting to check this conclusion from a direct calculation in holographic CFTs.

9.3. Chernoff bound

The *quantum Chernoff bound* is largely discussed as another distinguishability measure. It was first introduced in Ref. [69] as

$$Q(\rho, \rho') \equiv \min_{0 \leq m \leq 1} Q_m(\rho, \rho'), \tag{9.7}$$

where Q_m is the *quantum Rényi overlaps* [70],

$$Q_m(\rho, \rho') \equiv \operatorname{tr} \rho^m \rho'^{1-m} \lim_{n \to 1-m} = \frac{Z_{m,n}}{\mathcal{N}_{m,n}}. \tag{9.8}$$

The partition function is the same as Eq. (4.5) with $k = m + n$, and

$$w_j = \begin{cases} w, & \text{if } j = 1, \ldots, m, \\ w', & \text{otherwise.} \end{cases} \tag{9.9}$$

Note that this quantity is bounded from above by $Q(\rho, \rho') \leq 1$, which is saturated if $\rho = \rho'$, and from below by $0 \leq Q(\rho, \rho')$, which saturates if $\rho\rho' = 0$. One important property is that the Chernoff bound gives bounds on the affinity and the fidelity as

$$F^2(\rho, \rho') \leq Q(\rho, \rho') \leq A(\rho, \rho') \quad (= Q_{1/2}(\rho, \rho')). \tag{9.10}$$

Combining with Eq. (9.5), one can easily find, for the single- and double-interval cases,

$$A(\rho, \rho') = Q(\rho, \rho') = F^2(\rho, \rho'). \tag{9.11}$$

We can directly check this equality by evaluating the replica partition function. Note that this equality holds if both density states ρ and ρ' are pure states, that is,

$$A(\rho, \rho') = Q(\rho, \rho') = F^2(\rho, \rho') = \text{tr}(\rho\rho').\tag{9.12}$$

Note that we also have the following bounds on the trace distance:

$$1 - Q(\rho, \rho') \le D_{\text{tr}}(\rho, \rho') \le \sqrt{1 - Q^2(\rho, \rho')},\tag{9.13}$$

which is consistent with our conclusion that the quantum Chernoff bound also plays a role as a probe of the correct entanglement wedge.

9.4. Super-fidelity

In general cases, it is hard to get fidelity and affinity due to the complication involved in evaluating the square root of a density matrix. Instead, we can rely on *super-fidelity*, which is defined by

$$F_N(\rho, \rho') \equiv \text{tr}\, \rho\rho' + \sqrt{1 - \text{tr}\, \rho^2}\sqrt{1 - \text{tr}\, \rho'^2}.\tag{9.14}$$

This quantity involves only products of density matrices, which greatly simplifies its evaluation, in sharp contrast with the fidelity. The super-fidelity does not satisfy the property $F_N(\rho, \rho') = 0 \Leftrightarrow \rho\rho' = 0$.

The point is that the super-fidelity gives the upper bound on the fidelity as [71,72]

$$F(\rho, \rho') \le F_N(\rho, \rho') \le 1.\tag{9.15}$$

The equality is satisfied when $\rho = \rho'$. From this inequality, one can find that $F_N(\rho, \rho') < 1$ directly implies $F(\rho, \rho') < 1$, which means that the super-fidelity is another similarity measure.

Let us focus on holographic CFTs. In fact, one can immediately find that $\text{tr}\, \rho\rho' \sim \text{tr}\, \rho^2 \sim \text{tr}\, \rho'^2 \sim e^{-\#c}$, which means that the super-fidelity reduces to the trivial upper bound $F_N(\rho, \rho') = 1$ in the large-c limit. Therefore, we cannot distinguish our two states by making use of the super-fidelity in holographic CFTs. Note that in CFTs with finite c, this also gives a non-trivial bound.

9.5. p-fidelity

A generalization of the fidelity, p-fidelity [36] is defined by

$$F_p(\rho, \rho') \equiv \frac{\left|\left|\sqrt{\rho}\sqrt{\rho'}\right|\right|_p^2}{\max\left\{||\rho||_p^2, ||\rho'||_p^2\right\}},\tag{9.16}$$

where we introduce

$$||A||_p = \left(\text{tr}\left[\left(AA^\dagger\right)^{\frac{p}{2}}\right]\right)^{\frac{1}{p}}.\tag{9.17}$$

The fidelity $F(\rho, \rho')$ coincides with $F_1(\rho, \rho')$. By using the p-fidelity, the lower bound on $F_2(\rho, \rho')$ is given by the measure $I(\rho, \rho')$, Eq. (2.7):

$$F_2(\rho, \rho') \le I(\rho, \rho').\tag{9.18}$$

Therefore, we cannot utilize the 2-fidelity as a probe of the entanglement wedge in general.

Table 1. A ✓ indicates that a measure enables us to reproduce the entanglement wedge.

	Entanglement wedge reproduction
F	✓
A	✓
Q	✓
D_{tr}	✓
JS	✓
F_N	
I	
F_2	

9.6. Quantum Jensen Shannon divergence

The *quantum Jensen Shannon divergence* (QJS divergence) is defined in Ref. [73][4] as

$$JS(\rho, \rho') \equiv H\left(\frac{\rho + \rho'}{2}\right) - \frac{H(\rho) + H(\rho')}{2}, \tag{9.19}$$

where H is the von Neumann entropy. This quantity can also be seen in quantum information theory, where it is called the Holevo information. As shown in Ref. [73], it shares many relevant physical properties with the relative entropy. Since the relative entropy is well defined only in some restricted situations, the QJS divergence is more useful as a distinguishability measure. The QJS divergence also satisfies the inequality (which comes from the bound on the Holevo information [38])

$$0 \leq JS(\rho, \rho') \leq 1, \tag{9.20}$$

where the lower bound is saturated if and only if $\rho = \rho'$.

For two neighboring density states, this quantity can be approximated by the fidelity as

$$JS(\rho, \rho') \simeq 1 - F(\rho, \rho') \quad \text{if } \rho \simeq \rho'. \tag{9.21}$$

Through this relation, we can conclude that the QJS divergence can also probe the entanglement wedge in a similar way to the fidelity.

9.7. Comparison of distinguishability measures and entanglement wedge reconstruction

Finally, we would like to compare the results of the above distinguishability measures in addition to $I(\rho, \rho')$ and the fidelity $F(\rho, \rho')$. CFT wedges defined by the measures $\{F, A, Q, D_{\text{tr}}, JS\}$ reproduce the correct entanglement wedges for 2d holographic CFTs. On the other hand, CFT wedges deviate from the correct entanglement wedges when we employ the measures $\{I, F_N, F_2\}$. This is summarized in Table 1.

The fundamental properties of these measures are listed in Table D.1 in Appendix D. By comparing this table with the previous one, we notice that property (ix), i.e. monotonicity under completely positive trace-preserving (CPTP) maps, seems to be responsible for reproducing correct entanglement wedges.[5] At the same time, another common property for the coincidence between CFT wedges and

---

[4] The QJS divergence has also been studied in the context of holography in Ref. [74].
[5] The monotonicity is analogous to the strong subadditivity of the entanglement entropy [75–77].

entanglement wedges is that the total power of ρ and ρ' is one in the trace, as we emphasized in Sect. 6.6. This requirement comes from probing only the low-energy states dual to the classical gravity. On the the other hand, for the other measures $\{I, F_N, F_2\}$ the total power of ρ and ρ' is two. In this sense the former look analogous to the von Neumann entropy, while the latter seem analogous to the second Rényi entropy. In summary, our results in this paper suggest that these two properties are necessary for a distinguishability measure in holographic CFTs to reconstruct the correct entanglement wedges.[6]

It is interesting to note that there are other similarity measures which satisfy property (ix), for example the relative entropy. For this reason, we can expect that this quantity can also probe the entanglement wedge. It would be interesting to investigate whether the relative entropy can actually detect the entanglement wedge; this is left for future work.

10.　Entanglement wedges from HKLL operators

In this paper we have worked out the shape of the entanglement wedge from purely CFT computations by exciting the CFT vacuum by a local operator inserted at various locations. In this sense, a local operator plays the role of a probe for our holographic geometry. However, we need to choose the conformal dimension of the operator O_α in the range of Eq. (1.2) to obtain sensible results. Even though it will be difficult to remove the constraint $h_\alpha \ll c$ for negligible backreactions, one might think that we can somehow remove the requirement $h_\alpha \gg 1$, which was necessary to have a sharp resolution of the image of the CFT wedge by the local operator. The resolution of the distinguishability can be estimated by the Bures information metric, owing to the Cramér–Rao bound in Eq. (2.21), which is given for the local operator result in Eq. (4.17) as

$$\langle (\delta x)^2 \rangle \geq \frac{\tau^2}{h_\alpha}.\tag{10.1}$$

In this sense, the resolution of our local operator analysis is $O(1/\sqrt{h_\alpha})$ in the length scale. Therefore, we need the assumption $h_\alpha \gg 1$ to probe the geometry. On the other hand, the classical gravity approximation of AdS/CFT predicts that the actual resolution is of scale $O(1/c)$, which is equivalent to the Planck scale. Therefore, the local operator is a slightly coarse-grained probe, especially when h_α is not very large.

A more fined-grained operator for this purpose is known as the HKLL operator [13–15]. This operator is known as the CFT counterpart of a bulk local field operator ϕ_α, and thus should be suitable to extract the bulk geometry including the entanglement wedge. Thus, in this section we would like to study how we can probe the entanglement wedge geometry by the HKLL operator. However, note that analysis of HKLL operators has a disadvantage that the computations become highly complicated compared to the local operator ones. Due to this technical issue, our analysis will rely on heuristic arguments.

---

[6] This observation naturally raises a question: can we find a similar deviation of CFT wedge versus entanglement wedge to I if we employ the Hilbert–Schmidt distance? In particular, is the wedge from I the same as that from the Hilbert–Schmidt distance? $D_{\mathrm{HS}}(\rho, \rho') \equiv \sqrt{\mathrm{tr}(\rho - \rho')^2}$, which is analogous to the second Rényi entropy. It is known that the Hilbert–Schmidt distance is bounded by the trace distance [78] (see also Ref. [79]), $0 \leq D_{\mathrm{HS}}(\rho, \rho') \leq \sqrt{2} D_{\mathrm{tr}}(\rho, \rho')$. Unfortunately, the Hilbert–Schmidt distance reduces to 0 in the large-c limit for the same reason as the super-fidelity, and therefore we cannot extract interesting information from this quantity. Note that $\{F_N, D_{\mathrm{HS}}\}$ have the term $\mathrm{tr}(\rho\rho')$, which means that these two quantities contain the same information as I. In fact, if one appropriately normalizes them, then we can extract the same wedge as from I.

We focus on the simplest setup of AdS_3/CFT_2, where the global AdS_3 is dual to a holographic two-dimensional CFT on a cylinder. The global AdS_3 is described by the coordinates (ρ, x, τ) with the metric in Eq. (4.18), and the two-dimensional cylinder is parameterized by the complex coordinate $\xi = \tau + ix$ and $\bar{\xi} = \tau - ix$. It is useful to employ the state representation of HKLL operators given in Refs. [44,80], which is written as

$$|\phi_\alpha(\rho, x, \tau)\rangle = \tilde{\mathcal{N}}_\alpha \cdot \sum_{k=0}^{\infty} (-1)^k e^{-\delta(L_0^{\xi_0} + \bar{L}_0^{\xi_0})} \frac{\Gamma(2h_\alpha)}{k!\Gamma(k + 2h_\alpha)} (L_{-1}^{\xi_0})^k (\bar{L}_{-1}^{\bar{\xi}_0})^k O_\alpha(\xi_0, \tilde{\xi}_0)|0\rangle, \quad (10.2)$$

where $\tilde{\mathcal{N}}_\alpha$ is the overall normalization for the unit norm; $L_n^{\xi_0}$ and $\bar{L}_n^{\xi_0}$ are the chiral and anti-chiral Virasoro operators around the point ξ_0. The term $e^{-(L_0^{\xi_0} + \bar{L}_0^{\xi_0})\delta}$ represents the regularization of the infinite summation of k over the descendants, and the infinitesimally small parameter δ controls this UV regularization of localized excitation. More importantly, the location ξ_0 on the cylinder is given by the projection along the geodesic which passes through the bulk point (ρ, x, τ) in the global AdS_3 (as depicted in Fig. 1). This is explicitly given by $\xi_0 = \tanh \frac{\rho}{2} \cdot e^{\tau + ix}$.

First, note that the state in Eq. (10.2) can be obtained from our original local operator state by replacing the primary operator with a summation over descendants. In this sense we can effectively estimate the conformal dimension of the local operator in Eq. (10.2) as its average $h_\alpha \sim 1/\delta$. As argued in Ref. [44], in large-c CFTs we expect that δ is $O(1/c)$. This agrees with the resolution expected from the AdS/CFT, i.e. the scale is larger than the Planck scale. Our previous results for the excited states by local operators imply that the result of the Bures information metric for the reduced density matrix ρ_A is identical to that for the pure state as long as the excited point is within the CFT wedge. When we consider a pure HKLL state, i.e. Eq. (10.2), the Bures metric is computed as [44]

$$D_B^2 = \frac{1}{8\delta^2}(d\rho^2 + \sinh^2 \rho dx^2). \quad (10.3)$$

The Cramér–Rao bound from this result indeed agrees with the AdS/CFT prediction $\langle (\delta x)^2 \rangle \geq O(1/\delta^2) = O(1/c^2)$. In other words, the metric in Eq. (10.3) agrees with the correct time slice metric of the global AdS if we set $\delta = O(c)$ up to an $O(1)$ constant.

Moreover, from the above heuristic arguments, we expect that the CFT wedge for the Bures metric for HKLL states agrees with the correct entanglement wedge as in the local operator case. In this way, we can reproduce the shape of the entanglement wedge from analysis of the Bures metric of HKLL states such that the resolution scale agrees with the AdS/CFT expectation. It is an interesting future problem to confirm the above arguments by explicit CFT calculations and their replica interpretations.

11. Conclusions and discussions

We have presented a new method to determine the shape of the entanglement wedge from purely CFT calculations. Our strategy is to introduce CFT wedges, which are counterparts of entanglement wedges in AdS/CFT and which are defined for a given CFT. We can view a CFT wedge as a shadow of an entanglement wedge because the former is obtained from the latter by projecting along a geodesic in AdS backgrounds.

To determine the border of the CFT wedge, we employed the locally excited states and asked whether we can distinguish two reduced density matrices ρ_A and ρ_A' with slightly different points excited. If the points are in the CFT wedge, we can distinguish them, while we cannot if they are outside the wedge. To quantify this we mainly examined two different distinguishability measures,

namely the Bure distance (or equally fidelity) $D_B(\rho, \rho')$ and its Rényi-like version denoted by $I(\rho, \rho')$ (called the geometric mean fidelity). In general, we found that the CFT wedges are sharp only for holographic CFTs, while for generic CFTs the CFT wedges get blurred. This special feature of sharp CFT wedges for holographic CFTs mainly originates from the large-N factorization property. In a very brief summary, we observed that the CFT wedges for the Bures distance perfectly agree with the expected entanglement wedge in AdS/CFT in all the examples we studied. Moreover, it turned out that the Bures metric agrees with the metric on the entanglement wedge in AdS up to the overall factor. Thus, our results provide a genuine CFT derivation of entanglement wedges in AdS/CFT for the first time.

As a first example, we intensively studied the case where the subsystem A is a single interval in 2d CFTs. We found that in holographic CFTs, the border of the CFT wedge becomes sharp and perfectly agrees with the entanglement wedge for both the choices of distinguishability measure. We also studied a free scalar 2d CFT and showed that the CFT wedge structure is obscure, though some qualitative features are similar. This clearly shows that the geometry of entanglement wedges emerges only in holographic CFTs, being consistent with our understanding of AdS/CFT. We also calculated the Bures information metric and found that it is proportional to the metric on the entanglement wedge. Moreover, we studied the time evolution of the reduced density matrix and confirmed that the resulting time-dependent CFT wedges agree with the covariant description of entanglement wedges in AdS/CFT. As a future problem, we can also consider another non-trivial time-dependent setup, the falling-particle geometry, where we can rely on the CFT techniques developed in Refs. [82,83].

As a second, less trivial, example, we chose A to be double intervals in 2d holographic CFTs. In this case, the standard holographic analysis tells us the phase transition between the connected and disconnected entanglement wedge. Our CFT wedge analysis perfectly reproduced this phase transition. However, we found that the resulting CFT wedge for the measure $I(\rho, \rho')$ slightly deviated from the expected entanglement wedge.[7] On the other hand, we showed that the CFT wedge for the Bures distance reproduces the entanglement wedge in AdS/CFT perfectly. We argued that this difference of CFT wedges between two measures occurs because they are sensitive to different parts of the quantum states in CFT. The Bures distance $D_B(\rho, \rho')$ or fidelity $F(\rho, \rho')$ is sensitive to low-energy states as the total power p_{tot} of ρ and ρ' (i.e. $\sim \rho^{p_{tot}}$) is one, while the (second) Rényi-like measure $I(\rho, \rho')$ is also sensitive to high-energy modes as the total power p_{tot} is two. This is analogous to the well-known fact that the von Neumann entropy is simply computed as the area in AdS/CFT, while the computation of Rényi entropy requires us to take into account backreactions [84,85].

We also analyzed an example of 2d boundary conformal field theory (BCFT), which has a gravity dual via AdS/BCFT. This example also experienced a phase transition between a connected and disconnected extremal surface. We showed that the CFT wedges agree with the expectation from entanglement wedges in AdS/BCFT under the assumption that the boundary one-point function vanishes. A similar argument also holds for the thermofield double state without any assumptions. It will also be an interesting future problem to analyze CFT wedges for excited states created by heavy operators, as such states are expected to be dual to pure state black holes. We can imagine that we can calculate the correlation functions of probe operators in the presence of the heavy operators on

---

[7] It might be an interesting possibility to introduce "Rényi-like CFT wedges" defined by the measure $I(\rho, \rho')$, which itself may be useful for further understanding of AdS/CFT. We leave this for a future problem.

the replicated surfaces via a semi-classical approximation of conformal blocks, which is left for a future problem.

Moreover, we presented calculations of CFT wedges in higher-dimensional CFTs when the subsystem A is given by a round ball or a half-space. The resulting CFT wedges perfectly agree with the expectation from the entanglement wedge in the higher-dimensional AdS/CFT. Since this only covers the special example in higher dimensions, it will be an intriguing future problem to further explore higher-dimensional CFT wedges.

Since there are many other known distinguishability measures of quantum states, we examined whether such measures can reproduce the expected CFT wedges. We found that the affinity (Hellinger distance) $A(\rho, \rho')$, the trace distance $D_{\text{tr}}(\rho, \rho')$, the Chernoff bound $Q(\rho, \rho')$, and the quantum Jensen Shannon divergence $JS(\rho, \rho')$ pass this test, as does the Bures distance or fidelity. Interestingly, these measures have the common feature of monotonicity under CPTP maps. Also, they share the aforementioned property that the total power p_{tot} of ρ is one. It will be interesting to understand systematically how the difference in this total power affects the CFT wedges. It will also be an important future problem to extend our analysis of CFT wedges to the qunatum Fisher metric based on the relative entropy, which we have not discussed in this paper.

In the final part of the paper we studied states excited by HKLL operators for the computation of the information metric instead of those created by the local operators in CFTs. This is because, when the conformal dimension is not large, the local operator excitations are not sharp probes for detecting the bulk geometry. The HKLL operators are expected to be localized in a bulk point well even if the conformal dimension is small. We gave a heuristic argument for how we can extract the expected CFT wedge from HKLL states. This allows us to detect the entanglement wedge up to the Planck scale, matching the AdS/CFT prediction. Moreover, the Bures information metric for the HKLL states agrees with the actual metric of AdS up to an $O(1)$ factor, which we could not fix. It will be very interesting to pursue this agreement more with the precise coefficient.

All the calculations in this paper concerned the leading contribution in the $1/N$ or $1/c$ expansion dual to the classical gravity approximation. Therefore, it will be an interesting future direction to study $1/N$ or $1/c$ corrections dual to the quantum corrections in gravity. In this context, we may study the emergence of quantum extremal surfaces [81].

Also, the present work of deriving the entanglement wedges from CFTs might be related to other approaches to entanglement wedges. This involves an emergence of entanglement wedges in path integral optimization [86–89], where the mathematical structure has a significant similarity. Also, one basic geometrical characterization of entanglement wedges will be the entanglement wedge cross section, whose CFT interpretations have been discussed from various viewpoints [90–100]. We hope we come back to these connections in future works.

Appendix A.   Details of calculations of $I(\rho, \rho')$ in the single-interval case

Here we present a detailed analysis of the quantity $I(\rho, \rho')$ when w and w' take generic values. We write $z = p + iq$ ($= z_1$) and $z' = p' + iq'$ ($= -z_3$) such that $p, p' > 0$ and $q, q' < 0$, as we see from Fig. 2. We denote the regions inside and outside the CFT wedge by W_{in} and W_{out}. Note that W_{out} corresponds to $p > -q$ and $p' > -q$. The non-trivial Wick contraction for the calculation of the four-point function $F(z, \bar{z}, -z', -\bar{z}')$ given by Eq. (3.15) is favored when $|z - \bar{z}||z' - \bar{z}'| > |z + \bar{z}'|^2$, i.e.

$$4qq' > (p + p')^2 + (q - q')^2. \tag{A.1}$$

When $w \in W_{\text{out}}$ and $w' \in W_{\text{out}}$, we find that

$$F(z, \bar{z}, -z, -\bar{z}) \simeq |2q|^{-8h}, \qquad F(z', \bar{z}', -z', -\bar{z}') \simeq |2q'|^{-8h}, \tag{A.2}$$

where the trivial Wick contractions are favored. Also, since $(p + p')^2 + (q - q')^2 > (q + q')^2 + (q - q')^2 > 4qq'$, we find that

$$F(z, \bar{z}, -z', -\bar{z}') \simeq |4qq'|^{-4h}, \tag{A.3}$$

where the trivial Wick contractions are favored. Thus, we have $I(\rho, \rho') \simeq 1$.

When $w \in W_{\text{in}}$ and $w' \in W_{\text{out}}$, we find that

$$F(z, \bar{z}, -z, -\bar{z}) \simeq |2p|^{-8h}, \qquad F(z', \bar{z}', -z', -\bar{z}') \simeq |2q'|^{-8h}. \tag{A.4}$$

When the trivial Wick contraction is favored for $F(z, \bar{z}, -z', -\bar{z}')$, we find that

$$I(\rho, \rho') \simeq \frac{|p|^{4h}}{|q|^{4h}} \ll 1 \tag{A.5}$$

in the $h \gg 1$ limit. When the non-trivial one is favored we obtain

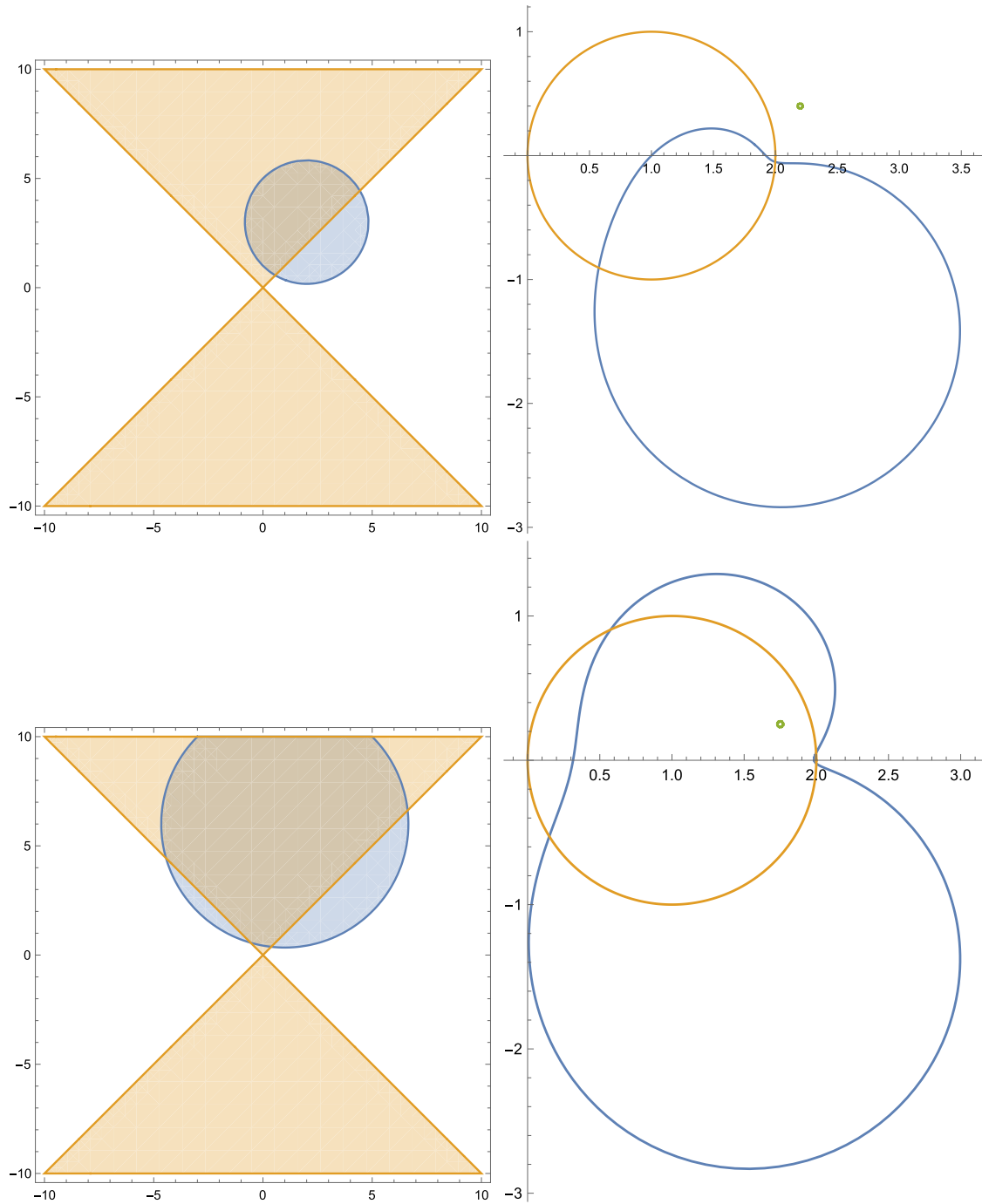$$I(\rho, \rho') \simeq \frac{|4pq'|^{4h}}{|(p + p')^2 + (q - q')^2|^{4h}} \ll 1, \tag{A.6}$$

where we noted that

$$(p + p')^2 + (q - q')^2 > (p - q')^2 + (q - q')^2 > -4pq'. \tag{A.7}$$

Thus, in this case we have $I(\rho, \rho') \simeq 0$.

Finally, when $w \in W_{\text{in}}$ and $w' \in W_{\text{in}}$, we have

$$F(z, \bar{z}, -z, -\bar{z}) \simeq |2p|^{-8h}, \qquad F(z', \bar{z}', -z', -\bar{z}') \simeq |2p'|^{-8h}. \tag{A.8}$$

Fig.A.1. The profile of the regions of z' and w' (surrounded by blue curves) where the non-trivial Wick contraction is favored, i.e. $|z - \bar{z}||z' - \bar{z}'| > |z + \bar{z}'|^2$. In the upper pictures we set $z = 2 - i$ (outside the wedge), and in the lower two pictures we set $z = 1 - 2i$ (inside the wedge). The left and right pictures depict the regions in the z'- and w'-plane, respectively. The orange curves describe the borders of the wedges. The green points describe the locations of w and z. We took the subsystem A to be $[0, 2]$.

When the trivial Wick contraction is favored for $F(z, \bar{z}, -z', -\bar{z}')$, we find that

$$I(\rho, \rho') \simeq \frac{|pp'|^{4h}}{|qq'|^{4h}} \ll 1 \tag{A.9}$$

in the $h \gg 1$ limit, unless $p = p'$ and $q = q'$. When the non-trivial one is favored we obtain

$$I(\rho, \rho') \simeq \frac{|4pp'|^{4h}}{|(p+p')^2 + (q-q')^2|^{4h}} \ll 1, \tag{A.10}$$

where we noted that

$$(p+p')^2 + (q-q')^2 \geq 4pp', \tag{A.11}$$

with the equality holding when $p = p'$ and $q = q'$. Thus, in this case we have $I(\rho, \rho') \simeq 0$ except for the case $w = w'$. If $w = w'$ we have $I(\rho, \rho') = 1$. See Fig. A.1 for plots.

When $\delta z = z' - z$ is infinitesimally small, we can expand $D_I(\rho, \rho') \equiv 2 - 2I(\rho, \rho')$ as follows:

$$D_I(\rho, \rho') \simeq \frac{4h}{|z + \bar{z}|^2} \cdot |dz|^2$$

$$= \frac{h}{4} \cdot \frac{\left(\sqrt{x(L-x) + i\tau L + \tau^2} + \sqrt{x(L-x) - i\tau L + \tau^2}\right)^2}{\tau^2 \sqrt{x^2 + \tau^2}\sqrt{(L-x)^2 + \tau^2}} (dx^2 + d\tau^2). \tag{A.12}$$

This is the expression of the information metric constructed from the distance measure D_I.

Appendix B. Detailed analysis of the Bures metric in $c = 1$ CFT

We start with the expression in Eq. (4.9) and consider the free scalar CFT

$$A_{n,m} = k^{-4kh} \cdot |z|^{8mnh(1-k)} \cdot |z'|^{4nh(1-k)} \cdot |z^k - \bar{z}^k|^{8mnh} \cdot |z'^k - \bar{z}'^k|^{4nh}$$

$$\times \langle O_\alpha^\dagger(z_1)O_\alpha(z_2) \cdots O_\alpha^\dagger(z_{2k-1})O(z_{2k})\rangle \cdot \frac{Z^{(k)}}{(Z^{(1)})^k}. \tag{B.1}$$

Below we set $h = 1/2$ by assuming the operator $O = e^{i\phi}$.

We can write the $2k$-point function as

$$\langle O_\alpha^\dagger(z_1)O_\alpha(z_2) \cdots O_\alpha^\dagger(z_{2k-1})O(z_{2k})\rangle = f(z)^k \cdot g(z,z')^n, \tag{B.2}$$

such that $f(z)^k$ corresponds to the computation $\mathrm{Tr}\,\rho^k$ and $g(z,z')^n$ corresponds to the ratio between $\mathrm{Tr}(\rho^m \rho' \rho^m)^n$ and $\mathrm{Tr}\,\rho^k$. The former, $f(z)$, is computed as

$$f(z) = \frac{\prod_{j=1}^{k-1} |z - ze^{\frac{2\pi i}{k}j}|^{4h}}{\prod_{j=0}^{k-1} |z - \bar{z}e^{\frac{2\pi i}{k}j}|^{4h}} = \frac{k^2}{2r^2(1 - \cos(k\theta_1))}, \tag{B.3}$$

where we set $h = 1/2$. We define

$$r = \sqrt{x^2 + y^2}, \qquad r' = \sqrt{x'^2 + y'^2},$$

$$\cos\theta_1 = \frac{x^2 - y^2}{r^2}, \qquad \sin\theta_1 = \frac{2xy}{r^2},$$

$$\cos\theta_2 = \frac{xx' - yy'}{rr'}, \qquad \sin\theta_2 = \frac{x'y + xy'}{rr'},$$

$$\cos\theta_3 = \frac{xx' + yy'}{rr'}, \qquad \sin\theta_3 = \frac{x'y - xy'}{rr'},$$

$$\cos\theta_4 = \frac{x'^2 - y'^2}{r'^2}, \qquad \sin\theta_4 = \frac{2x'y'}{r'^2}. \tag{B.4}$$

The function $g(z, z')$ is estimated as

$$
\begin{aligned}
&g(z, z') \\
&= \left[\frac{\prod_{j=0}^{k-1}|z - \bar{z}e^{\frac{2\pi i}{k}j}|^{4h} \cdot \prod_{j=1}^{k-1}|z' - ze^{\frac{2\pi i}{k}j}|^{4h}}{\prod_{j=1}^{k-1}|z - \bar{z}'e^{\frac{2\pi i}{k}j}|^{4h} \cdot \prod_{j=1}^{k-1}|z - ze^{\frac{2\pi i}{k}j}|^{4h}}\right]^2 \cdot \\
&\quad \left[\frac{\prod_{l=1}^{n-1}|z - \bar{z}'e^{\frac{2\pi i}{n}l}|^{4h} \cdot \prod_{l=1}^{n-1}|z - ze^{\frac{2\pi i}{n}l}|^{4h}}{\prod_{l=0}^{n-1}|z - \bar{z}e^{\frac{2\pi i}{n}l}|^{4h} \cdot \prod_{l=1}^{n-1}|z' - ze^{\frac{2\pi i}{n}l}|^{4h}}\right] \cdot \\
&\quad \left[\frac{\prod_{l=1}^{n-1}|z - \bar{z}'e^{\frac{2\pi i}{n}l}|^{4h} \cdot \prod_{l=1}^{n-1}|z' - z'e^{\frac{2\pi i}{n}l}|^{4h}}{\prod_{l=0}^{n-1}|z' - \bar{z}'e^{\frac{2\pi i}{n}l}|^{4h} \cdot \prod_{l=1}^{n-1}|z - z'e^{\frac{2\pi i}{n}l}|^{4h}}\right] \\
&= \prod_{j=0}^{k-1}\left[\frac{|z - \bar{z}e^{\frac{2\pi i}{k}j}|^{4h} \cdot |z' - ze^{\frac{2\pi i}{k}j}|^{4h}}{|z - \bar{z}'e^{\frac{2\pi i}{k}j}|^{4h}}\right]^2 \cdot \prod_{l=0}^{n-1}\left[\frac{|z - \bar{z}'e^{\frac{2\pi i}{n}l}|^{4h}}{|z - \bar{z}e^{\frac{2\pi i}{n}l}|^{4h}|z' - ze^{\frac{2\pi i}{n}l}|^{4h}}\right] \\
&\quad \cdot \prod_{l=0}^{n-1}\left[\frac{|z - \bar{z}'e^{\frac{2\pi i}{n}l}|^{4h}}{|z' - \bar{z}'e^{\frac{2\pi i}{n}l}|^{4h}|z - z'e^{\frac{2\pi i}{n}l}|^{4h}}\right] \cdot \frac{\prod_{l=1}^{n-1}\left[|z - ze^{\frac{2\pi i}{n}l}|^{4h} \cdot |z' - z'e^{\frac{2\pi i}{n}l}|^{4h}\right]}{\prod_{j=1}^{k-1}|z - ze^{\frac{2\pi i}{k}j}|^{8h}}. \tag{B.5}
\end{aligned}
$$

Let us assume that $h_\alpha = 1/2$. To evaluate $g(z, z')$, the following identities are useful:

$$\prod_{j=1}^{n-1}\sin\left(\frac{\pi}{n}j\right) = \frac{n}{2^{n-1}}, \tag{B.6}$$

and, for $w = re^{i\theta}$ and $w' = r'e^{i\theta'}$,

$$\prod_{j=0}^{n-1}|w - w'e^{\frac{2\pi i}{n}j}|^2 = r^{2n} + r'^{2n} - 2r^n r'^n \cos\left(n(\theta - \theta')\right). \tag{B.7}$$

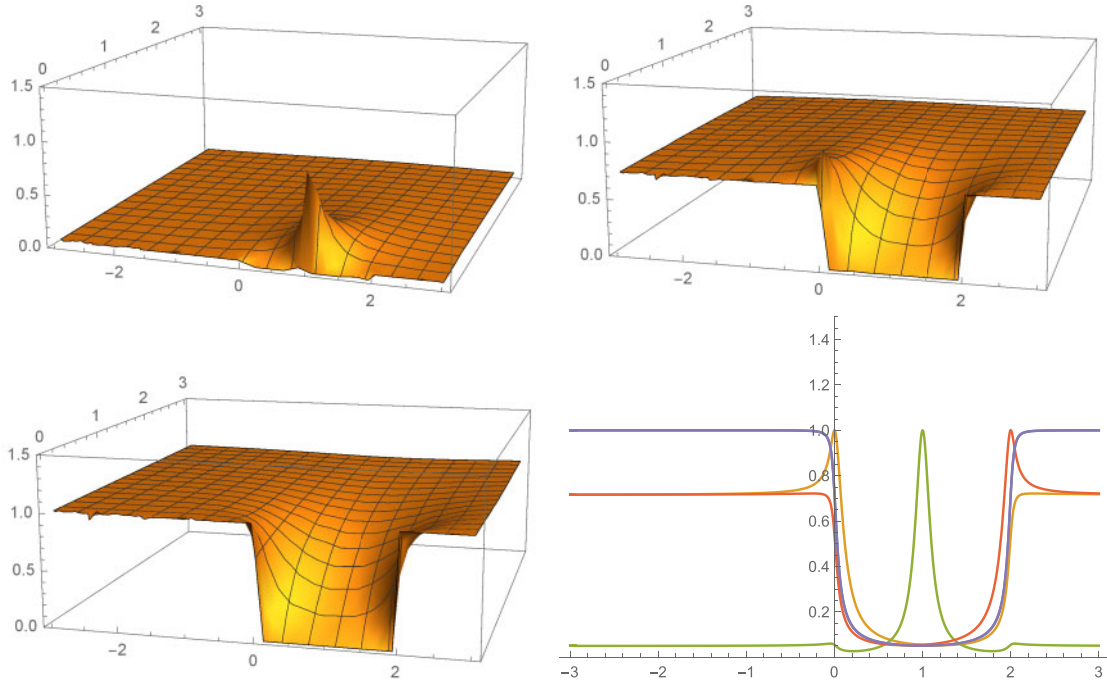If we write $w = x + iy$ and $w' = x' + iy'$, we have

$$\cos(\theta - \theta') = \frac{xx' + yy'}{rr'}, \qquad \sin(\theta - \theta') = \frac{x'y - xy'}{rr'}. \tag{B.8}$$

By using Eqs. (B.6) and (B.8) we can rewrite $g(z, z')$ as

$$
\begin{aligned}
g(z, z') &= \left[\frac{2r^{2k}(1 - \cos(k\theta_1))\left(r^{2k} + r'^{2k} - 2r^k r'^k \cos(k\theta_3)\right)}{\left(r^{2k} + r'^{2k} - 2r^k r'^k \cos(k\theta_2)\right)(2r)^{2(k-1)} \cdot k^2 \cdot 2^{2(1-k)}}\right]^2 \\
&\quad \times \frac{\left(r^{2n} + r'^{2n} - 2r^n r'^n \cos(n\theta_2)\right)^2 \cdot (2r)^{2(n-1)}(2r')^{2(n-1)} \cdot n^4 \cdot 2^{4(1-n)}}{\left(r^{2n} + r'^{2n} - 2r^n r'^n \cos(n\theta_3)\right)^2 \cdot 2(r)^{2n}(1 - \cos(n\theta_1)) \cdot 2(r')^{2n}(1 - \cos(n\theta_4))}. \tag{B.9}
\end{aligned}
$$

Finally, by taking the limit $n = m \to 1/2$ ($k \to 1$), we find that

$$A_{n=1/2,m=1/2} = |z - \bar{z}| \cdot |z' - \bar{z}'| \cdot \frac{1}{4y^2} \cdot g(z, z')^{1/2}, \tag{B.10}$$

Fig. B.1. The profile of $A_{n=1/2, m=1/2} = \text{Tr}\left[\sqrt{\sqrt{\rho}\rho'\sqrt{\rho}}\right]$ in $c = 1$ free scalar CFT for the operator $O = e^{i\phi}$ which has the dimension $h = 1/2$ for various choices of excited points. The upper left, upper right, and lower left graphs describe $A_{n=1/2, m=1/2}$ for $\rho(w = 1 + 0.05i)$, $\rho(w = 0.05i)$, and $\rho(w = -1 + 0.05i)$, respectively, as a function of (p, q) for $\rho'(w' = p + iq)$. The lower right graphs describe $A_{n=1/2, m=1/2}$ for $w = s + 0.05i$ [$s = -1$ (blue), $s = 0$ (orange), $s = 1$ (green), and $s = 2$ (red)] as a function of p such that $w' = p + 0.05i$, with $L = 2$.

where $g(z, z')$ in the limit $n = m \to 1/2$ reads

$$g(z, z')_{n=m=1/2} = \left[\frac{4y^2 \cdot \left(r^2 + r'^2 - 2rr'\cos\theta_3\right)}{r^2 + r'^2 - 2rr'\cos\theta_2} \cdot \frac{r + r' - 2\sqrt{rr'}\cos(\theta_2/2)}{r + r' - 2\sqrt{rr'}\cos(\theta_3/2)}\right]^2$$

$$\times \frac{(1/16) \cdot (1/rr')}{4rr'(1 - \cos(\theta_1/2)(1 - \cos(\theta_4/2)))}. \quad \text{(B.11)}$$

Thus, we obtain

$$A_{n=1/2, m=1/2} = \frac{r + r' + 2\sqrt{rr'}\cos(\theta_3/2)}{r + r' + 2\sqrt{rr'}\cos(\theta_2/2)} \cdot \frac{|y||y'|}{2rr'\sqrt{(1 - \cos(\theta_1/2))(1 - \cos(\theta_4/2))}}. \quad \text{(B.12)}$$

To evaluate Eq. (B.12) we have to be careful with the computations of cosines such as $\cos(\theta_3/2)$. For this, it is useful to focus on the case $m = 1/2$ and $k = 2n$ for the integer n in Eqs. (B.3) and (B.9), which corresponds to the calculation of $\text{Tr}[(\rho\rho')^n]$. In this case we have

$$\cos(n\theta_1) = \frac{1}{2}\left(\zeta + \zeta^{-1}\right), \qquad \cos(2n\theta_1) = \frac{1}{2}\left(\zeta^2 + \zeta^{-2}\right),$$

$$\cos(n\theta_2) = \frac{1}{2}\left(\zeta^{1/2}\zeta'^{1/2} + \zeta^{-1/2}\zeta'^{-1/2}\right), \qquad \cos(2n\theta_2) = \frac{1}{2}\left(\zeta\zeta' + \zeta^{-1}\zeta'^{-1}\right),$$

$$\cos(n\theta_3) = \frac{1}{2}\left(\zeta^{1/2}\zeta'^{-1/2} + \zeta^{-1/2}\zeta'^{1/2}\right), \qquad \cos(2n\theta_3) = \frac{1}{2}\left(\zeta\zeta'^{-1} + \zeta^{-1}\zeta'\right),$$

$$\cos(n\theta_4) = \frac{1}{2}\left(\zeta' + \zeta'^{-1}\right), \qquad \cos(2n\theta_4) = \frac{1}{2}\left(\zeta'^2 + \zeta'^{-2}\right), \quad \text{(B.13)}$$

where we defined

$$\zeta = \frac{z^{2n}}{|z|^{2n}} = \frac{w}{w-L} \cdot \frac{|w-L|}{|w|}, \qquad \zeta' = \frac{z'^{2n}}{|z'|^{2n}} = \frac{w'}{w'-L} \cdot \frac{|w'-L|}{|w'|}. \qquad (B.14)$$

By using this expression we can take the analytical continuation $n \to 1/2$. In this way we obtain the final expression in Eq. (4.37).

We have plotted $A_{n=1/2,m=1/2} = \text{Tr}\left[\sqrt{\sqrt{\rho}\rho'\sqrt{\rho}}\right]$ for fixed choices of w' as a function of $w' = p+iq$ in Fig. B.1 and Fig. 6. We find a localized peak $A \simeq 1$ at $w = w'$ when w is close to the center of the subsystem A. However, the entanglement wedge is not clear again, as opposed to the holographic case.

Appendix C.   General time-dependent case

For a generic pure state in a holographic CFT with a gravity dual, the fidelity $F(\rho, \rho') = A_{1/2,1/2}$ is computed from the two-point function $\langle O_\alpha^\dagger(w, \bar{w}) O_\alpha(w', \bar{w}') \rangle$ in such a state dual to a geodesic length $L(w, \bar{w} : w', \bar{w}')$, simply written as $L(w : w')$, as

$$A_{1/2,1/2} \simeq \exp\left\{ h\left[L(w_1 : w_2) + L(w_1' : w_2') - L(w_1' : w_2) - L(w_1 : w_2') \right] \right\}. \qquad (C.1)$$

By setting $w_1 = x_1 + i\tau_1$ and $w_2 = x_2 - i\tau_2$ and taking the limits $x_{1,2}' - x_{1,2} = dx^{1,2} \to 0$ and $\tau_{1,2}' - \tau_{1,2} = d\tau^{1,2} \to 0$, this leads to the Bures metric given by

$$\begin{aligned} D_{\text{B}}^2 &= 2(1 - A_{1/2,1/2}) \\ &\simeq (-2h) \cdot \left[(\partial_{x_1}\partial_{x_2}L)dx_1 dx_2 + (\partial_{x_1}\partial_{\tau_2}L)dx_1 d\tau_2 \right. \\ &\qquad \left. + (\partial_{\tau_1}\partial_{x_2}L)d\tau_1 dx_2 + (\partial_{\tau_1}\partial_{\tau_2}L)d\tau_1 d\tau_2 \right]. \end{aligned} \qquad (C.2)$$

If we set $x_1 = x_2 = x$ and $\tau_1 = \tau_2 = \tau$, we get the 2d metric

$$D_{\text{B}}^2 \simeq (-2h) \cdot \left[(\partial_{x_1}\partial_{x_2}L)(dx)^2 + (\partial_{x_1}\partial_{\tau_2}L + \partial_{\tau_1}\partial_{x_2}L)d\tau dx + (\partial_{\tau_1}\partial_{\tau_2}L)d\tau d\tau \right]. \qquad (C.3)$$

If we plug in the geodesic length in Poincaré AdS$_3$, $L = \log[(x_1 - x_2)^2 + (\tau_1 + \tau_2)^2]$, we obtain

$$\begin{aligned} D_{\text{B}}^2 &= h\left[G_{xx}dx_1 dx_2 + G_{tx}(dx_1 d\tau_2 - dx_2 d\tau_2) + G_{tt}d\tau_1 d\tau_2 \right], \\ G_{xx} &= G_{tt} = \frac{4\left[(\tau_1 + \tau_2)^2 - (x_1 - x_2)^2\right]}{\left[(\tau_1 + \tau_2)^2 + (x_1 - x_2)^2\right]^2}, \\ G_{tx} &= \frac{8\left[(\tau_1 + \tau_2)(x_1 - x_2)\right]}{\left[(\tau_1 + \tau_2)^2 + (x_1 - x_2)^2\right]^2}. \end{aligned} \qquad (C.4)$$

If we restrict to $x_1 = x_2 = x$, then we reproduce the metric in Eq. (5.12) as expected.

Appendix D.   Distinguishability measures

Here we list the fundamental properties (including Joza's axioms [102]) of distinguishability measures, and summarize them in Table D.1 (see Ref. [36] for more details).

(i) $0 \leq \mathcal{F}(\rho, \rho') \leq 1$
(ii) $\mathcal{F}(\rho, \rho') = 1$ if and only if $\rho = \rho'$
(iii) $\mathcal{F}(\rho, \rho') = 0$ if and only if $\rho\rho' = 0$

Table D.1. A $\checkmark$ indicates when a measure satisfies the particular property (i)–(ix). "S" means that the quantity satisfies super-multiplicativity but not multiplicativity.

	(i)	(ii)	(iii)	(iv)	(v)	(vi)	(vii)	(viii)	(ix)
F	$\checkmark$	$\checkmark$	$\checkmark$	$\checkmark$	$\checkmark$	$\checkmark$	$\checkmark$	$\checkmark$	$\checkmark$
A	$\checkmark$	$\checkmark$	$\checkmark$	$\checkmark$	$\checkmark$	$\checkmark$	$\checkmark$	$\checkmark$	$\checkmark$
Q	$\checkmark$	$\checkmark$	$\checkmark$	$\checkmark$	$\checkmark$	$\checkmark$	$\checkmark$	$\checkmark$	$\checkmark$
D_{tr}*	$\checkmark$	$\checkmark$	$\checkmark$	$\checkmark$	$\checkmark$	?		$\checkmark$	$\checkmark$
JS*,†	$\checkmark$	$\checkmark$	$\checkmark$	$\checkmark$	$\checkmark$	$\checkmark$			$\checkmark$
F_N	$\checkmark$	$\checkmark$		$\checkmark$	$\checkmark$	$\checkmark$	$\checkmark$	S	
I	$\checkmark$	$\checkmark$	$\checkmark$	$\checkmark$	$\checkmark$			$\checkmark$	
F_2	$\checkmark$	$\checkmark$	$\checkmark$	$\checkmark$	$\checkmark$			$\checkmark$	

* The properties (ii) and (iii) for D_{tr} and JS are defined based on $1 - D_{\text{tr}}$ and $1 - JS$, instead of themselves. †: The QJS divergence satisfies convexity, instead of concavity [(vi) and (vii)].

(iv) $\mathcal{F}(\rho, \rho') = \mathcal{F}(\rho', \rho)$

(v) $\mathcal{F}(U \rho U^\dagger, U \rho' U^\dagger) = \mathcal{F}(\rho, \rho')$ for any unitary operator U

(vi) $\mathcal{F}\left(\sum_i p_i \rho_i, \rho'\right) \geq \sum_i p_i \mathcal{F}\left(\rho_i, \rho'\right)$ for any $p_i \geq 0$ such that $\sum_i p_i = 1$ (*separable concavity*)

(vii) $\mathcal{F}\left(\sum_i p_i \rho_i, \sum_j p_j \rho'_j\right) \geq \sum_i p_i \mathcal{F}\left(\rho_i, \rho'_i\right)$ for any $p_i \geq 0$ s.t. $\sum_i p_i = 1$ (*joint concavity*)

(viii) $\mathcal{F}\left(\rho_1 \otimes \rho_2, \rho'_1 \otimes \rho'_2\right) = \mathcal{F}(\rho_1, \rho'_1)\mathcal{F}(\rho_2, \rho'_2)$ (*multiplicativity*)

(viii) (S) $\mathcal{F}\left(\rho_1 \otimes \rho_2, \rho'_1 \otimes \rho'_2\right) \geq \mathcal{F}(\rho_1, \rho'_1)\mathcal{F}(\rho_2, \rho'_2)$ (*super-multiplicativity*)

(ix) $\mathcal{F}\left(\mathcal{E}(\rho), \mathcal{E}(\rho')\right) \geq \mathcal{F}(\rho, \rho')$ for any CPTP map $\mathcal{E}$.

References

[1] J. Maldacena, Adv. Theor. Math. Phys. **2**, 231 (1998) [arXiv:hep-th/9711200] [Search INSPIRE].
[2] S. S. Gubser, I. R. Klebanov, and A. M. Polyakov, Phys. Lett. B **428**, 105 (1998) [arXiv:hep-th/9802109] [Search INSPIRE].
[3] E. Witten, Adv. Theor. Math. Phys. **2**, 253 (1998) [arXiv:hep-th/9802150] [Search INSPIRE].
[4] B. Czech, J. L. Karczmarek, F. Nogueira, and M. Van Raamsdonk, Class. Quantum Grav. **29**, 155009 (2012) [arXiv:1204.1330 [hep-th]] [Search INSPIRE].
[5] A. C. Wall, Class. Quantum Grav. **31**, 225007 (2014) [arXiv:1211.3494 [hep-th]] [Search INSPIRE].
[6] M. Headrick, V. E. Hubeny, A. Lawrence, and M. Rangamani, J. High Energy Phys. **1412**, 162 (2014) [arXiv:1408.6300 [hep-th]] [Search INSPIRE].
[7] S. Ryu and T. Takayanagi, Phys. Rev. Lett. **96**, 181602 (2006).
[8] S. Ryu and T. Takayanagi, J. High Energy Phys. **0608**, 045 (2006).
[9] V. E. Hubeny, M. Rangamani, and T. Takayanagi, J. High Energy Phys. **0707**, 062 (2007) [arXiv:0705.0016 [hep-th]] [Search INSPIRE].
[10] T. Nishioka, S. Ryu, and T. Takayanagi, J. Phys. A: Math. Theor. **42**, 504008 (2009).
[11] T. Takayanagi, Class. Quantum Grav. **29**, 153001 (2012) [arXiv:1204.2450 [gr-qc]] [Search INSPIRE];
[12] T. Nishioka, Rev. Mod. Phys. **90**, 035007 (2018) [arXiv:1801.10352 [hep-th]] [Search INSPIRE].
[13] A. Hamilton, D. Kabat, G. Lifschytz, and D. A. Lowe, Phys. Rev. D **73**, 086003 (2006) [arXiv:hep-th/0506118] [Search INSPIRE].
[14] A. Hamilton, D. Kabat, G. Lifschytz, and D. A. Lowe, Phys. Rev. D **74**, 066009 (2006) [arXiv:hep-th/0606141] [Search INSPIRE].
[15] A. Hamilton, D. Kabat, G. Lifschytz, and D. A. Lowe, Phys. Rev. D **75**, 106001 (2007); **75**, 129902 (2007) [erratum] [arXiv:hep-th/0612053] [Search INSPIRE].
[16] T. Faulkner and A. Lewkowycz, J. High Energy Phys. **1707**, 151 (2017) [arXiv:1704.05464 [hep-th]] [Search INSPIRE].
[17] T. Faulkner, A. Lewkowycz, and J. Maldacena, J. High Energy Phys. **1311**, 074 (2013) [arXiv:1307.2892 [hep-th]] [Search INSPIRE].

[18] D. L. Jafferis, A. Lewkowycz, J. Maldacena, and S. J. Suh, J. High Energy Phys. **1606**, 004 (2016) [arXiv:1512.06431 [hep-th]] [Search INSPIRE].

[19] A. Almheiri, X. Dong, and D. Harlow, J. High Energy Phys. **1504**, 163 (2015) [arXiv:1411.7041 [hep-th]] [Search INSPIRE].

[20] D. Harlow, Commun. Math. Phys. **354**, 865 (2017) [arXiv:1607.03901 [hep-th]] [Search INSPIRE].

[21] X. Dong, D. Harlow, and A. C. Wall, Phys. Rev. Lett. **117**, 021601 (2016) [arXiv:1601.05416 [hep-th]] [Search INSPIRE].

[22] Y. Suzuki, T. Takayanagi, and K. Umemoto, Phys. Rev. Lett. **123**, 221601 (2019) [arXiv:1908.09939 [hep-th]] [Search INSPIRE].

[23] T. Takayanagi, Phys. Rev. Lett. **107**, 101602 (2011) [arXiv:1105.5165 [hep-th]] [Search INSPIRE].

[24] M. Fujita, T. Takayanagi, and E. Tonni, J. High Energy Phys. **1111**, 043 (2011) [arXiv:1108.5152 [hep-th]] [Search INSPIRE].

[25] M. Nozaki, T. Takayanagi, and T. Ugajin, J. High Energy Phys. **1206**, 066 (2012) [arXiv:1205.1573 [hep-th]] [Search INSPIRE].

[26] M. Headrick, Phys. Rev. D **82**, 126010 (2010) [arXiv:1006.0047 [hep-th]] [Search INSPIRE].

[27] T. Hartman, arXiv:1303.6955 [hep-th] [Search INSPIRE].

[28] T. Hartman, C. A. Keller, and B. Stoica, J. High Energy Phys. **1409**, 118 (2014) [arXiv:1405.5137 [hep-th]] [Search INSPIRE].

[29] M. Nozaki, T. Numasawa, and T. Takayanagi, Phys. Rev. Lett. **112**, 111602 (2014) [arXiv:1401.0539 [hep-th]] [Search INSPIRE].

[30] M. Nozaki, J. High Energy Phys. **1410**, 147 (2014) [arXiv:1405.5875 [hep-th]] [Search INSPIRE].

[31] F. C. Alcaraz, M. I. Berganza, and G. Sierra, Phys. Rev. Lett. **106**, 201601 (2011) [arXiv:1101.2881 [cond-mat.stat-mech]] [Search INSPIRE].

[32] M. Hayashi, *Quantum Information Theory* (Springer, New York, 2016).

[33] S. Luo and Q. Zhang, Phys. Rev. A **69**, 032106 (2004).

[34] X. Wang, C.-S. Yu, and X. X. Yi, Phys. Lett. A **373**, 58 (2008) [arXiv:0807.1781 [quant-ph]].

[35] J. Liu, X. Lu, J. Ma and X. Wang, Sci. China Phys. Mech. Astron. **55**, 1529 (2012).

[36] Y.-C. Liang, Y.-H. Yeh, P. E. M. F. Mendonça, R. Y. Teh, M. D. Reid, and P. D. Drummond, Rep. Prog. Phys. **82**, 076001 (2019) [arXiv:1810.08034 [quant-ph]] [Search INSPIRE].

[37] J. Cardy, Phys. Rev. Lett. **112**, 220401 (2014) [arXiv:1403.3040 [cond-mat.stat-mech]] [Search INSPIRE].

[38] M. A. Nielsen and I. Chuang, *Quantum Computation and Quantum Information* (Cambridge University Press, Cambridge, 2002).

[39] J. Zhang, P. Ruggiero, and P. Calabrese, J. High Energy Phys. **1910**, 181 (2019) [arXiv:1907.04332 [hep-th]] [Search INSPIRE].

[40] J. Zhang, P. Ruggiero, and P. Calabrese, Phys. Rev. Lett. **122**, 141602 (2019) [arXiv:1901.10993 [hep-th]] [Search INSPIRE].

[41] J. Zhang and P. Calabrese, J. High Energy Phys. **2002**, 056 (2020) [arXiv:1911.04797 [hep-th]] [Search INSPIRE].

[42] A. Bhattacharyya, T. Takayanagi, and K. Umemoto, J. High Energy Phys. **1911**, 107 (2019) [arXiv:1909.04680 [hep-th]] [Search INSPIRE].

[43] C. W. Helstrom, Phys. Lett. A **25**, 101 (1967).

[44] M. Miyaji, T. Numasawa, N. Shiba, T. Takayanagi, and K. Watanabe, Phys. Rev. Lett. **115**, 171602 (2015) [arXiv:1506.01353 [hep-th]] [Search INSPIRE].

[45] V. E. Hubeny and M. Rangamani, J. High Energy Phys. **1206**, 114 (2012) [arXiv:1204.1698 [hep-th]] [Search INSPIRE].

[46] S. He, T. Numasawa, T. Takayanagi, and K. Watanabe, Phys. Rev. D **90**, 041701(R) (2014) [arXiv:1403.0702 [hep-th]] [Search INSPIRE].

[47] S. El-Showk and K. Papadodimas, J. High Energy Phys. **1210**, 106 (2012) [arXiv:1101.4163 [hep-th]] [Search INSPIRE].

[48] N. Lashkari, Phys. Rev. Lett. **113**, 051602 (2014) [arXiv:1404.3216 [hep-th]] [Search INSPIRE].

[49] N. Lashkari, Phys. Rev. Lett. **117**, 041601 (2016) [arXiv:1508.03506 [hep-th]] [Search INSPIRE].

[50] G. Sárosi and T. Ugajin, J. High Energy Phys. **1607**, 114 (2016) [arXiv:1603.03057 [hep-th]] [Search INSPIRE].

[51] G. Sárosi and T. Ugajin, J. High Energy Phys. **1702**, 060 (2017) [arXiv:1611.02959 [hep-th]] [Search INSPIRE].

[52] G. Sárosi and T. Ugajin, J. High Energy Phys. **1801**, 012 (2018) [arXiv:1705.01486 [hep-th]] [Search INSPIRE].

[53] M. A. Rajabpour, Phys. Rev. B **92**, 075108 (2015) [arXiv:1501.07831 [cond-mat.stat-mech]] [Search INSPIRE].

[54] M. A. Rajabpour, arXiv:1503.07771 [hep-th] [Search INSPIRE].

[55] M. A. Rajabpour, J. Stat. Mech. **1606**, 063109 (2016) [arXiv:1512.03940 [hep-th]] [Search INSPIRE].

[56] S. W. Hawking and D. N. Page, Commun. Math. Phys. **87**, 577 (1983).

[57] P. Calabrese and J. Cardy, J. Stat. Mech. **0504**, P04010 (2005) [arXiv:cond-mat/0503393 [cond-mat.stat-mech]] [Search INSPIRE].

[58] J. L. Cardy, Nucl. Phys. B **324**, 581 (1989).

[59] T. Hartman and J. Maldacena, J. High Energy Phys. **1305**, 014 (2013) [arXiv:1303.1080 [hep-th]] [Search INSPIRE].

[60] A. L. Fitzpatrick, J. Kaplan, and M. T. Walters, J. High Energy Phys. **1408**, 145 (2014) [arXiv:1403.6829 [hep-th]] [Search INSPIRE].

[61] G. Penington, J. High Energ. Phys. **2009**, 2 (2020) [arXiv:1905.08255 [hep-th]] [Search INSPIRE].

[62] A. Almheiri, R. Mahajan, J. Maldacena, and Y. Zhao, J. High Energ. Phys. **2003**, 149 (2020) [arXiv:1908.10996 [hep-th]] [Search INSPIRE].

[63] M. Rozali, J. Sully, M. Van Raamsdonk, C. Waddell, and D. Wakeham, J. High Energ. Phys. **2005**, 4 (2020) [arXiv:1910.12836 [hep-th]] [Search INSPIRE].

[64] H. Z. Chen, Z. Fisher, J. Hernandez, R. C. Myers, and S.-M. Ruan, J. High Energ. Phys. **2003**, 152 (2020) [arXiv:1911.03402 [hep-th]] [Search INSPIRE].

[65] G. Penington, S. H. Shenker, D. Stanford, and Z. Yang, arXiv:1911.11977 [hep-th] [Search INSPIRE].

[66] A. Almheiri, T. Hartman, J. Maldacena, E. Shaghoulian, and A. Tajdini, J. High Energ. Phys. **2003**, 13 (2020) [arXiv:1911.12333 [hep-th]] [Search INSPIRE].

[67] J. Maldacena, J. High Energy Phys. **0304**, 021 (2003) [arXiv:hep-th/0106112] [Search INSPIRE].

[68] H. Casini, M. Huerta, and R. C. Myers, J. High Energy Phys. **1105**, 036 (2011) [arXiv:1102.0440 [hep-th]] [Search INSPIRE].

[69] K. M. R. Audenaert, J. Calsamiglia, R. Muñoz-Tapia, E. Bagan, Ll. Masanes, A. Acin, and F. Verstraete, Phys. Rev. Lett. **98**, 160501 (2007) [arXiv:quant-ph/0610027].

[70] M. Boca, I. Ghiu, P. Marian and T. A. Marian, Phys. Rev. A **79**, 014302 (2009) [arXiv:0806.1892 [quant-ph]].

[71] J. A. Miszczak, Z. Puchała, P. Horodecki, A. Uhlmann, and K. Życzkowski, arXiv:0805.2037 [quant-ph].

[72] P. E. M. F. Mendonça, R. d. J. Napolitano, M. A. Marchiolli, C. J. Foster, and Y.-C. Liang, Phys. Rev. A **78**, 052330 (2008) [arXiv:0806.1150 [quant-ph]].

[73] A. P. Majtey, P. W. Lamberti, and D. P. Prato, Phys. Rev. A **72**, 052310 (2005).

[74] S. He, F.-L. Lin, and J.-j. Zhang, J. High Energy Phys. **1712**, 073 (2017) [arXiv:1708.05090 [hep-th]] [Search INSPIRE].

[75] E. Lieb and M. B. Ruskai, Phys. Rev. Lett. **30**, 434 (1973).

[76] E. H. Lieb and M. B. Ruskai, J. Math. Phys. **14**, 1938 (1973).

[77] M. Headrick and T. Takayanagi, Phys. Rev. D **76**, 106013 (2007) [arXiv:0704.3719 [hep-th]] [Search INSPIRE].

[78] P. J. Coles, Phys. Rev. A **85**, 042103 (2012).

[79] P. J. Coles, M. Cerezo, and L. Cincio, Phys. Rev. A **100**, 022103 (2019) [arXiv:1903.11738 [quant-ph]].

[80] K. Goto and T. Takayanagi, J. High Energy Phys. **1710**, 153 (2017) [arXiv:1704.00053 [hep-th]] [Search INSPIRE].

[81] N. Engelhardt and A. C. Wall, J. High Energy Phys. **1501**, 073 (2015) [arXiv:1408.3203 [hep-th]] [Search INSPIRE].

[82] Y. Kusuki and M. Miyaji, J. High Energ. Phys. **1908**, 63 (2019) [arXiv:1905.02191 [hep-th]] [Search INSPIRE].

[83] Y. Kusuki, J. High Energ. Phys. **1807**, 10 (2018) [arXiv:1804.06171 [hep-th]] [Search INSPIRE].

[84] L.-Y. Hung, R. C. Myers, M. Smolkin, and A. Yale, J. High Energy Phys. **1112**, 047 (2011) [arXiv:1110.1084 [hep-th]] [Search INSPIRE].

[85] X. Dong, Nature Commun. **7**, 12472 (2016) [arXiv:1601.06788 [hep-th]] [Search INSPIRE].

[86] M. Miyaji, T. Takayanagi, and K. Watanabe, Phys. Rev. D **95**, 066004 (2017) [arXiv:1609.04645 [hep-th]] [Search INSPIRE].

[87] P. Caputa, N. Kundu, M. Miyaji, T. Takayanagi, and K. Watanabe, Phys. Rev. Lett. **119**, 071602 (2017) [arXiv:1703.00456 [hep-th]] [Search INSPIRE].

[88] P. Caputa, N. Kundu, M. Miyaji, T. Takayanagi, and K. Watanabe, J. High Energy Phys. **1711**, 097 (2017) [arXiv:1706.07056 [hep-th]] [Search INSPIRE].

[89] A. Bhattacharyya, P. Caputa, S. R. Das, N. Kundu, M. Miyaji, and T. Takayanagi, J. High Energy Phys. **1807**, 086 (2018) [arXiv:1804.01999 [hep-th]] [Search INSPIRE].

[90] K. Umemoto and T. Takayanagi, Nature Phys. **14**, 573 (2018) [arXiv:1708.09393 [hep-th]] [Search INSPIRE].

[91] P. Nguyen, T. Devakul, M. G. Halbasch, M. P. Zaletel, and B. Swingle, J. High Energy Phys. **1801**, 098 (2018) [arXiv:1709.07424 [hep-th]] [Search INSPIRE].

[92] K. Umemoto and Y. Zhou, J. High Energy Phys. **1810**, 152 (2018) [arXiv:1805.02625 [hep-th]] [Search INSPIRE].

[93] J. Kudler-Flam and S. Ryu, Phys. Rev. D **99**, 106014 (2019) [arXiv:1808.00446 [hep-th]] [Search INSPIRE].

[94] Y. Kusuki, J. Kudler-Flam, and S. Ryu, Phys. Rev. Lett. **123**, 131603 (2019) [arXiv:1907.07824 [hep-th]] [Search INSPIRE].

[95] P. Caputa, M. Miyaji, T. Takayanagi, and K. Umemoto, Phys. Rev. Lett. **122**, 111601 (2019) [arXiv:1812.05268 [hep-th]] [Search INSPIRE].

[96] K. Tamaoka, Phys. Rev. Lett. **122**, 141601 (2019) [arXiv:1809.09109 [hep-th]] [Search INSPIRE].

[97] S. Dutta and T. Faulkner, arXiv:1905.00577 [hep-th] [Search INSPIRE].

[98] Y. Kusuki and K. Tamaoka, arXiv:1907.06646 [hep-th] [Search INSPIRE].

[99] Y. Kusuki and K. Tamaoka, J. High Energ. Phys. **2002**, 17 (2020) [arXiv:1909.06790 [hep-th]] [Search INSPIRE].

[100] K. Umemoto, Phys. Rev. D **100**, 126021 (2019) [arXiv:1907.12555 [hep-th]] [Search INSPIRE].

[101] T. Eguchi, P. B. Gilkey, and A. J. Hanson, Phys. Rept. **66**, 213 (1980).

[102] R. Jozsa, J. Mod. Opt. **41**, 2315 (1994).